Tuning Catalytic and Electronic Properties of Supported Ni Catalysts by Altering Zeolite Beta Elemental Composition

By

MICHAEL MELONI
DISSERTATION

Submitted in partial satisfaction of the requirements for the degree of

DOCTOR OF PHILOSOPHY

in

Chemical Engineering

in the

OFFICE OF GRADUATE STUDIES

of the

UNIVERSITY OF CALIFORNIA

DAVIS

Approved:

Ron C. Runnebaum, Chair

Coleman X. Kronawitter

Bruce C. Gates

Committee in Charge

2021

Table of Contents

Michael Meloni

December 2021

Chemical Engineering

Tuning Catalytic and Electronic Properties of Supported Ni Catalysts by Altering Zeolite Beta Elemental Composition

Abstract

Zeolites are commonly used as a support for transition metal catalysts due to their high surface area, ability to stabilize isolated cations, and porous structure. The basic building block of a zeolite is the TO_4 tetrahedra where T is usually Si^{4+} but can be substituted with other elements such as Al^{3+}, Fe^{3+}, and B^{3+}. The charge disparity that results from these substitutions creates the need for an extraframework cation that can be a transition metal. The compositional flexibility of certain zeolite frameworks, such as BEA and MFI, make them a good candidate to use a modular support whose elemental composition can be modified without changing the crystallographic structure of the support. The research in this dissertation was focused on using the flexibility in elemental composition of the BEA zeolite framework to tune the properties of a supported metal. The electron density, as well as reactivity, of a supported metal catalyst can be influenced by changes in zeolite elemental composition. This approach resulted in an increased understanding of how zeolite composition influences highly dispersed, supported metals.

Zeolite Beta (BEA framework) supported Ni catalysts were synthesized and tested for catalytic activity using ethylene dimerization. The naming convention that will be used is M-[X]-Beta, where M is the extra-framework cation and X is the heteroatom composition. The catalysts were characterized using Fourier Transform Infrared Spectroscopy (FTIR) with various probe molecules, N_2 adsorption, x-ray diffraction (XRD), catalysis, and thermogravimetric analysis (TGA). Ni was dispersed onto H-[X]-Beta (X

= Al, Ga, and Fe) via anhydrous deposition by using n-pentane solvent and $Ni(acac)_2$ as the metal source. N_2 adsorption, as well as XRD, demonstrated that there is no significant change to the crystallinity or pore structure of the zeolite after Ni deposition. CO and NO adsorption onto the cationic Ni sites showed the presence of Ni in extraframework exchange positions and the relative electron density of the Ni cation increases in the order Ni-[Fe]-Beta > Ni-[Ga]-Beta > Ni-[Al]-Beta. C_2H_4 adsorption shows that the Ni cations on Ni-[Ga]-Beta and Ni-[Al]-Beta have alkyl ligands bonded to them of various length, while after exposure to C_2H_4 the adsorbed species on Ni-[Fe]-Beta are butenes. As C_2H_4 dimerization catalysts, operating at 180 °C and 2.16 kPa C_2H_4, the activity towards the formation of butene is in the order: Ni-[Fe]-Beta > Ni-[Ga]-Beta > Ni-[Al]-Beta. The activation energy was measured to be 44.8 kJ/mol and 32.4 kJ/mol for Ni-[Al]-Beta and Ni-[Fe]-Beta respectively, indicating that Ni-[Fe]-Beta is more effectively stabilizing the TOF determining transition state.

Ni was atomically dispersed into the vacant silanol nests of dealuminated Beta zeolite and used as a C_2H_4 hydrogenation catalyst. NH_4-[Al]-Beta was dealuminated with HNO_3 to create silanol nests, then Ni was deposited using $Ni(acac)_2$ in n-pentane. After evacuation of the solvent the sample was calcined in air to remove the acac ligands. The Ni sites were probed by solid-state FTIR with CO and NO adsorption, which confirmed the presence of cationic Ni^{2+} in silanol nests. X-ray Absorption Spectroscopy (XAS) of the oxidized Ni-[DeAl]-Beta was used to determine the geometry and average local environment of the Ni sites. Wavelet analysis of Ni-[DeAl]-Beta and NiO was used to show the absence of Ni – Ni scattering in the oxidized Ni-[DeAl]-Beta extended x-ray absorption fine spectrum (EXAFS). The pre-edge feature of the XANES region suggested that Ni is in a tetrahedral geometry. EXAFS fitting found a Ni – O coordination number of 4 and Ni – Si coordination number of 4, consistent with Ni dispersed into silanol nests. Ni-[DeAl]-Beta catalysts were activated by reduction in 10% H_2 at 300°C, then used for C_2H_4 hydrogenation. XANES after reduction shows approximately 50% of Ni sites are reduced to a metallic state. EXAFS analysis shows Ni metallic clusters of approximate 1 nm in size based on Ni – Ni coordination numbers. STEM images also indicate that there is a lack of large Ni clusters (> 1 nm) after reduction of Ni-

[DeAl]-Beta. Ni-[DeAl]-Beta was found to be 20-fold more active than Ni-[Al]-Beta and 2.9-fold more active than NiO-SiO_2 as a C_2H_4 hydrogenation catalyst. The work in this dissertation furthers knowledge in the field of heterogenous catalysis forward by demonstrating how zeolites can be used as a modular support for transition metals. The compositional flexibility in zeolite Beta is leveraged to influence the active metal site without changing the crystallographic structure of the support. The fine control over the electronic properties and geometry of active Ni sites represents progress towards more creating more tunable sites for a heterogenous catalyst.

Acknowledgments

I would like to thank the Alex Yeh and Noah Felvey who were with me from the beginning and helped to establish the Runnebaum lab. They worked with me to setup most instruments in the lab, a process that was totally foreign to me. They also helped me grow as a researcher and person throughout my PhD. As friends and colleagues, I could not have asked for better people to work with.

I thank my advisor Ron Runnebaum for giving me the freedom to work towards goals that I found interesting.

I would like to thank my collaborators Jiyun Hong, Adam Hoffman, and Simon Bare for running experiments, fitting EXAFS data, and helping troubleshoot issues that we came across.

I would like to thank the burrito crew of the Gates and Runnebaum lab members for always being supportive and getting burritos of sadness, happiness, or any other emotion.

I thank my family for being supportive throughout my PhD.

I would like to thank all my lifting and coffee drinking partners for making each morning fun.

I thank all the friends I have made at Davis who made the experience truly memorable.

List of Publications

1. Meloni, M. & Runnebaum, R. C. Tuning supported Ni catalysts by varying zeolite Beta heteroatom composition: effects on ethylene adsorption and dimerization catalysis. *Catal. Sci. Technol.* **11**, 3393–3401 (2021).
2. Albrahim, M. *et al.* Reduction and Agglomeration of Supported Metal Clusters Induced by High-Flux X-ray Absorption Spectroscopy Measurements. *J. Phys. Chem. C* **125**, 11048–11057 (2021).
3. Felvey, N. W., Meloni, M. J., Kronawitter, C. X. & Runnebaum, R. C. Ethane dehydrogenation over Cr/ZSM-5: Characterization of active sites through probe molecule adsorption FTIR. *Catal. Sci. Technol.* **10**, 5069–5081 (2020).

Chapter 1: Introduction

1.1 Introduction

Supported metal catalysts are commonly used for a wide variety of chemical reactions such as hydrogenation, oligomerization, and selective catalytic reduction.[1–3] A current challenge in the field of metal supported catalysts is understanding how the support influences the electronic properties and reactivity of the supported metal. The metal support interactions can drastically affect the activity and selectivity of a metal catalyst.[4] Zeolites are high surface area, porous and crystalline silicates that are used themselves as a catalyst and for cation ion-exchange. The charge disparity introduced into the zeolite framework of substituting T^{3+} ($T = Al^{3+}$, Ga^{3+}, Fe^{3+} or B^{3+}), referred to as heteroatom substitution, instead of Si^{4+} requires extraframework cation sites to balance the negative charge of the zeolite framework.[5] The composition of the heteroatom influences properties of the zeolite such as the acidity when H^+ is the extraframework cation.[6–8] Transition metals such as Cu, Ni, and Pt can also be dispersed onto these extraframework cation sites.[9] Altering the elemental composition of the heteroatom site while keeping the same zeolite framework, enables studying of how support-metal interactions can be tuned while keeping the same 3-D structure of the support. Zeolite Beta is unique among zeolites because it is a large pore zeolite and can be synthesized with a variety of heteroatoms.[10–12] Not only is it able of incorporating T^{3+} heteroatoms, but other elements such as Ni, Ti, and Sn can be inserted into the zeolite framework.[13–15] The compositional flexibility of zeolite Beta enables its use as a tunable support to influence the properties of a supported metal cation, while keeping the crystallographic structure of the support the same.

Ni is commonly used in catalysis as an active metal site because it effectively catalyzes a variety of reactions and costs orders of magnitude less than other platinum group elements. One reaction of interest is the building of longer chain hydrocarbons from smaller ones by alkene di-/oligo-merization.[16–18] This approach is a shift compared to traditional methods of creating medium chain hydrocarbons which involves the processing of petroleum.[19] Instead, sustainably sourced smaller hydrocarbons, such as C_2H_4 produced from ethanol, can be used as the feedstock replacing petroleum.[17,20,21] Typical catalysts studied for C_2H_4 di-/oligo-merization are cationic Ni dispersed onto aluminosilicates such as [Al]-Beta and [Al]-MCM-41.[22–24] C_2H_4 dimerization with Ni-Beta catalysts presented an opportunity to study how Ni catalysts can be tuned

to increase activity and selectivity through changes in zeolite elemental composition. The local coordination environment of the supported Ni cations should remain similar between the different elemental compositions of Beta, but the electron donating/withdrawing properties of the support will be altered via heteroatom compositional changes.

In Chapter 2, the effect of zeolite Beta framework composition on the properties of a supported Ni cation is examined. The hypothesis was that the electron donating/withdrawing properties of the support could be altered by changing the elemental composition of the Beta zeolite. The relative electron density of the Ni cations is probed with Fourier transform infrared spectroscopy (FTIR) using CO and NO adsorption to the Ni sites. The interaction of the Ni sites with C_2H_4, reactant for dimerization, was examined by C_2H_4 adsorption at room temperature with FTIR. The results from FTIR probe molecules demonstrated that the Beta support composition influences the electron density of the Ni cation, as well as the interaction with C_2H_4. The electron density of the Ni cations increased in the order Ni-[Fe]-Beta > Ni-[Ga]-Beta > Ni-[Al]-Beta (where [X] is the framework heteroatom and Ni is an extraframework cation). The Ni-[X]-Beta catalysts were used for C_2H_4 dimerization to determine if activity and selectivity can be increased by altering the support composition. It was found that Ni-[Fe]-Beta was 2.4-fold more active than Ni-[Al]-Beta and more selective towards the formation of butenes.

In Chapter 3, the research builds upon Chapter 2 by examining in more detail the differences in Ni sites between Ni-[Fe]-Beta and Ni-[Al]-Beta. The activation energy for C_2H_4 dimerization was determined for both catalysts between 160 – 200°C, with values of 32.5 kJ/mol for Ni-[Fe]-Beta and 48.8 kJ/mol for Ni-[Al]-Beta respectively. The difference in activation energy indicates that Ni-[Fe]-Beta is more effective at stabilizing the TOF determining transition state. The reducibility of the Ni cations was compared using temperature programmed reduction (TPR) with CO by using solid-state FTIR spectroscopy. The Ni cations present in Ni-[Al]-Beta were more reducible by CO, as indicated by the appearance of Ni^+ carbonyl bands at lower (ca. 80°C) temperature than Ni-[Fe]-Beta (ca. 220°C). The influence of H_2 on the activity of Ni-[Fe]-Beta was studied by varying the partial pressure of H_2 from 0 – 32 kPa during catalysis. The increase

in H_2 partial pressure increases the rate of butene formation at the expense of selectivity. At 32 kPa H_2 there is a sharp decrease in butene selectivity from 0.75 to 0.59 over 1 h. The effect of preparation method was studied by synthesizing a sample by using anhydrous deposition (with $Ni(acac)_2$) and by dispersing Ni via ion exchange with $Ni(NO_3)_2$. The reaction rate (normalized by amount of dispersed Ni) of Ni-[Fe]-Beta prepared by ion-exchange was 1.4-fold higher than the catalyst prepared via anhydrous deposition, but the activation energy measured was the same.

The work in Chapter 4 demonstrates how the removal of framework heteroatoms can create isolated Ni sites that enable the synthesis of nanometer-sized metallic Ni clusters. Framework Al was removed from NH_4-[Al]-Beta through an acid treatment to form silanol nests in place of framework Al. Ni deposition, followed by calcination, resulted in Ni reoccupying the silanol nests (material is referred to as Ni-[DeAl]-Beta). The Ni sites were characterized with CO and NO adsorption with FTIR spectroscopy as well as with x-ray absorption spectroscopy (XAS) and scanning transmission electron microscopy (STEM). CO and NO adsorption were used to show the presence of Ni initially in a silanol nests. The pre-edge peak in the X-ray absorption near edge spectrum (XANES) showed that Ni was in an approximately tetrahedral geometry. The fit of the extended X-ray absorption fine structure (EXAFS) was consistent with Ni reoccupying silanol nests. Ni-[DeAl]-Beta was tested as a C_2H_4 hydrogenation catalyst then compared to other catalysts Ni-[Al]-Beta and NiO-SiO_2. Prior to catalysis, the materials were treated in 10% H_2 at 300°C. The reduced Ni-[DeAl]-Beta catalyst was characterized using CO adsorption as well as XAS and STEM. The resulting fit from the extended x-ray absorption fine structure (EXAFS) is used to estimate the size of metallic Ni nanoparticles to be approximately 0.9 – 1.2 nm. The STEM images of the reduced catalyst show a lack of large (> 1 nm) nanoparticles, which is consistent with metallic particles of 1 nm or less. The activity of Ni-[DeAl]-Beta for hydrogenation was 16-fold higher than Ni-[Al]-Beta and 2-fold higher than NiO-SiO_2. The effect of reduction temperature was studied to better understand the catalytically active Ni sites. Catalytic activity was tested after reduction of Ni-[DeAl]-Beta at 200°C, 250°C, and 300°C; the apparent reaction rate of was 6% lower after reduction at 250°C compared to 300°C. Reduction with H_2 at different

temperatures was also monitored with FTIR spectroscopy by reducing in H_2, then adsorbing CO at room temperature. The results show that less Ni^0 is formed after reduction at 250°C compared to 300°C. This difference suggests that either highly active Ni^0 is formed at 250°C or cationic Ni in silanol nests is also active for C_2H_4 hydrogenation.

1.2 References

(1) Zhang, L.; Zhou, M.; Wang, A.; Zhang, T. Selective Hydrogenation over Supported Metal Catalysts: From Nanoparticles to Single Atoms. *Chem. Rev.* **2020**, *120* (2), 683–733. https://doi.org/10.1021/acs.chemrev.9b00230.

(2) Finiels, A.; Fajula, F.; Hulea, V. Nickel-Based Solid Catalysts for Ethylene Oligomerization – a Review. *Catal. Sci. Technol.* **2014**, *4* (8), 2412–2426. https://doi.org/10.1039/C4CY00305E.

(3) Guan, B.; Zhan, R.; Lin, H.; Huang, Z. Review of State of the Art Technologies of Selective Catalytic Reduction of NOx from Diesel Engine Exhaust. *Appl. Therm. Eng.* **2014**, *66* (1–2), 395–414. https://doi.org/10.1016/j.applthermaleng.2014.02.021.

(4) Lu, J.; Aydin, C.; Browning, N. D.; Gates, B. C. Oxide- and Zeolite-Supported Isostructural Ir(C 2H 4) 2 Complexes: Molecular-Level Observations of Electronic Effects of Supports as Ligands. *Langmuir* **2012**, *28* (35), 12806–12815. https://doi.org/10.1021/la302522a.

(5) Aiello, R.; Nagy, J. B.; Giordano, G.; Katovic, A.; Testa, F. Isomorphous Substitution in Zeolites. *Comptes Rendus Chim.* **2005**, *8* (3–4), 321–329. https://doi.org/10.1016/j.crci.2005.01.014.

(6) Jones, A. J.; Carr, R. T.; Zones, S. I.; Iglesia, E. Acid Strength and Solvation in Catalysis by MFI Zeolites and Effects of the Identity, Concentration and Location of Framework Heteroatoms. *J. Catal.* **2014**, *312*, 58–68. https://doi.org/10.1016/j.jcat.2014.01.007.

(7) Eichler, U.; Brändle, M.; Sauer, J. Predicting Absolute and Site Specific Acidities for Zeolite

Catalysts by a Combined Quantum Mechanics/Interatomic Potential Function Approach †. *J. Phys. Chem. B* **1997**, *101* (48), 10035–10050. https://doi.org/10.1021/jp971779a.

(8) Jones, A. J.; Iglesia, E. The Strength of Brønsted Acid Sites in Microporous Aluminosilicates. *ACS Catal.* **2015**, *5* (10), 5741–5755. https://doi.org/10.1021/acscatal.5b01133.

(9) Dědeček, J.; Čapek, L.; Kaucký, D.; Sobalík, Z.; Wichterlová, B. Siting and Distribution of the Co Ions in Beta Zeolite: A UV-Vis-NIR and FTIR Study. *J. Catal.* **2002**, *211* (1), 198–207. https://doi.org/10.1016/S0021-9517(02)93697-3.

(10) Patet, R. E.; Koehle, M.; Lobo, R. F.; Caratzoulas, S.; Vlachos, D. G. General Acid-Type Catalysis in the Dehydrative Aromatization of Furans to Aromatics in H-[Al]-BEA, H-[Fe]-BEA, H-[Ga]-BEA, and H-[B]-BEA Zeolites. *J. Phys. Chem. C* **2017**, *121* (25), 13666–13679. https://doi.org/10.1021/acs.jpcc.7b02344.

(11) Tang, B.; Dai, W.; Sun, X.; Wu, G.; Guan, N.; Hunger, M.; Li, L. Mesoporous Zr-Beta Zeolites Prepared by a Post-Synthetic Strategy as a Robust Lewis Acid Catalyst for the Ring-Opening Aminolysis of Epoxides. *Green Chem.* **2015**, *17* (3), 1744–1755. https://doi.org/10.1039/c4gc02116a.

(12) Bare, S. R.; Kelly, S. D.; Sinkler, W.; Low, J. J.; Modica, F. S.; Valencia, S.; Corma, A.; Nemeth, L. T. Uniform Catalytic Site in Sn-β-Zeolite Determined Using X-Ray Absorption Fine Structure. *J. Am. Chem. Soc.* **2005**, *127* (37), 12924–12932. https://doi.org/10.1021/ja052543k.

(13) Roy, S.; Bakhmutsky, K.; Mahmoud, E.; Lobo, R. F.; Gorte, R. J. Probing Lewis Acid Sites in Sn-Beta Zeolite. *ACS Catal.* **2013**, *3* (4), 573–580. https://doi.org/10.1021/cs300599z.

(14) Dědeček, J.; Sobalík, Z.; Wichterlová, B. Siting and Distribution of Framework Aluminium Atoms in Silicon-Rich Zeolites and Impact on Catalysis. *Catal. Rev. - Sci. Eng.* **2012**, *54* (2), 135–223. https://doi.org/10.1080/01614940.2012.632662.

(15) Penkova, A.; Dzwigaj, S.; Kefirov, W. R.; Hadjiivanov, K.; Che, M. Effect of the Preparation Method on the State of Nickel Ions in BEA Zeolites. A Study by Fourier Transform Infrared Spectroscopy of Adsorbed CO and NO, Temperature-Programmed Reduction, and X-Ray Diffraction. *J. Phys. Chem. C* **2007**, *111* (24), 8623–8631. https://doi.org/10.1021/jp071927p.

(16) Aresta, M.; Dibenedetto, A.; Angelini, A. Catalysis for the Valorization of Exhaust Carbon: From CO2 to Chemicals, Materials, and Fuels. Technological Use of CO2. *Chemical Reviews*. 2014, pp 1709–1742. https://doi.org/10.1021/cr4002758.

(17) Wang, S.; Agirrezabal-Telleria, I.; Bhan, A.; Simonetti, D.; Takanabe, K.; Iglesia, E. Catalytic Routes to Fuels from C1 and Oxygenate Molecules. *Faraday Discuss.* **2017**, *197*, 9–39. https://doi.org/10.1039/c7fd00018a.

(18) Mülhaupt, R. Green Polymer Chemistry and Bio-Based Plastics: Dreams and Reality. *Macromol. Chem. Phys.* **2013**, *214* (2), 159–174. https://doi.org/10.1002/macp.201200439.

(19) Chen, G. Q.; Patel, M. K. Plastics Derived from Biological Sources: Present and Future: A Technical and Environmental Review. *Chem. Rev.* **2012**, *112* (4), 2082–2099. https://doi.org/10.1021/cr200162d.

(20) Morschbacker, A. Bio-Ethanol Based Ethylene. *Polym. Rev.* **2009**, *49* (2), 79–84. https://doi.org/10.1080/15583720902834791.

(21) Resasco, D. E.; Wang, B.; Crossley, S. Zeolite-Catalysed C-C Bond Forming Reactions for Biomass Conversion to Fuels and Chemicals. *Catal. Sci. Technol.* **2016**, *6* (8), 2543–2559. https://doi.org/10.1039/c5cy02271a.

(22) Moussa, S.; Concepción, P.; Arribas, M. A.; Martínez, A. Nature of Active Nickel Sites and Initiation Mechanism for Ethylene Oligomerization on Heterogeneous Ni-Beta Catalysts. *ACS Catal.* **2018**, *8* (5), 3903–3912. https://doi.org/10.1021/acscatal.7b03970.

(23) Agirrezabal-Telleria, I.; Iglesia, E. Stabilization of Active, Selective, and Regenerable Ni-Based Dimerization Catalysts by Condensation of Ethene within Ordered Mesopores. *J. Catal.* **2017**, *352*, 505–514. https://doi.org/10.1016/j.jcat.2017.06.025.

(24) Joshi, R.; Zhang, G.; Miller, J. T.; Gounder, R. Evidence for the Coordination-Insertion Mechanism of Ethene Dimerization at Nickel Cations Exchanged onto Beta Molecular Sieves. *ACS Catal.* **2018**, 11407–11422. https://doi.org/10.1021/acscatal.8b03202.

Chapter 2

Tuning supported Ni catalysts by varying zeolite Beta heteroatom composition: effects on ethylene adsorption and dimerization catalysis

Adapted from publication in Catalysis Science and Technology

M. Meloni and R. C. Runnebaum, *Catal. Sci. Technol.*, 2021, **11**, 3393–3401.
DOI:10.1039/d1cy00308a

2.1 Abstract

The influence of zeolite heteroatom composition on the electron density and catalytic activity of a supported Ni cation is examined. Ni-[X]-Beta catalysts, where X = Al, Ga, Fe, or dealuminated, were synthesized and characterized with probe molecule adsorption with FTIR spectroscopy and C_2H_4 dimerization catalysis. It was observed via CO adsorption that supported Ni cations were increasing in electron density in the order: [Fe]>[Ga]>[Al]. C_2H_4 dimerization activity increased with increasing electron density of the Ni cation. Despite similarities in reported acid site strength, the acid sites on [Fe]-Beta in this work had significantly lower activity than [Ga]-Beta for the skeletal isomerization of linear butenes as well as C_2H_4 dimerization. Introducing H_2 as a reactant resulted in a decrease in dimerization activity for Ni-[Al]-Beta and Ni-[Ga]-Beta but an increase for Ni-[Fe]-Beta. The selectivity and activity of Ni-[DeAl]-Beta changed dramatically with the introduction of H_2, which subsequently converted all C_2H_4 with ca. 100% selectivity towards C_2H_6 (even with a lower space velocity relative to without H_2). These results demonstrate the ability of heteroatom composition to tune catalysis by using C_2H_4 dimerization catalysis as a test reaction with zeolite Beta supported Ni catalysts.

2.2 Introduction

Zeolites are widely used as supports for transition metal catalysts because of their size selecting features, highly uniform crystalline structure, and extra-framework cation exchange sites.[1–3] Zeolite frameworks are regular structures composed of TO_4 tetrahedra, where T is generally Si^{4+} but can be substituted with trivalent cations such Al^{3+}, Fe^{3+}, Ga^{3+}, and B^{3+} (referred to as the heteroatom).[4] The charge imbalance between Si^{4+} and the T^{3+} heteroatom is compensated by an extraframework cation such as Na^+. Zeolites are frequently used as solid acid catalysts with H^+ as the charge compensating extraframework cation. These cation exchange sites often become the support ligand sites of transition metals on zeolites. Zeolite supported metal catalysts have a wide variety of applications such as Zn, Cu, and Fe are commonly studied catalysts for relevant reactions such as alkene upgrading and selective catalytic reduction.[5–7]

Zeolites of the same framework (e.g. MFI, BEA) but with different heteroatoms have been observed to exhibit different catalytic activities in acid catalyzed reactions such as alkane cracking or methanol dehydration on the basis of the identity of the heteroatom.[8,9] Experimental measurements of the intrinsic acidity of a zeolite can be difficult to interpret due to convoluting effects when using probe molecules, such as interactions with the zeolite framework.[10] However, the theoretically calculated deprotonation energy (DPE) has appeared as a good descriptor, correlating well with activity of MFI zeolites for methanol dehydration.[8,11,12] In methanol dehydration, this outcome is because the rate constant in the zero-order kinetic regime is insensitive to van der Waals interactions. The differential DPE is related to the ability of the surface oxygens on the TO_4^- tetrahedra to stabilize the negative charge when various trivalent cations are substituted into the framework. Zeolite used as a solid acid catalyst with different heteroatoms have been observed to catalyze reactions such as methanol dehydration, alkane cracking, and toluene alkylation differently depending on the framework composition.[11,13,14]

When Na^+ or H^+ is replaced by a transition metal, one would expect changes in electron density of the supported metal. Because the support oxygens can be considered ligands on the supported metal,[15] this interaction is analogous to changing the ligands on an organometallic complex to alter the properties of the metal center. The resulting changes in electron density of the metal are anticipated to be consistent with reported differences in electron donating/withdrawing properties of the oxygens on the TO_4^- when the identity of the heteroatom is varied. Other methods that have been explored to influence a supported metal cation involve changing the zeolite framework or using a metal oxide support.[15] Since cation exchange sites are similar within a given zeolite framework[16], such as BEA, zeolite framework composition enables the creation of extraframework cation sites that are geometrically similar between chemically different zeolite supports.

C_2H_4 upgrading is an important class of reaction that enables the creation of longer hydrocarbon molecules from relatively simple building blocks, including those obtained from more sustainable sources.[17–20] The process can be environmentally friendly given C_2H_4 can be more sustainably produced from the conversion

of ethanol or methanol.[19,21,22] Many of the catalysts used are transition metals dispersed on zeolites such as Zn, Mo, and Rh for alkene/alkane aromatization and C_2H_4 dimerization respectively.[5,23,24] While Rh-based catalysts are highly active for C_2H_4 dimerization,[25] the relatively high cost of Rh motivates the investigation of other transition metal catalysts. Ni catalysts supported on aluminosilicate zeolites such as Beta, Y, and MCM-41 have been studied for C_2H_4 dimerization.[26–29] Selectivity of the catalyst depends, in part, upon the mechanism of dimerization, which can favor 1-butene or a mixture of linear butenes.[30,31] Additionally, the presence of acid sites can catalyze the skeletal isomerization of linear butenes to isobutene. In this work, we report the impact of framework elemental composition of Beta zeolites on the electron density of supported Ni cations, as well as the resulting catalytic activity and selectivity when used for C_2H_4 dimerization catalysis.

2.3 Experimental Methods

Catalyst Synthesis. Zeolites will be referred to as M-[X]-Beta, where M is the extraframework cation and X is the framework heteroatom. Na-[B]-Beta was synthesized by adapting a procedure from Reddy et al.[32] Typically 12.5g of colloidal SiO_2 (40 wt%, Alfa Aesar) was added to 15.8g of Tetraethylammonium hydroxide (TEAOH 35% in water, Alfa Aesar). A solution of 0.398g H_3BO_3 (Fischer Scientific) dissolved in 9.19g of H_2O was added to the previous solution and stirred for 1 h. A solution of 0.346g of NaOH (Honeywell) dissolved in 7.46g of H_2O was then added to the previous solution. The resulting gel ($10SiO_2$: 7.3TEAOH: $0.77H_3BO_3$: 1.0NaOH: $110H_2O$) turned opaque and viscous upon addition of the final solution, then was aged overnight at room temperature. After aging overnight, the solution was clear and was seeded with ca. 50mg of Na-[B]-Beta before being transferred to a 125 mL Teflon lined Parr autoclave vessel. Hydrothermal synthesis took place statically at 140°C for 11 days. Template removal was done by calcination at 600°C for 6 h, with a 1 h soak at 120°C and 2°C/min ramp rate. [Ga]-Beta was synthesized via heteroatom re-insertion done by post-synthetic treatment of Na-[B]-Beta.[33,34] Typically, 1.0g of Na-[B]-Beta was combined with 50mL of 0.25M $Ga(NO_3)_3$ in a thick walled glass round bottom pressure vessel. The solution was stirred at 80°C for 96 h, then centrifuged with DI water, NH_4 ion exchanged, and then

calcined at 400°C in 10% O_2 to obtain H-[Ga]-Beta. [Fe]-Beta was synthesized using a procedure from Raja et al.[35] Typically 0.0775g of NaOH and 0.0575g of KOH were added to 10.6g of 35% TEAOH. 3.00g of fumed SiO_2 was added to the solution and stirred for 4 h. A solution of 0.306g ferric sulfate (ACROS Organics) dissolved in 3.68g of H_2O was slowly added to the previous solution over 30 minutes. The solution ($10SiO_2$: 5.0TEAOH: $0.25Fe_2O_3$: 0.39NaOH: 0.21KOH: $41H_2O$) was then transferred to a 23mL Teflon liner in a Parr autoclave vessel, hydrothermal synthesis took place statically at 140°C for 15 days. The resulting white zeolite was washed with H_2O then calcined in 10% O_2 at 480°C for 4 h with a 1 h hold at 120°C and ramp rate of 2°C/min. [Al]-Beta zeolite with Si/Al=19 (NH_4-[Al]-Beta) was purchased from Zeolyst (CP814C). Zeolites were converted to NH_4-[X]-Beta via ion exchange by two consecutive exchanges mixing the zeolite with 1M NH_4NO_3 for 24 h at room temperature. Samples were converted to H-[X]-Beta by calcination in 10% O_2 (zero air, Praxair), 90% N_2 (99.999%, Praxair) at 600°C and 400°C for 6 h for NH_4-[Al]-Beta and NH_4-[Fe]-Beta respectively. [DeAl]-Beta was synthesized by dealuminating NH_4-[Al]-Beta in 13M HNO_3 at 80°C for 16 h. The sample was then calcined in 10% O_2 at 600°C for 4 h before Ni deposition.

Ni was dispersed on H-[X]-Beta zeolites by mixing the given support with $Ni(acac)_2$ (acac= acetylacetonate; STREM chemical, min 95%) and n-pentane in a Schlenk flask such that the Ni loading was 1wt% (±0.02%, exact Ni loading was calculated for each sample). The solution was stirred for 24 h and then the solvent was evacuated for 24 h. After evacuation, the sample was calcined in 10% O_2 at 550°C for 4 h with 2°C/min ramp rate, then transferred without exposure to air to a glovebox. All work was done in a glovebox or with a Schlenk line to exclude moisture and oxygen. Catalyst structure was determined by powdered x-ray diffraction (PXRD) and N_2 physisorption with details reported in the Supplemental Information (Figures S2.11-S2.14, Table S2.3). Catalyst structure was confirmed by powdered x-ray diffraction (PXRD) and N_2 physisorption with details reported in the Supplemental Information (Figures S2.11–S2.14, Table S2.3). The XRD patterns confirm the zeolite Beta crystal structure for all catalysts. N_2 adsorption

experiments before and after Ni loading, in which relatively small changes in surface area are observed, suggest the support is not significantly affected by the metal deposition.

FTIR. Samples stored in a glovebox were pressed into self-supporting wafers, with approximately 25mg of sample, then loaded into a Harrick high temperature transmission cell. Diffuse Reflectance cell measurements were performed with pure zeolitic samples. Fourier Transform Infrared Spectrometry (FTIR) spectra were taken by a Bruker Tensor II with $2cm^{-1}$ resolution and 128 scans collected per spectrum. For subtraction spectra, a spectrum (in N_2) before reactive gas (CO, NO, or C_2H_4) treatment was subtracted from the resulting spectra. N_2 (99.999%, Airgas) and C_2H_4 (99.998%, Matheson) were passed through traps containing reduced Cu and molecular sieve to remove oxygen and moisture respectively. CO (99.999%, Matheson) was passed through a trap containing γ-Al_2O_3 and molecular sieve to remove trace moisture and metal carbonyls.

Catalysis: C_2H_4 Hydrogenation. Catalysts, stored in an Ar-filled glovebox, were weighed directly into a 6.35mm OD quartz tube, and were diluted with 100mg of α-Al_2O_3. The samples in the quartz tube were transferred from the glovebox to a three-zone furnace with the exclusion of air and moisture. Prior to catalysis, samples were heated to 350°C for 2 h in N_2. After the samples were allowed to cool to 180°C, they were used for C_2H_4 dimerization. C_2H_4 dimerization was performed with all catalysts at 180°C, 2.16 kPa C_2H_4 or in a separate experiment with 8.66 kPa H_2 (99.999%, Praxair) at the same temperature and C_2H_4 partial pressure. C_2H_4 conversion was calculated via carbon balance by using a Gas Chromatograph equipped with a Flame Ionization Detector. Calibration was done with a custom gas mixture from Matheson. In all catalysis experiments the C_2H_4 conversion was kept between 2-6% unless otherwise noted. Blank reactions were run with the bare support; any activity was subtracted from the Ni based catalysts by assuming a consumption of $2H^+$ per Ni^{2+} cation.

2.4 Results and Discussion

C_2H_4 Adsorption.

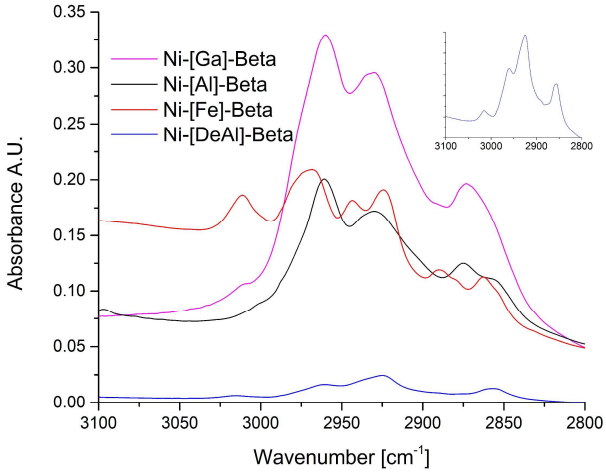

Figure 2.1. C_2H_4 adsorption at room temperature onto oxidized Ni-[X]-Beta catalysts. Bands uniquely in the Ni-[Fe]-Beta spectrum are assigned to adsorbed butene. The bands in the Ni-[Al]-Beta and Ni-[Ga]-Beta spectra are assigned to alkyl ligands of various length. Bands position and assignments are reported in Table 1.

C_2H_4 adsorption spectra of Ni-[X]-Beta zeolites are shown in Figure 2.1. Ni-[Ga]-Beta and Ni-[Al]-Beta share a set bands assigned to alkyl ligands,[36,37] reported in Table 2.1, at 2957, 2923, 2872, and 2846 cm^{-1}. In addition to these bands the Ni-[Ga]-Beta exhibits bands at 3013, 2944, 2890 and 2864 cm^{-1}, shown in Figure S2.1, which are shared with Ni-[Fe]-Beta. Ni-[Fe]-Beta is also characterized by bands, which are listed in Table 2.1, at 3013, 2968, 2943, 2925, 2890, and 2863 cm^{-1}. These bands likely correspond to butene adsorbed to silanol and Ni sites.[38] The Ni-[Ga]-Beta, Ni-[Al]-Beta, and Ni-[Fe]-Beta samples showed a decrease in absorbance due to terminal and bridging acidic silanols (3741 and 3636[Fe], 3618[Ga], 3605[Al] cm^{-1}, respectively)[39–41] suggesting that dimerization products adsorb to acid sites at room temperature. C_2H_4 adsorption onto Ni-[DeAl]-Beta resulted in bands at 3016, 2961, 2925, and 2857 cm^{-1}; 3016 cm^{-1} is assigned to π-bonded C_2H_4

while the rest are assigned to alkyl ligands.[42] Experiments with the bare support, which lacks dispersed Ni, did not show decreased silanol absorbance after dosing C_2H_4, providing more evidence for the adsorption of dimerization/hydrogenation products to silanols. The control experiments without dispersed Ni also provide evidence that extraframework heteroatoms are not interacting directly with C_2H_4. C_2H_4 adsorption gives some insight into how the Ni sites interact differently with C_2H_4. Ni-[Al]-Beta and Ni-[Ga]-Beta have similar bands representative of alkyl ligands on the Ni sites. In addition to these alkyl bands, Figure S2.15 shows the bands corresponding to isolated silanols and briding acidic silanols (3740 and 3618 cm^{-1}, respectively for Ni-[Ga]-Beta, 3740 and 3607 cm^{-1} respectively for Ni-[Al]-Beta)[40,43] decreased. No increase or decrease of OH bands was observed when C_2H_4 adsorption was performed with the bare support, suggesting that products of dimerization could be adsorbed to various silanol sites. An alternative explanation is that silanols near Ni sites are participating in the adsorption/catalysis of C_2H_4. However, isolated silanol bands decreased as well and by lack of proximity should not be interacting with the Ni sites; therefore observed this decrease in absorbance is more consistent with the adsorption/hydrogenation of products rather than C_2H_4.

Table 2.1. Bands after C_2H_4 adsorption at room temperature onto oxidized Ni-[X]-Beta catalysts. Bands with marked with * are transient and decrease with increasing time after C_2H_4 exposure.

Catalyst	Butene Bands		Alkyl Bands	
Ni-[Al]-Beta	-	-	2957, 2923,	2872, 2856
Ni-[DeAl]-Beta	-	-	3016, 2961	2925, 2857
Ni-[Fe]-Beta	3013, 2968, 2943	2924, 2890, 2863, 2854	-	-
Ni-[Ga]-Beta	*3013, *2944	*2890, *2864	2960, 2932, 2873	

CO and NO Adsorption: Electron Density of Metal Center.

The relative electron density of the Ni cations was probed with CO and NO adsorption Ni-[X]-Beta because these probe molecules are sensitive to the electron density of Ni. A reduction was done before CO adsorption because on the Ni^{+} carbonyls, and not Ni^{2+} carbonyls, are sensitive to the electron density of the Ni cation.[44] CO adsorption was performed at 30°C on all catalysts after reducing the Ni sites in 10% CO,

balance N_2, at 300°C for 15 minutes and cooling in N_2 to 30°C. CO was then dosed into the cell and spectra were recorded as CO was purged out of the cell with N_2. The spectra for Ni-[Al]-Beta, Ni-[Ga]-Beta, and Ni-[Fe]-Beta, shown in Figures S2.2, S2.3 and S2.4, respectively, follow similar patterns with Ni^{2+}-CO being present as well as Ni^{+}-$(CO)_2$ that decompose into Ni^{+}-CO with increasing time after CO pulse. Band positions and assignment of the Ni carbonyls are given in Table 2.2. In addition to Ni carbonyl bands, Ni-[Fe]-Beta, shown in Figure S2.4, also exhibits a band at 2183 cm^{-1}. This band corresponds to Fe^{2+}-CO likely formed from the reduction of extraframework Fe_2O_3.

Table 2.2. Summary of carbonyl bands after samples were reduced in 10% CO at 300°C and nitrosyl bands of NO adsorption onto oxidized materials.

Catalyst	Ni^{2+}-CO	Ni^{+}-$(CO)_{2ss}$	Ni^{+}-$(CO)_{2as}$	Ni^{+}-CO	Ni^{+}-$(CO)_x$	Ni^{2+}-$(NO)_x$
Ni-[Al]-Beta	2212	2138	2096	2112	-	1896, 1888, 1874
Ni-[Ga]-Beta	2209	2136	2092	2107	-	1893, 1903, 1898, 1886, 1839
Ni-[Fe]-Beta	2207	2133	2089	2103	-	1889, 1865, 1841
Ni-[DeAl]-Beta	2197			2090	2137, 2124, 2074	1879, 1834, 1869

Figure S2.5 shows CO adsorption onto Ni-[DeAl]-Beta. Bands at 2197, 2136, 2125, 2074, and 2090 cm^{-1} are assigned to Ni^{2+}-CO, Ni^{+}-$(CO)_2$, Ni^{+}-$(CO)_2$, Ni^{+}-$(CO)_2$ Ni^{+}-(CO), respectively, re-occupying empty silanol nests that were previously occupied by Al, where the 2125 and 2136 cm^{-1} bands are assigned to complex specified carbonyls. All assignments agree with previous literature, except for the 2074 and 2090 cm^{-1} bands which will be discussed.[43] At high CO coverages, shortly after the CO pulse, the bands at 2125 cm^{-1} and 2074 cm^{-1} dominate the spectra and decrease with increasing time after the CO pulse. The band at 2090 cm^{-1} grows as the 2125 and 2074 cm^{-1} bands decrease. An isosbestic point at 2083 cm^{-1} indicates a direct conversion of a dicarbonyl (Ni^{+}-$(CO)_2$), 2074 cm^{-1}, to a monocarbonyl (Ni^{+}-(CO)) at 2090 cm^{-1}. These assignments are the opposite of those reported for low temperature CO adsorption, however we believe the clear isosbestic feature in our data confirms our assignment. NO adsorption was performed at room temperature on previously oxidized catalysts. A comparison of NO adsorption spectra, characterizing

Ni-[X]-Beta catalysts, is shown in Figure S2.6. NO was repeatedly dosed into the FTIR cell and spectra were recorded. The NO adsorption bands for all catalysts are summarized in Table 2. Ni-[Al]-Beta has bands at 1896, 1888, and 1874 cm^{-1}, 1896 cm^{-1} has been previously been assigned to Ni^{2+}-NO in extraframework cation exchange sites.[43] Bands at 1888 and 1874 cm^{-1} are likely due to Ni^{2+}-$(NO)_2$ as they are similar to those assigned in Ni-[Al]-MFI but we have insufficient evidence to make definitive assignments. It is worth noting that there is lack of consensus on the assignment as the Ni-[Al]-MFI bands have been separately assigned to Ni^{2+}-$(NO)_2$ and Ni^{2+}-NO.[45,46]Analogously, Ni-[Fe]-Beta bands at 1889, 1865, and 1841 cm^{-1} are likely due to Ni^{2+}-NO and Ni^{2+}-$(NO)_2$, Ni^{2+}-$(NO)_2$ respectively. Bands observed on Ni-[Ga]-Beta at 1903, 1898, and 1893 cm^{-1} are likely Ni^{2+}-NO, while 1886 and 1839 cm^{-1} are likely Ni^{2+}-$(NO)_2$. However, due to the complexity of the spectra and relatively small amount of literature these assignments are tentative. The Ni-[DeAl]-Beta NO adsorption has bands at 1879, 1869 and 1834 cm^{-1} which have been previously assigned to Ni^{2+}-NO of Ni reoccupying silanol nests.[47]

The relative electron density of the Ni cations was probed with CO and NO adsorption. Band assignments for CO adsorption are listed in Table 2.2, with the desorption spectra shown in Figures S2.2–S2.5. The Ni^{+}-$(CO)_{2as}$ bands for the Ni-[X]-Beta catalysts are 2096, 2093, and 2091 cm^{-1} for X= [Al], [Ga], and [Fe] respectively. The decrease in wavenumber of this band is consistent with a more electron dense Ni cation in the order [Fe]>[Ga]>[Al]. NO adsorption onto oxidized catalysts follow the same trend as CO adsorption with Ni-NO bands decreasing in the order [Fe]<[Ga]<[Al]. Although we did not directly probe the oxidation state of the Ni sites during catalysis, it is likely the Ni^{2+} is the active oxidation state given the recent experimental and theoretical reports of Ni^{2+} being active while Ni^{+} is a spectator species.[27,29,30,48] However, it is worth noting that there are reports of the C_2H_4 dimerization activity correlated with concentration of Ni^{+} sites.[49]

C_2H_4 Dimerization Activity and Selectivity.

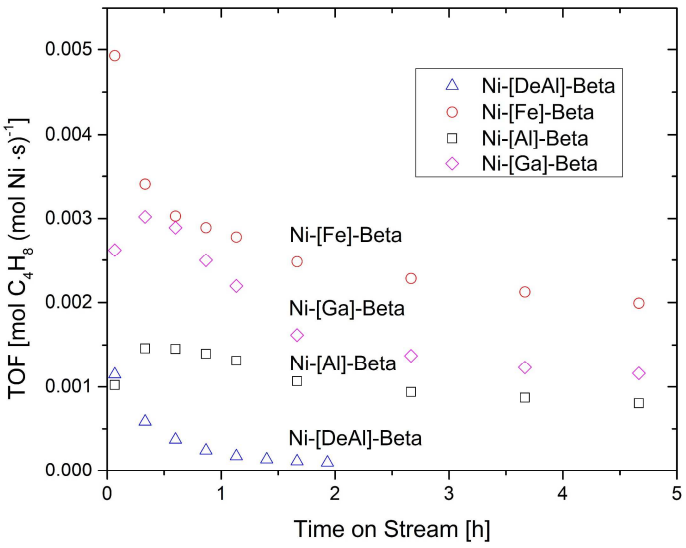

Figure 2.2. Turnover frequency of butene formation for Ni-[X]-Beta catalysts at 180°C and 2.16 kPa C_2H_4. No activation period is observed when [Fe]- or [DeAl]-Beta was used as the support.

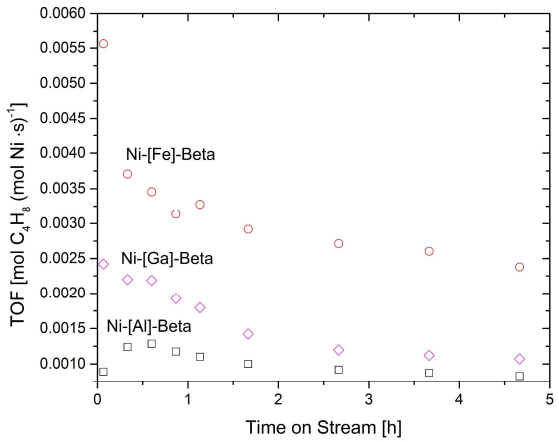

Figure 2.3. Turnover frequency of butene formation in the presence of H_2 for Ni-[X]-Beta catalysts at 180°C, 2.16 kPa C_2H_4, and 8.66kPa H_2. The activation period is observed for Ni-[Al]-Beta but none of the other catalyst test in the presence of H_2.

Butene formation turnover frequency in the absence of H_2 is presented in Figure 2.2. Ni-[Al]-Beta and Ni-[Ga]-Beta exhibit activation periods at short times-on-stream, approximately 0.5 h, while the other catalysts do not show this behavior. Summarized in Table 2.3. when comparing the activity

of these catalysts for C_2H_4 dimerization, the relative activity per mole of supported Ni is in the order Ni-[Fe]-Beta > Ni-[Ga]-Beta > Ni-[Al]-Beta > Ni-[DeAl]-Beta ranging from 2.12×10^{-3}–1.00×10^{-4} [mol C_4H_8 (mol Ni s)$^{-1}$]. Dimerization in the presence of H_2, shown in Figure 2.3, follows the same trend in relative activity, however an activation period is only observed with Ni-[Al]-Beta. Ni-[DeAl]-Beta is omitted from this because the activity for dimerization in the presence of H_2 is essentially zero, with a 99.9% selectivity towards C_2H_4 hydrogenation. Comparisons between individual catalysts with and without H_2 can be seen in Figures S2.7–S2.9. Activity towards butene formation in the presence of H_2 decreases for Ni-[Al]-Beta and Ni-[Ga]-Beta but results in an average 1.2-fold increase with Ni-[Fe]-Beta. Butene selectivity for catalyst in the absence of H_2 is shown in Figure 2.4. At 3.67 h on stream, all catalysts exhibit high selectivity, 92–98%, towards butene formation but at shorter times on stream, a lower selectivity for some catalysts of 0.30, 0.69, 0.90, 0.98 for Ni-[Al]-, [Ga]-, [DeAl]-, and [Fe]-Beta respectively. In the presence of H_2, the selectivities, shown in Figure 2.5, at 3.67 h time-on-stream decrease for all catalysts to 0.10, 0.44, 0.0, 0.52 for Ni-[Al]-, [Ga]-, [DeAl]-, and [Fe]-Beta respectively. All catalysts except for Ni-[DeAl]-Beta show a similar trend of increasing butene selectivity until ca. 1.25 h time-on-stream and then decreasing butene selectivity.

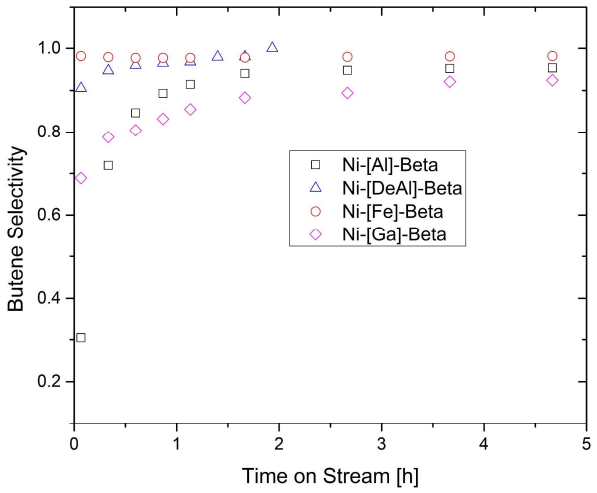

Figure 2.4. Selectivity of butenes relative to total product formation for catalysts in the absence of H_2. Ni-[Ga] and Ni-[Al]-Beta exhibit similar trends in butene selectivity, including isobutene, starting low and increasing to ~90% after 2 h TOS. This change in selectivity over time is consistent with an TOF induction period observed during catalysis. Reaction conditions: 180°C and 2.16 kPa C_2H_4

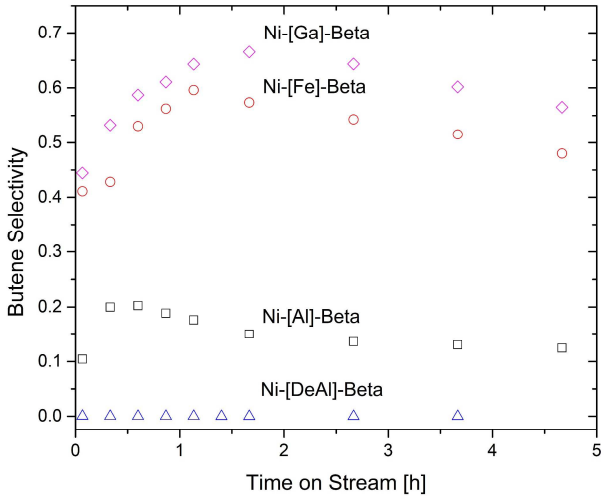

Figure 2.5. Selectivity to butenes on the basis of total product formation for conversions in the presence of H_2. Except for Ni-[DeAl]-Beta, each catalyst exhibits the same trend in selectivity with increasing TOS. Reaction conditions: 180°C, 2.16 kPa C_2H_4, and 8.66k Pa H_2.

The relative activity in terms of moles of butene produced per mole of Ni increases in the order Ni-[Fe]-Beta > Ni-[Ga]-Beta > Ni-[Al]-Beta. Catalyst was performed with the bare zeolite, before Ni was dispersed, to determine the effects of acid sites and/or extra-framework species on catalysis. H-[Al]-Beta and H-[Ga]-Beta had measurable but relatively low activity compared to Ni-[Al]-Beta and Ni-[Ga]-Beta. H-[Fe]-Beta had no measurable activity indicating that the acid sites and extra-framework species are not active for C_2H_4 dimerization under these conditions. An activation period is observed with Ni-[Al]-Beta and Ni-[Ga]-Beta, which is not observed with the other catalysts. This activation period may be associated with the formation of the active site (Ni(II)-hydride or Ni(II)-alkyl/hydride).[30,36] The lack of observation of the activation period with Ni-[Fe]-Beta and Ni-[DeAl]-Beta, suggests that the formation of this active site is significantly faster on these catalysts than on Ni-[Al]-Beta or Ni-[Ga]-Beta. The activity of the catalysts increases in the order Ni-[Fe]-Beta > Ni-[Ga]-Beta > Ni-[Al]-Beta which is also the order of electron density of the Ni

cations as observed with CO adsorption. There are proposals of the active site being Ni(II)OH for dimerization that is formed due to Ni exchanging with a single Al site, instead of a paired Al site.[50] We think it is unlikely that Ni(II)OH would survive our oxidative treatment before catalysis, as there have been literature that suggests Ni(II)OH condenses to a Ni oxo-form after thermal treatment on Ni exchanged MFI.[45] While we don't have enough information to determine if the Ni cations are associated with a single or paired Al site, the Ni/[X] ratios, presented in table S2.2, are low enough, and within the range of Co exchanges done in Beta by Dědeček et al, it is it likely most Ni are sitting in paired Al sites. However, due to the difficulty of identifying whether a cation is at a paired or isolated site we cannot definitively assign the Ni cations to isolated or paired [X] sites. The increase in activity suggests that the Ni sites in Ni-[Fe]-Beta better at stabilizing transition states mediating the formation of the Ni-butene complex proposed to be the rate limiting step.[48] In comparison to the Beta-supported Ni, Rh-Y catalysts are more active. When operating at P_{C2H4} = 40 kPa, T = 30°C, the TOF with Rh-Y is 10.8×10^{-3} s^{-1} and 58.5×10^{-3} s^{-1} (with 10 kPa H_2).[25] When using [Fe]-Beta as a support to tune dispersed Ni, which is Earth-abundant and less expensive, a TOF within an order of magnitude of that of Rh-Y was achieved in the absence of co-fed H_2.

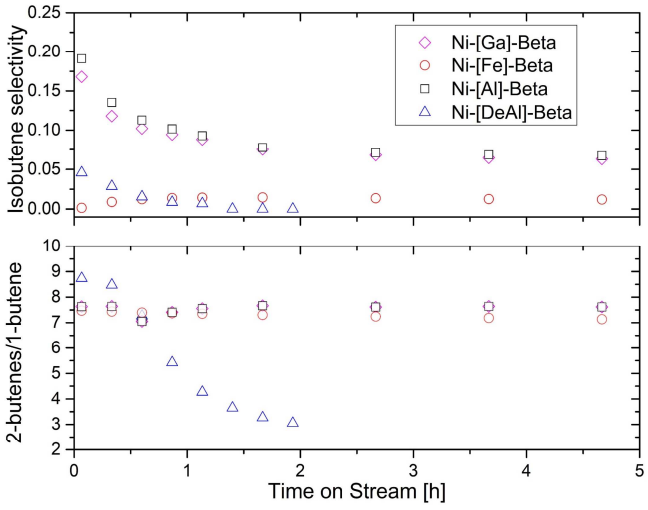

Figure 2.6. Top: Selectivity of isobutene relative to total butene formation. Bottom: ratio of total 2-butene formation to 1-butene. Results for dimerization carried out in the absence of H_2.

Table 2.3. Summary of catalysis with materials at 180°C and 2.16kPa C_2H_4 at 3.7 h time on stream. TOF units: [mol C_4H_8 (mol Ni s)$^{-1}$], selectivity presented as moles of listed product per mole of total product formation.

Catalyst	TOF x10^3	Butenes	Ethane	Isobutene	2-butenes /1-butene	$TOF_{3.7}/TOF_i$
Ni-[Al]-Beta	0.87	0.95	0.023	0.068	7.6	0.75
Ni-[Ga]-Beta	1.2	0.98	0.016	0.065	7.6	0.70
Ni-[Fe]-Beta	2.1	0.98	0.019	0.013	7.2	0.80
Ni-[DeAl]-Beta	0.10	1.0	0.0	0.0	3.1	0.09

The DPE is calculated as the energy difference between a neutral zeolite framework and a non-interacting gas phase proton and negatively charged zeolite framework.[8,12] In the case of C_2H_4 dimerization it is likely that charged carbocation intermediates interact with the zeolite framework causing framework distortion of the heteroatom sites.[53] These framework distortions are likely different between H-[Ga]-Beta and H-[Fe]-Beta resulting in different activities for C_2H_4 dimerization and butene isomerization despite similar acid site strength. The zeolite heteroatom elemental composition influences the activity of the supported Ni cation, as well as the activity of the acid sites for C_2H_4 dimerization.

The overall selectivity towards butenes as well as the ratio of 2-butenes to 1-butene were characterized in order to understand more about the possible mechanism of dimerization between the catalysts as well as the isomerization activity of the catalysts. The insertion-coordination (Cossee-Arlman) mechanism has been observed on Ni dispersed on aluminosilicates.[30,54,55] The metallacyclic mechanism selectively produces 1-butene[30,31], while the Cossee-Arlman mechanism produces a mixture of 1-butene, cis-2-butene and trans-2-butene. In addition to this distribution of isomers, acid sites (as well as Ni sites) in aluminosilicates have been observed to be active for the skeletal isomerization of linear butenes. The 2-butene/1-butene ratios (Figure 2.6) are consistent with the Cossee-Arlman mechanism for all the catalysts tested.

Although the theoretical acid site strength of Fe substituted zeolites should be similar to that of Ga substituted zeolites (as demonstrated for methanol dehydration), Ni-[Fe]-Beta had higher selectivity towards linear butenes, shown in Figure 2.6, than Ni-[Ga]-Beta while operating at a similar

conversion. This suggests the residual acid sites present in Ni-[Fe]-Beta are significantly less able to catalyze the skeletal isomerization of linear butene to isobutene. The Si/X ratio between [Fe]- and [Ga]-Beta are similar as seen in Table S2.2 suggesting that there are not a lack of H^+ sites on Ni-[Fe]-Beta compared to Ni-[Ga]-Beta. In addition, catalysis experiments with H-[Fe]-Beta showed no activity for dimerization, in contrast with H-[Ga]-Beta which had some activity for C_2H_4 dimerization. The results show that butene selectivity due to Ni sites, as well as H^+ sites, is altered by changing of the zeolite framework heteroatom composition. Overall selectivity to butenes is enhanced, especially at short times-on-stream, by using the zeolite hereroatom to tune the dispersed Ni.

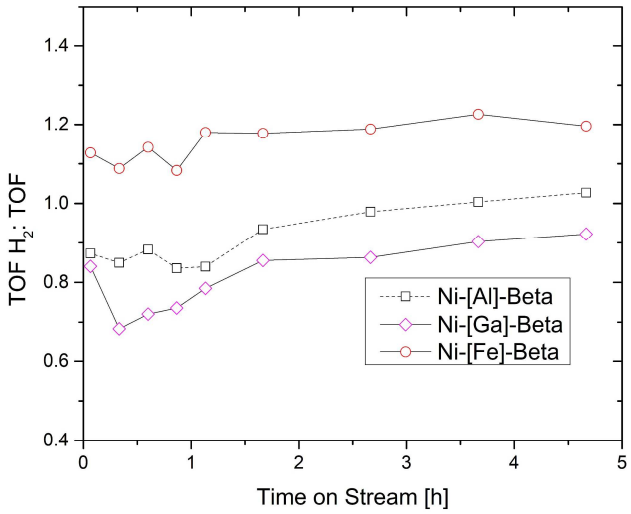

Figure 2.7. The ratio of TOF [mol C_4H_8 (mol Ni s)$^{-1}$] in the presence of H_2 to TOF in the absence of H_2. Ni-[Ga]-Beta and Ni-[Al]-Beta see a decrease in TOF while Ni-[Fe]-Beta sees an increase.

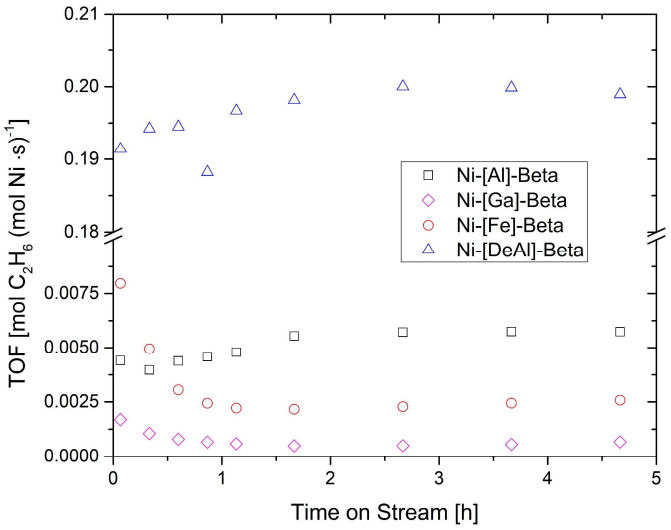

Figure 2.8. C_2H_6 production rate for the given catalysts in the presence of H_2 (T=180°C; 2.16 kPa C_2H_4, 8.66kPa H_2). The Ni-[DeAl]-Beta TOF is not a true reaction rate due to the operation at 99.9% C_2H_4 conversion.

The addition of co-fed H_2 was examined because it has been demonstrated to enhance catalytic activity in some catalysts[56] and may assist in creating the active site for C_2H_4 dimerization.[30,54] In addition, it is possible that co-feeding H_2 increases stability of the catalyst by creating conditions where products that would otherwise deactivate Ni sites can be desorbed. Ni-[Fe]-Beta was shown, in Figure 2.7, to be ca. 1.2-fold more active when H_2 is present in the feed stream. The sample with the most significant change in activity, shown in Figure 2.8, was Ni-[DeAl]-Beta, which switched from ca. 98% selectivity toward butenes (a dimerization product) in the absence of H_2 to 100% selectivity towards C_2H_6 (a hydrogenation product) in the presence of H_2. In the presence of H_2, Ni-[DeAl]-Beta operated at nearly 100% conversion operating at W/F = 5.0 s^{-1} compared to W/F = 8.7 s^{-1} and 1.1% conversion in the absence of H_2.

Future work will elucidate details for this dramatic change in activity of Ni-[DeAl]-Beta, but it is possible that cationic Ni re-occupying empty silanol nests is highly active for C_2H_4 hydrogenation. As shown in Figure 2.7, the overall rate of butene production was ca. 0.9-fold lower than in the absence of H_2 at more than 2 h on stream for Ni-[Ga]-Beta and approximately the same for Ni-[Al]-

Beta. The rate of deactivation decreases upon the addition of co-fed H_2 for all the catalysts. The rates of deactivation in the last 3 h of catalysis for each catalyst are reported in Table S2.1. Mechanisms of deactivation have been proposed to be accumulation of large hydrocarbon products that do not desorb from Ni sites, which prevent the sites from participating in further dimerization catalysis. It is likely that the addition of H_2 helps to prevent this buildup of large molecular weight products by hydrogenating intermediates before they can become too large to desorb from active sites. The role of zeolite heteroatom resulted in enhancing activity of supported Ni when the heteroatom was Fe, while reducing activity when the heteroatom was Al or Ga, and most dramatically shifting conversion completely to hydrogenation products when a dealuminated Beta support [DeAl] was used.

2.5 Conclusions

Ni was dispersed on Beta zeolites with different framework heteroatoms: Al, Ga, and Fe. Differences in electron density of the supported Ni cations were observed by using CO and NO adsorption experiments. Dosing of C_2H_4 at room temperature revealed differences in adsorbed species between the catalysts. Ni-[Al]- and Ni-[Ga]-Beta showed adsorbed alkyl species of unknown degree of oligomerization, while Ni-[Fe]-Beta exhibited bands representative of adsorbed butenes. C_2H_4 dimerization activity in the absence of H_2 increased in the order Ni-[Fe]-Beta > Ni-[Ga]-Beta > Ni-[Al]-Beta > Ni-[DeAl]-Beta. Despite the similarities in the acid site strength between [Ga]-Beta and [Fe]-Beta, both the Ni and H^+ sites present in each catalyst have different activity and selective for dimerization. Ni-[Fe]-Beta had higher activity and selectivity for butene formation than Ni-[Ga]-Beta. The acid sites on H-[Ga]-Beta and H-[Fe]-Beta also exhibited different activity for the dimerization of C_2H_4, as well as the skeletal isomerization of linear butenes. In the presence of co-fed H_2 the relative order of dimerization activity remained the same. The introduction of H_2 to dimerization increased the activity of Ni-[Fe]-Beta, while Ni-[Al]-Beta and Ni-[Ga]-Beta saw little change or a slight decrease in activity. The overall selectivity towards

butenes decreased due to an increase in hydrogenation products. The Ni-[DeAl]-Beta catalyst exhibited high activity and selectivity towards C_2H_4 hydrogenation in the presence of H_2. These results highlight the role of heteroatom in tuning the electronic properties of the supported Ni cation, for selective adsorption and dimerization catalysis.

2.6 Conflicts of Interest

There are no conflicts to declare.

2.7 Acknowledgements

The authors would like to acknowledge support from the Rossi Endowment at UC Davis (RR).

2.8 References

1 B. C. Gates, M. Flytzani-Stephanopoulos, D. A. Dixon and A. Katz, *Catal. Sci. Technol.*, 2017, **7**, 4259–4275.

2 E. F. Iliopoulou, S. D. Stefanidis, K. G. Kalogiannis, A. Delimitis, A. A. Lappas and K. S. Triantafyllidis, *Appl. Catal. B Environ.*, 2012, **127**, 281–290.

3 N. Kosinov, C. Liu, E. J. M. Hensen and E. A. Pidko, *Chem. Mater.*, 2018, **30**, 3177–3198.

4 R. Aiello, J. B. Nagy, G. Giordano, A. Katovic and F. Testa, *Comptes Rendus Chim.*, 2005, **8**, 321–329.

5 A. Mehdad and R. F. Lobo, *Catal. Sci. Technol.*, 2017, **7**, 3562–3572.

6 J. Pérez-Ramírez, M. S. Kumar and A. Brückner, *J. Catal.*, , DOI:10.1016/j.jcat.2004.01.007.

7 M. Colombo, I. Nova and E. Tronconi, *Catal. Today*, 2010, **151**, 223–230.

8 A. J. Jones, R. T. Carr, S. I. Zones and E. Iglesia, *J. Catal.*, 2014, **312**, 58–68.

9 W. E. Farneth and R. J. Gorte, *Chem. Rev.*, 1995, **95**, 615–635.

10 M. Boronat and A. Corma, *ACS Catal.*, 2019, **9**, 1539–1548.

11 A. J. Jones and E. Iglesia, *ACS Catal.*, 2015, **5**, 5741–5755.

12 J. Sauer, *J. Mol. Catal.*, 1989, **54**, 312–323.

13 D. Vitvarová, L. Kurfiřtová, M. Kubů and N. Žilková, *Microporous Mesoporous Mater.*, 2014, **194**, 174–182.

14 R. J. Gorte, *Catal. Letters*, 1999, **62**, 1–13.

15 J. Lu, C. Aydin, N. D. Browning and B. C. Gates, *Langmuir*, 2012, **28**, 12806–12815.

16 J. Dědeček, L. Čapek, D. Kaucký, Z. Sobalík and B. Wichterlová, *J. Catal.*, 2002, **211**, 198–207.

17 A. Finiels, F. Fajula and V. Hulea, *Catal. Sci. Technol.*, 2014, **4**, 2412–2426.

18 G. Q. Chen and M. K. Patel, *Chem. Rev.*, 2012, **112**, 2082–2099.

19 A. Morschbacker, *Polym. Rev.*, 2009, **49**, 79–84.

20 Y. T. Kuo, G. A. Almansa and B. J. Vreugdenhil, *Appl. Energy*, 2018, **215**, 21–30.

21 P. Tian, Y. Wei, M. Ye and Z. Liu, *ACS Catal.*, 2015, **5**, 1922–1938.

22 Z. Li, N. M. Schweitzer, A. B. League, V. Bernales, A. W. Peters, A. B. Getsoian, T. C. Wang, J. T. Miller, A. Vjunov, J. L. Fulton, J. A. Lercher, C. J. Cramer, L. Gagliardi, J. T. Hupp and O. K. Farha, *J. Am. Chem. Soc.*, 2016, **138**, 1977–1982.

23 P. Zhu, G. Yang, J. Sun, R. Fan, P. Zhang, Y. Yoneyama and N. Tsubaki, *J. Mater. Chem. A*, 2017, **5**, 8599–8607.

24 V. Bernales, D. Yang, J. Yu, G. Gümüşlu, C. J. Cramer, B. C. Gates and L. Gagliardi, *ACS Appl. Mater. Interfaces*, 2017, **9**, 33511–33520.

25 P. Serna and B. C. Gates, *Angew. Chemie - Int. Ed.*, 2011, **50**, 5528–5531.

26 V. Hulea and F. Fajula, *J. Catal.*, 2004, **225**, 213–222.

27 A. Martínez, M. A. Arribas, P. Concepción and S. Moussa, *Appl. Catal. A Gen.*, 2013, **467**, 509–518.

28 I. Agirrezabal-Telleria and E. Iglesia, *J. Catal.*, 2017, **352**, 505–514.

29 N. R. Jaegers, K. Khivantsev, L. Kovarik, D. W. Klas, J. Z. Hu, Y. Wang and J. Szanyi, *Catal. Sci. Technol.*, 2019, **9**, 6570–6576.

30 R. Joshi, G. Zhang, J. T. Miller and R. Gounder, *ACS Catal.*, 2018, 11407–11422.

31 D. S. McGuinness, *Chem. Rev.*, 2011, **111**, 2321–2341.

32 K. S. N. Reddy, M. J. Eapen, P. N. Joshi, S. P. Mirajkar and V. P. Shiralkar, *J. Incl. Phenom. Mol. Recognit. Chem.*, 1994, **20**, 197–210.

33 S. I. Zones, A. Benin, S. J. Hwang, D. Xie, S. Elomari and M. F. Hsieh, *J. Am. Chem. Soc.*, 2014, **136**, 1462–1471.

34 H. Koller, C. Y. Chen and S. I. Zones, *Top. Catal.*, 2015, **58**, 451–479.

35 S. S. and K. L. Anuj Raj, 1993, 207–213.

36 S. Moussa, P. Concepción, M. A. Arribas and A. Martínez, *ACS Catal.*, 2018, **8**, 3903–3912.

37 M. Tanaka, A. Itadani, Y. Kuroda and M. Iwamoto, *J. Phys. Chem. C*, 2012, **116**, 5664–5672.

38 J. Datka and E. Kukulska-Zając, *J. Phys. Chem. B*, 2004, **108**, 17760–17766.

39 K. Hadjiivanov, E. Ivanova, R. Kefirov, J. Janas, A. Plesniar, S. Dzwigaj and M. Che, *Microporous Mesoporous Mater.*, 2010, **131**, 1–12.

40 K. A. Al-Majnouni, N. D. Hould, W. W. Lonergan, D. G. Vlachos and R. F. Lobo, *J. Phys. Chem. C*, 2010, **114**, 19395–19405.

41 I. Kiricsi, C. Flego, G. Pazzuconi, W. O. Parker, R. Millini, C. Perego and G. Bellussi, *J. Phys. Chem.*, 1994, **98**, 4627–4634.

42 A. M. Argo, J. F. Odzak, F. S. Lai and B. C. Gates, *Nature*, 2002, **415**, 623–626.

43 A. Penkova, S. Dzwigaj, W. R. Kefirov, K. Hadjiivanov and M. Che, *J. Phys. Chem. C*, 2007, **111**, 8623–8631.

44 M. Mihaylov, O. Lagunov, E. Ivanova and K. Hadjiivanov, *Top. Catal.*, 2011, **54**, 308–317.

45 K. Góra-Marek, A. Glanowska and J. Datka, *Microporous Mesoporous Mater.*, 2012, **158**, 162–169.

46 M. Mihaylov and K. Hadjiivanov, *Langmuir*, 2002, **18**, 4376–4383.

47 A. Penkova, S. Dzwigaj, W. R. Kefirov, K. Hadjiivanov and M. Che, *J. Phys. Chem. C*, 2007, **111**, 8623–8631.

48 R. Y. Brogaard and U. Olsbye, *ACS Catal.*, 2016, **6**, 1205–1214.

49 H. Choo and L. Kevan, *J. Phys. Chem. B*, 2001, 6353–6360.

50 I. Agirrezabal-Telleria and E. Iglesia, *J. Catal.*, 2020, **389**, 690–705.

51 R. E. Patet, M. Koehle, R. F. Lobo, S. Caratzoulas and D. G. Vlachos, *J. Phys. Chem. C*, 2017, **121**, 13666–13679.

52 D. J. Parrillo, C. Lee, R. J. Gorte, D. White and W. E. Farneth, *J. Phys. Chem.*, 1995, **99**, 8745–8749.

53 M. L. Sarazen and E. Iglesia, *Proc. Natl. Acad. Sci. U. S. A.*, 2017, **114**, E3900–E3908.

54 M. Lallemand, A. Finiels, F. Fajula and V. Hulea, *J. Phys. Chem. C*, 2009, **113**, 20360–20364.

55 R. D. Andrei, M. I. Popa, F. Fajula and V. Hulea, *J. Catal.*, 2015, **323**, 76–84.

56 P. Serna and B. C. Gates, *J. Am. Chem. Soc.*, 2011, **133**, 4714–4717.

2.9 Supporting Information

Supporting Information Table of Contents

Supporting Information.

N_2 Physisorption. Samples, loaded into a capped tube in the glovebox to exclude exposure to moisture and air, were transferred to a Micromeritics 3Flex instrument and degassed at 350°C for 4 h before measurements under dynamic vacuum. Samples were weighed in a glovebox before and after analysis to ensure a dry weight was obtained. N_2 adsorption isotherms were taken at -196°C. BET surface area was determined in the relative pressure range 0.001-0.05. Micropore volume was calculated using the t-plot method using Harkins-Jura thickness equation relating relative pressure to thickness of adsorbed layer.

Acid Site Titration. Acid site titration with isopropylamine was performed in a Netzsch Jupiter F209 TGA-MS. The sample was exposed to isopropylamine in-situ at 30°C. The sample was then heated to 527°C at 5°C/min in N_2, 80mL/min total flow, with a 1 hour hold at 180°C to remove physisorbed isopropylamine. The mass to charge ratios 17 (ammonia), 41 (propene), 44 (isopropylamine), and 58 (isopropylamine) were monitored during the experiment.

Table S2.1. Rate of deactivation of catalysts of the last 3 h of catalysis.

	Deactivation over 3 h		
Catalyst	No H_2	H_2	H_2 – No H_2
Ni-[Al]-Beta	25%	17%	-8%
Ni-[Ga]-Beta	30%	25%	-5%
Ni-[Fe]-Beta	20%	18%	-2%
Ni-[DeAl]-Beta	91%	-	-

Table S2.2. Acid site density, Si/X, and Ni/X of [X]-Beta zeolites. [a]Determined via isopropylamine titration, [b]determined via ICP-MS.

Heteroatom	Acid Site Density[a] [μmol/g]	Si/X[a]	Si/X[b]	Ni/H$^+$	Ni/X[b]
Al	735	22	19	0.24	0.21
Ga	616	25	24	0.27	0.27
Fe	712	22	19	0.24	0.22

Table S2.3. Surface areas and micropore volumes of catalysts derived from nitrogen physisorption

Extra-Framework Cation	Heteroatom	BET SA [m²/g]	Micropore Vol [cm³/g]	External SA [m²/g]
Na^+	B	699	0.239	68.5
H^+	Ga	665	0.199	159
Ni, H^+	Ga	643	0.188	169
H^+	Al	694	0.204	174
Ni, H^+	Al	690	0.201	184
-	DeAl	599	0.17	156
Ni	DeAl	632	0.19	145
H^+	Fe	705	0.204	186
Ni, H^+	Fe	695	0.220	128

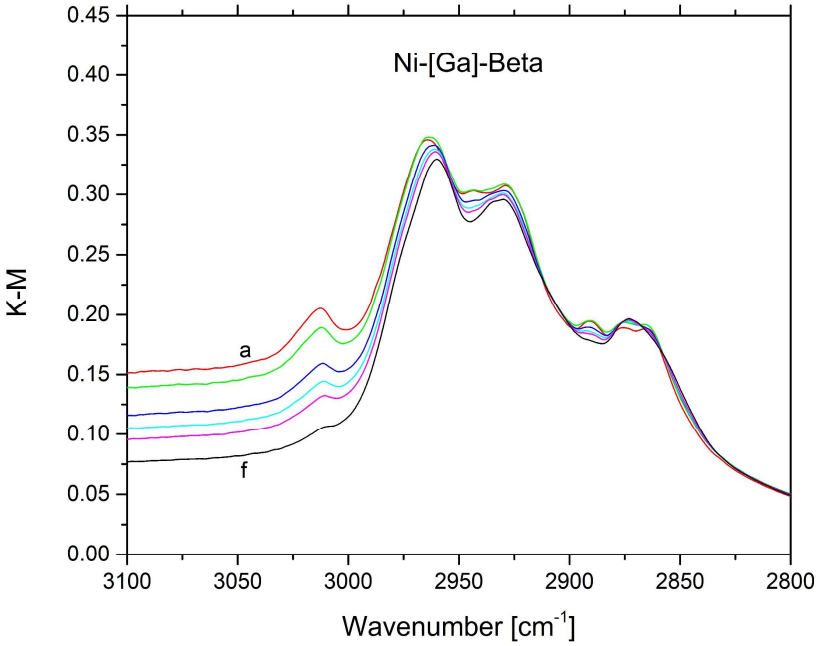

Figure S2.1. C_2H_4 adsorption onto oxidized Ni-[Ga]-Beta catalyst. C_2H_4 was pulsed into drifts cell and purged from a to f. Spectra show butene bands desorb over time.

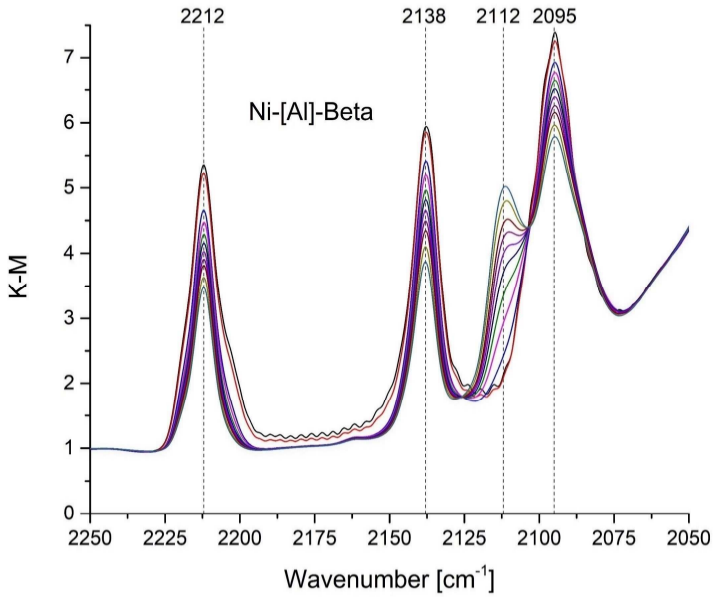

Figure S2.2. CO adsorption at 30°C after reduction with CO at 300°C onto Ni-[Al]-Beta, spectra after CO pulse a-f.

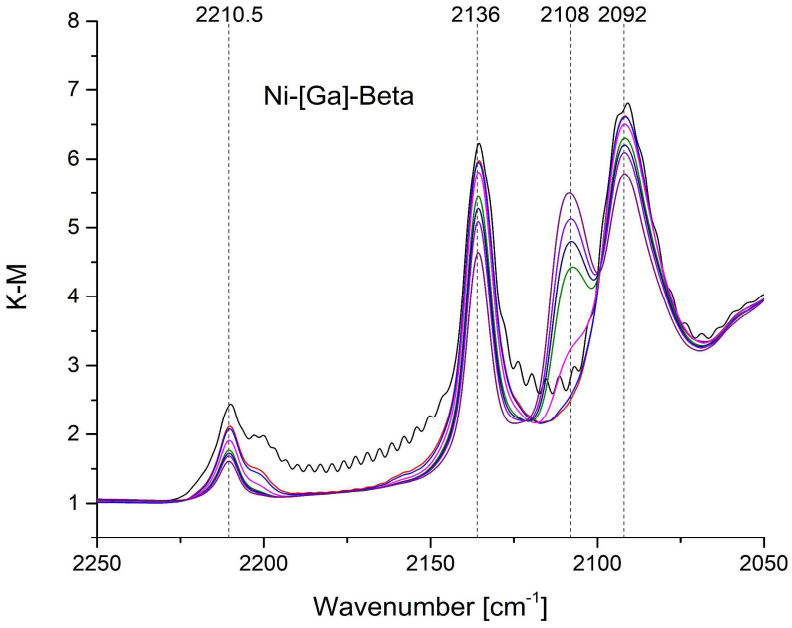

Figure S2.3. CO adsorption at 30°C after reduction with CO at 300°C onto Ni-[Ga]-Beta, spectra after CO pulse a-f.

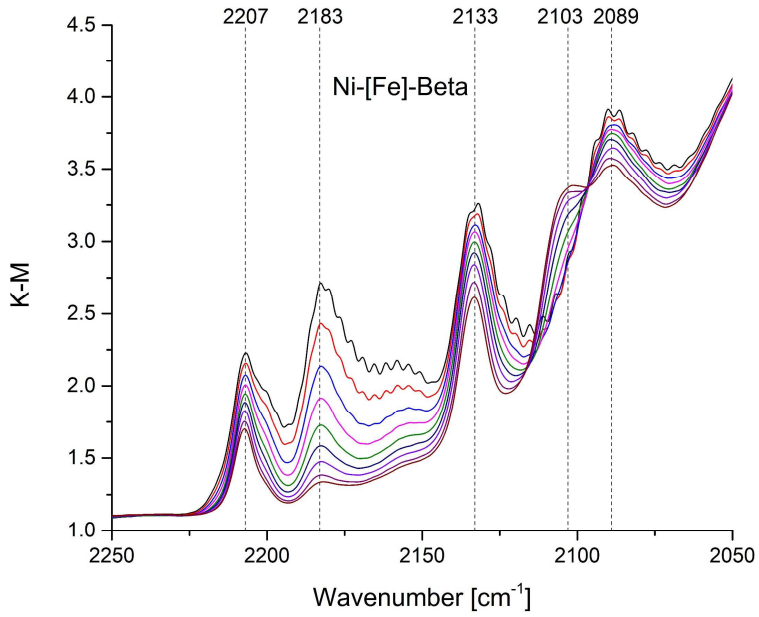

Figure S2.4. CO adsorption at 30°C after reduction with CO at 300°C onto Ni-[Fe]-Beta, spectra after CO pulse a-f. Bands at 2207, 2133, 2103, 2089 cm^{-1} correspond to Ni carbonyls while the band at 2183 cm^{-1} corresponds to extraframework Fe^{2+} carbonyl.

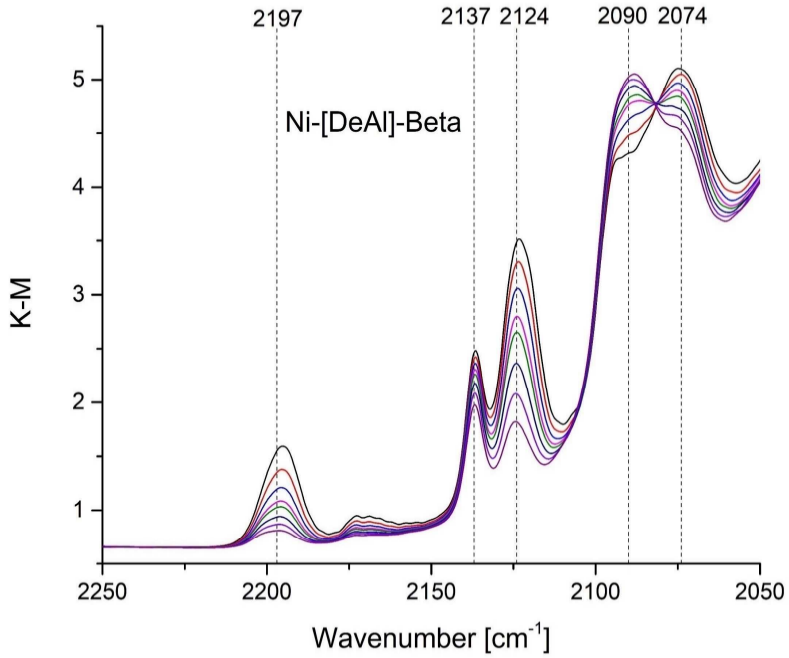

Figure S2.5. CO adsorption at 30°C after reduction with CO at 300°C onto Ni-[DeAl]-Beta, spectra after CO pulse a-f.

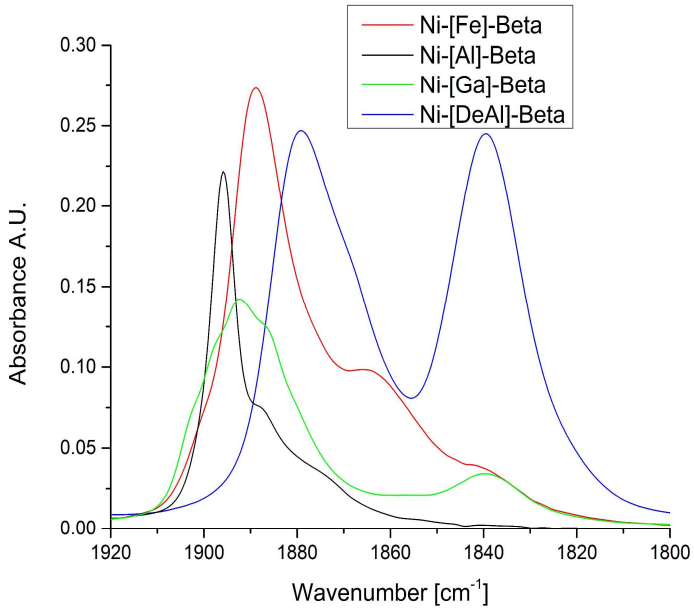

Figure S2.6. NO adsorption at room temperature onto oxidized Ni-[X]-Beta, where X= Al, Ga, Fe, or DeAl.

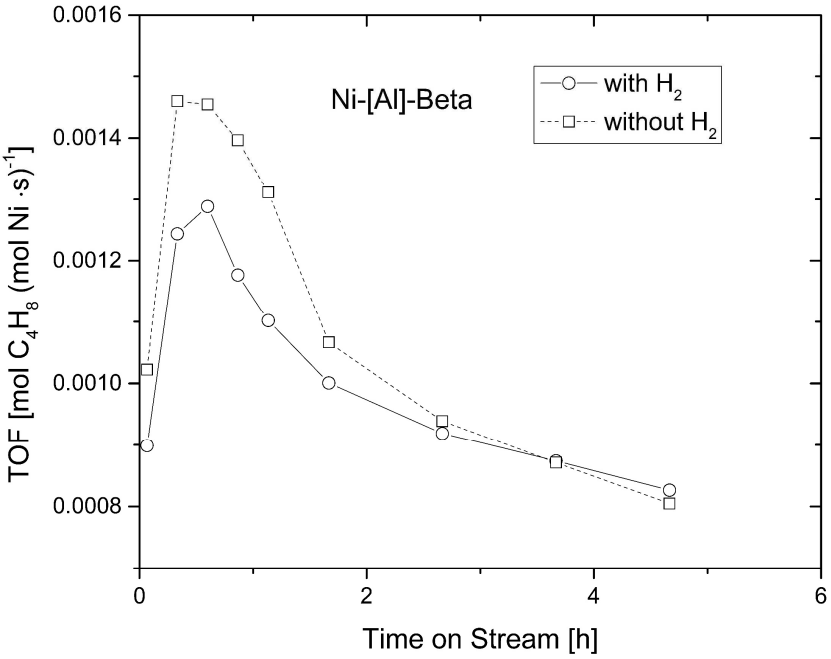

Figure S2.7. TOF of Ni-[Al]-Beta with and without H_2. The addition of H_2 reduces of the TOF but decrease the rate of deactivation.

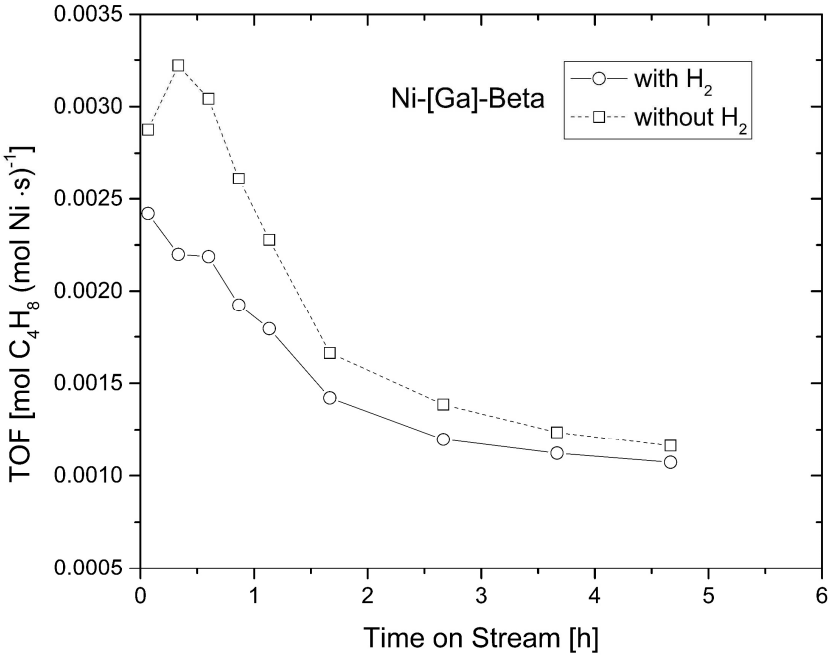

Figure S2.8. TOF of Ni-[Ga]-Beta with and without H_2. The induction period is not observed in the presence of H_2. The TOF decreases in the presence of H_2.

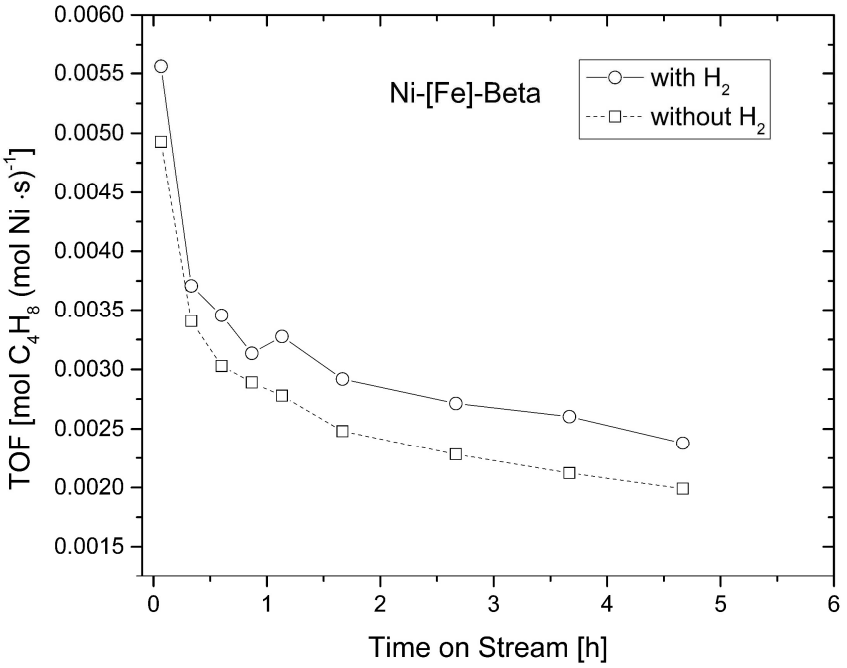

Figure S2.9. TOF of Ni-[Fe]-Beta with and without H_2. The activity is increased in the presence of H_2, the rate of deactivation is not significantly altered.

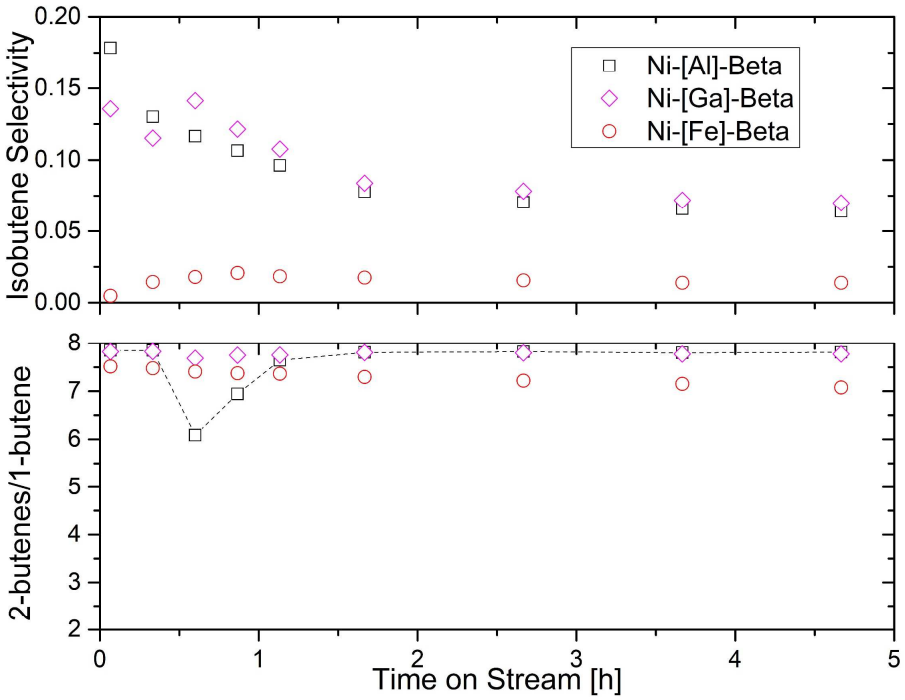

Figure S2.10. Top: Selectivity of isobutene relative to total butene formation. Bottom: ratio of total 2-butene formation to 1-butene. Results for dimerization carried out in the presence of H_2.

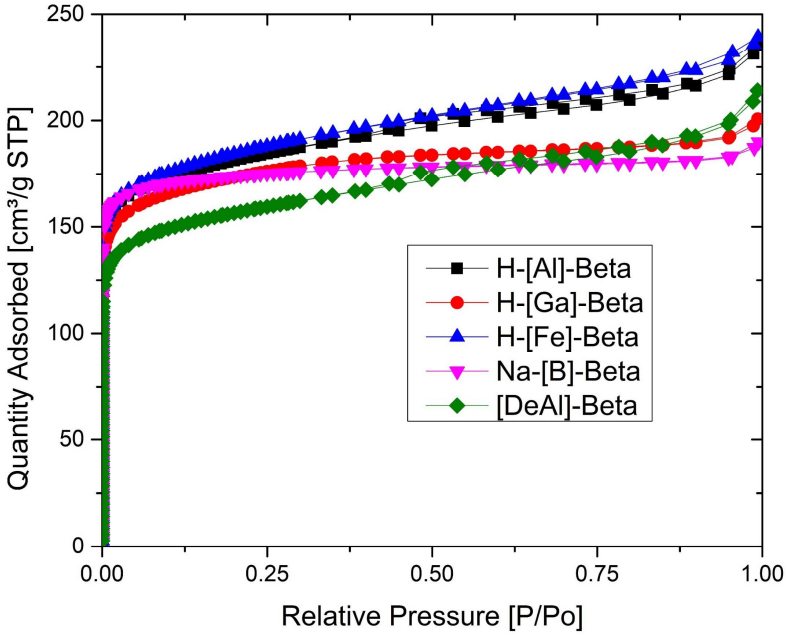

Figure S2.11. N_2 physisorption isotherms for supports without dispersed Ni.

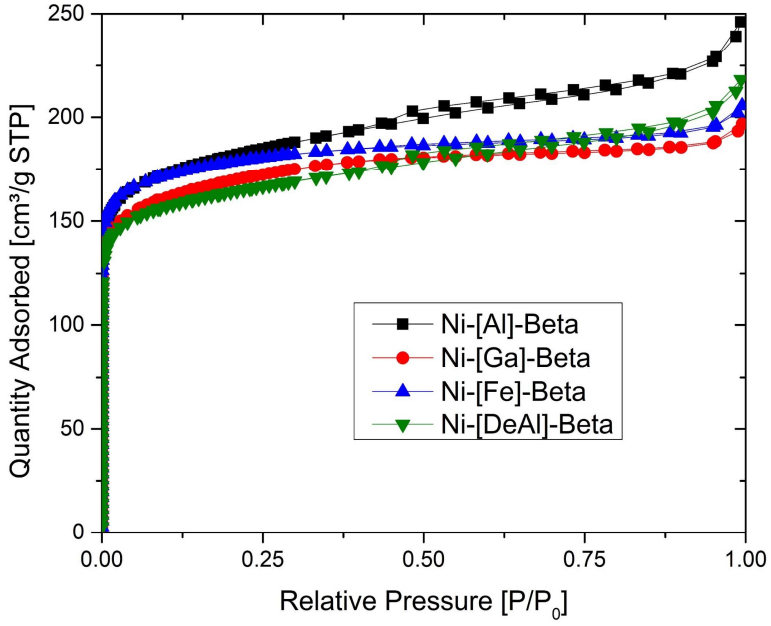

Figure S2.12. N_2 physisorption isotherms for catalysts with dispersed Ni

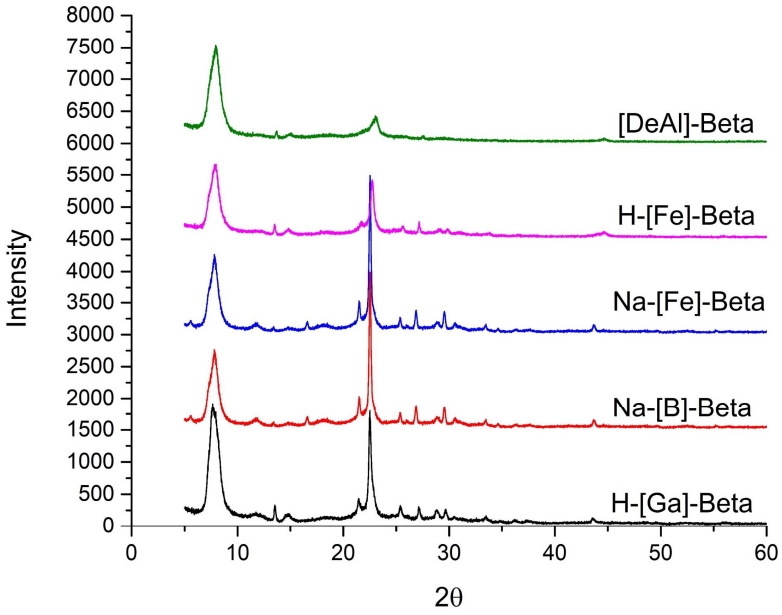

Figure S2.13. Powder XRD spectra for Beta supports without dispersed Ni

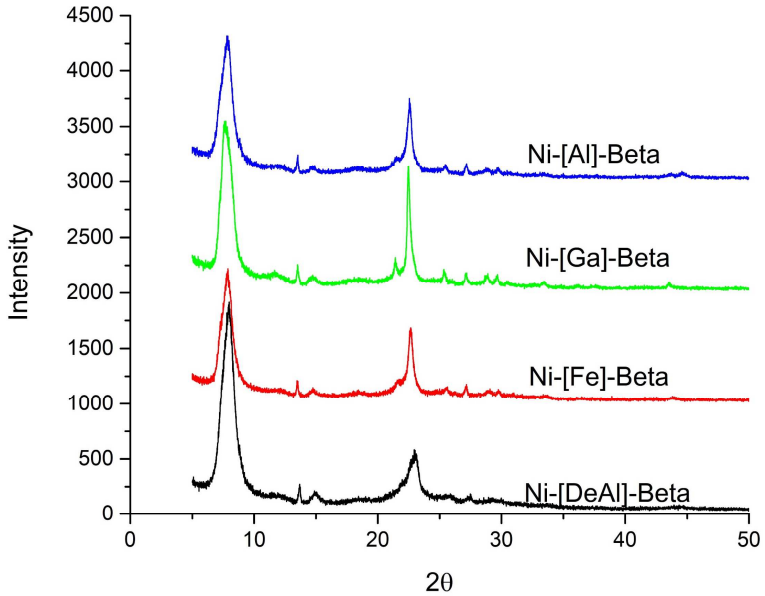

Figure S2.14. Powder XRD spectra for Beta catalysts with dispersed Ni

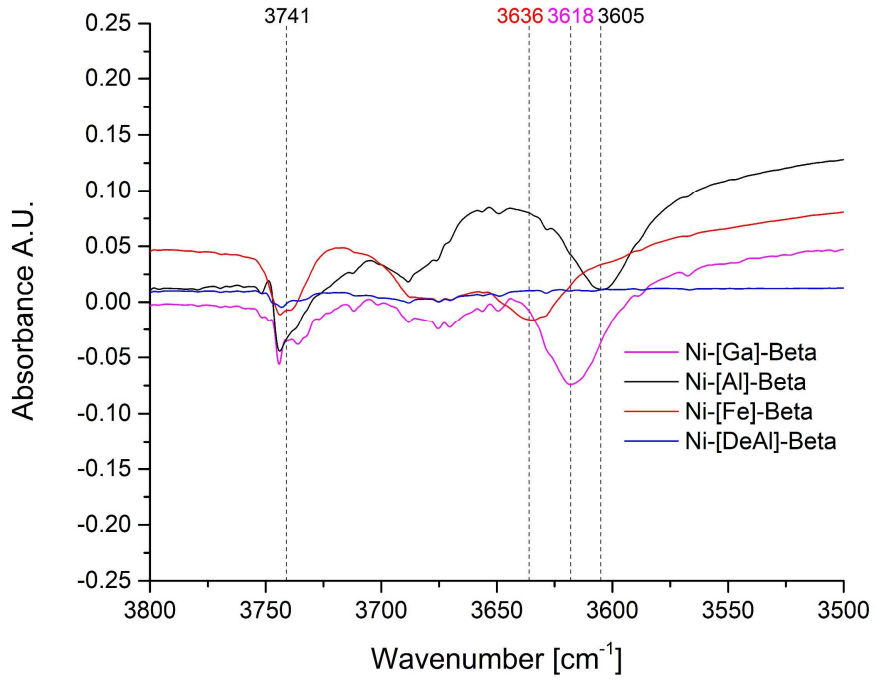

Figure S2.15. FTIR spectra of the OH region of catalysts after C_2H_4 adsorption (CH region shown in Figure 1. Spectra show a decrease in the isolated silanol band (3741 cm^{-1}) as well as acidic silanol bands (3605, 3618, and 3636 cm^{-1} respectively) for Ni-[Al]-,-[Ga]-, and -[Fe]-Beta catalysts

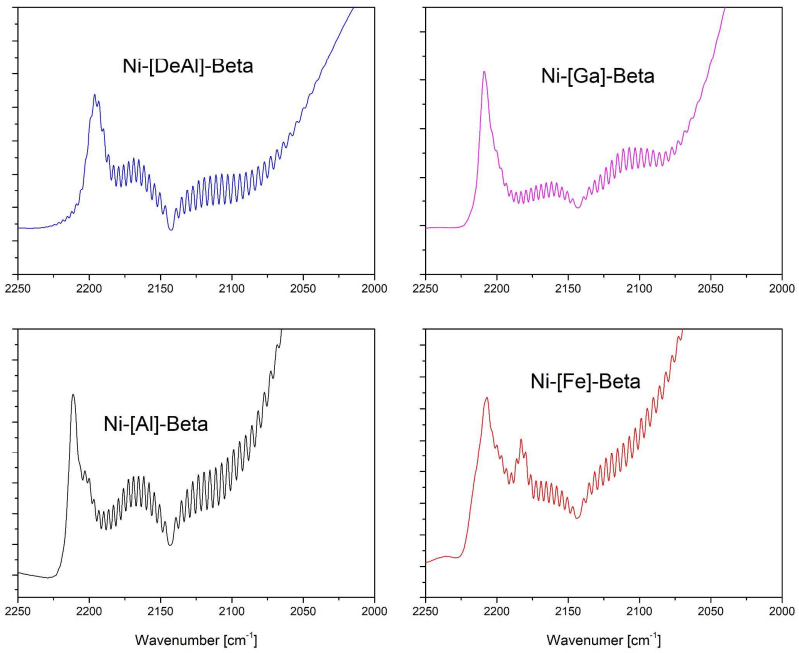

Figure S2.16. FTIR spectra of CO adsorption of catalysts after oxidative treatment to remove $Ni(acac)_2$ ligands. Spectra show Ni^{2+} (2197, 2209, 2212, and 2206 cm^{-1}) in all catalysts as well as Fe^{2+} (2183 cm^{-1}) in the Ni-[Fe]-Beta catalyst (band assignments seen in Table 2).

Chapter 3

Effect of altering zeolite support composition on supported Ni cations: reducibility and ethylene dimerization activity

Manuscript in preparation

Michael Meloni[1], and Ron C. Runnebaum[1,2,*]
[1]Department of Chemical Engineering, University of California, Davis, CA, 95616, USA
[2]Department of Viticulture & Enology, University of California, Davis, CA, 95616, USA

3.1 Abstract

The reducibility and C_2H_4 dimerization activity of zeolite Beta supported Ni cations was examined using Ni-[Al]-Beta and Ni-[Fe]-Beta, where Al or Fe are heteroatoms present in the zeolite framework. The Ni cations present in Ni-[Al]-Beta were more reducible by CO, as indicated by the appearance of Ni^+ carbonyl bands at lower (ca. 80°C) temperature than Ni-[Fe]-Beta (ca. 220°C). Co-feeding H_2 at 16 kPa increased the dimerization activity by 1.4-fold, while butene selectivity decreased to 0.91. When the partial pressure of H_2 increased to 32 kPa the butene selectivity continuously decreased from 0.75 to 0.59. The activation energy for Ni-[Al]-Beta and Ni-[Fe]-Beta was determined to be 48.8 and 32.4 kJ/mol respectively, showing that Ni-[Fe]-Beta is more effectively stabilizing the TOF determining transition state. The Ni sites of ion exchanged [Fe]-Beta are more uniform, as indicated by smaller full width half max (FWHM) of the Ni^{2+} monocarbonyl band compared to the anhydrously prepared sample. Dispersing Ni by ion exchange instead of anhydrous deposition onto Ni-[Fe]-Beta results in 1.4-fold higher dimerization activity per Ni atom but no change in activation energy.

3.2 Introduction

Supported metal catalysts are used in a variety of industries including chemical synthesis, environmental chemistry, and pharmaceuticals.[1,2] One of the most consequential but difficult to study aspects of supported metal catalysts is determining how the support-metal interactions affect the properties of a supported metal catalysts.[3,4] Particle size can be difficult to control between supports, and larger particles are influenced less by the support interactions. Atomically dispersed metals present, therefore, an opportunity to systematically study how the support functions as ligands bonded to a metal center.[5–7] Crystalline supports such as zeolites can be used as a uniform support upon which metals can be dispersed.[5] These metals occupy extraframework cation sites that can be repeatably synthesized. The use of zeolite heteroatom composition can enable chemical changes in the support while keeping crystallographic structure of the zeolite the isomorphically identical.[8] The extraframework cation sites are the same within a zeolite framework,[9] which enables the comparison of how elemental composition of the support (i.e. as ligands) affects supported-

metal properties such as electron density and reactivity. Zeolite Beta (BEA framework) is unique because it can be synthesized with a variety of framework elemental compositions.[8,10] Cationic Ni supported on a solid material is of interest for C_2H_4 dimerization as it has the potential to replace organometallic catalysts.[11] In this study support-metal interactions are studied using Ni dispersed onto Al and Fe containing Beta zeolites. The differences between reducibility of Ni cations as well as C_2H_4 dimerization activation energy are characterized through catalysis and temperature programmed reduction.

3.3 Experimental Methods

Catalyst Synthesis. [Fe]-Beta was synthesized using a procedure from Raj et al.[12,13] Typically 0.0775g of NaOH and 0.0575g of KOH were added to 10.6g of 35% TEAOH. 3.00g of fumed SiO_2 was added to the solution and stirred for 4 h. A solution of 0.306g ferric sulfate (ACROS Organics) dissolved in 3.68g of H_2O was slowly added to the previous solution over 30 minutes. The solution ($10SiO_2$: 5.0TEAOH: $0.25Fe_2O_3$: 0.39NaOH: 0.21KOH: $117H_2O$) was then transferred to a 23mL Teflon liner in a Parr autoclave vessel, hydrothermal synthesis took place statically at 140°C for 15 days. The resulting white zeolite was washed with H_2O then calcined in 10% O_2 with a ramp of 2°C/min with a 1 h hold at 120°C and 330°C, then ramped at 1°C/min until 500°C and held for 6 h. Zeolites were converted to NH_4-[X]-Beta via ion exchange by two consecutive exchanges mixing the zeolite with 1M NH_4NO_3 for 24 h at room temperature. NH_4-[Al]-Beta zeolite with Si/Al=19 (NH_4-[Al]-Beta) was purchased from Zeolyst (CP814C). Ni was dispersed onto H-[Fe]-Beta and H-[Al]-Beta via anhydrous deposition with $Ni(acac)_2$ (acac = acetylacetonate) mixed with the specific zeolite in n-pentane. All work was done in a glovebox or Schlenk line to exclude moisture and O_2. Ni was also dispersed via Ni ion exchange by stirring Na-[Fe]-Beta in 20 mM $Ni(NO_3)_2$ at 75°C for 24 h. The solution was then cooled, rinsed with DI water, and dried before calcination by using the previously described procedure for Na-[Fe]-Beta. Ni and Al or Fe content of samples, ratios reported in Table 3.1, were determined via ICP MS at UC Davis Interdisciplinary Center for Inductively-Coupled Mass Spectrometry (ICP-MS).

Fourier Transform Infrared Spectroscopy. Powdered samples, stored in a glovebox, were loaded into a Pike diffuse reflectance cell. Fourier Transform Infrared Spectrometry (FTIR) data were taken by a Bruker Tensor II with 2 cm^{-1} resolution and 128 scans collected per spectrum. For CO temperature programmed reduction, samples were heated in 10% CO from room temperature to 300°C at a rate of 5°C/min with spectra collected every 20°C.

Catalysis. Catalysts were loaded in a glovebox into a 6.35 mm OD quartz tube, diluted with ca. 100 mg α-Al_2O_3, and held in place with quartz wool. The tube was transferred without exposure to air into a 3-zone heated furnace. Before catalysis samples were heated at 1°C/min to 500°C in 10% O_2 (zero air, Praxair) and held for 4 h, then cooled to the reaction temperature. The reaction products were measured with gas chromatography (GC) using a flame ionization detector (FID). Conversion was calculated by using a carbon balance on all the products and reactants. All catalysts were operating at C_2H_4 conversions of less than 10%. Turnover frequency (TOF) was determined by normalizing the reaction rate to the amount of Ni dispersed as determined by ICP-MS. Catalysts were regenerated between runs by the same procedure of heating 1°C/min to 500°C in 10% O_2 for 4 h. After regeneration, the reactor was purged with N_2 (99.999%, Praxair) for 30 min before starting reactant flow at the desired temperature.

Thermogravimetric Analysis. Thermogravimetric analysis experiments (TGA), with an online mass spectrometer (MS), were performed with Netsch Jupiter F209. Samples were loaded into an alumina crucible and weighed by the TGA. The SDA removal via calcinated was done by heating Na-[Fe]-Beta, washed zeolite from the initial hydrothermal synthesis, in 10% O_2 at a ramp rate of 5°C/min to 500°C for 6 h. The experiment files were corrected by running the temperature program with an empty crucible. The m/z monitored by MS were 18, 32, and 44 for H_2O, O_2, and CO_2 respectively.

3.4 Results and Discussion

C_2H_4 Dimerization Catalysis

The activation energy for Ni-[Al]-Beta and Ni-[Fe]-Beta were determine between 160 – 200°C, Figure 3. 1, to be 48.8, 32.4, and 32.3 kJ/mol for Ni-[Al]-Beta, Ni-[Fe]-Beta (anhydrous), and Ni-[Fe]-Beta (ion exchanged) respectively. Activation energies reported here and for other Ni based heterogenous catalysts are summarized in Table S3.2. Both Ni-[Al]-Beta and Ni-[Fe]-Beta have been shown to catalyze C_2H_4 dimerization by the Cossee-Arlman mechanism.[14,15] The activation energies determined show that Ni-[Fe]-Beta is significantly more effective at stabilizing the TOF-determining transition state involved in the formation of [Ni-butene-H]$^+$.[16] The activation energy of 48.8 kJ/mol, Figure 3.1 and Table S3.2, determined using Ni-[Al]-Beta is consistent with other measurements.[17,18] The activation energy of Ni-[Fe]-Beta prepared via ion exchange and anhydrous deposition are the same (32.3 and 32.4 kJ/mol respectively), showing that there is no difference between the active Ni sites stabilizing the TOF determining transition state between the two preparation methods.

Table 3.1. Elemental ratios determined by ICP-MS, X = Al or Fe for Ni-[Al]-Beta and Ni-[Fe]-Beta respectively. TOF [units: mol C_4H_8 (mol Ni s)$^{-1}$] taken from catalyst at 3 h on stream at 160°C, 8.7 kPa C_2H_4. Activation energies determined between 160 – 200°C.

Catalyst	Si/X	Ni/X	TOF x10^{-3}	Ea [kJ/mol]
Ni-[Al]-Beta	19	0.42	2.32	48.8
Ni-[Fe]-Beta Anhydrous	11	0.26	4.17	32.4
Ni-[Fe]-Beta Ion Exchange	8	0.12	5.77	32.3

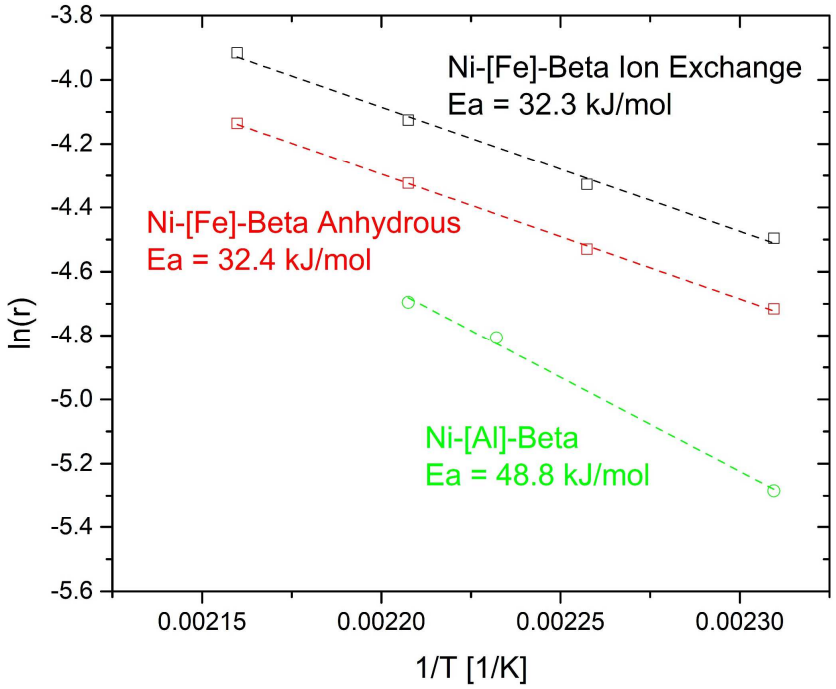

Figure 3.1. Arrhenius plot of Ni-[Fe]-Beta anhydrous, (red), Ni-[Fe]-Beta ion exchanged (black) and Ni-[Al]-Beta (green). Dimerization was carried out at 8.7 kPa C_2H_4, balance N_2. Activation energies were measured to be 32.4 and 48.8 kJ/mol for Ni-[Fe]-Beta and Ni-[Al]-Beta respectively.

However, the TOF between the different preparation methods was different at $4.17x10^{-3}$ and $5.77x10^{-3}$ [mol C_4H_8 (mol Ni s)$^{-1}$], Table 3.1, for the anhydrous and ion exchanged sample respectively. The 1.4-fold higher activity (Figure 3.2, and Figure S3.1) per mol of dispersed Ni shows that the Ni is being more effectively utilized for dimerization by dispersing using ion exchange compared to the anhydrous deposition. Because the active sites appear to be equivalent, based on activation energy measurements, in catalyzing C_2H_4 dimerization based on measuring the same activation energy, the ion exchange dispersion method appears to be more effective at dispersing active Ni sites. Divalent cations dispersed via ion exchanges will preferentially site at extraframework sites with two proximal framework heteroatoms, which is the proposed active Ni site.[9,16,19,20] Because the ion exchange is more effective at dispersing active Ni site, the active Ni sites are likely extraframework Ni cations that are associated with paired framework Fe sites. The anhydrous deposition is less specific in how the Ni is deposited, which may result in Ni dispersed in other locations that are not active for dimerization.

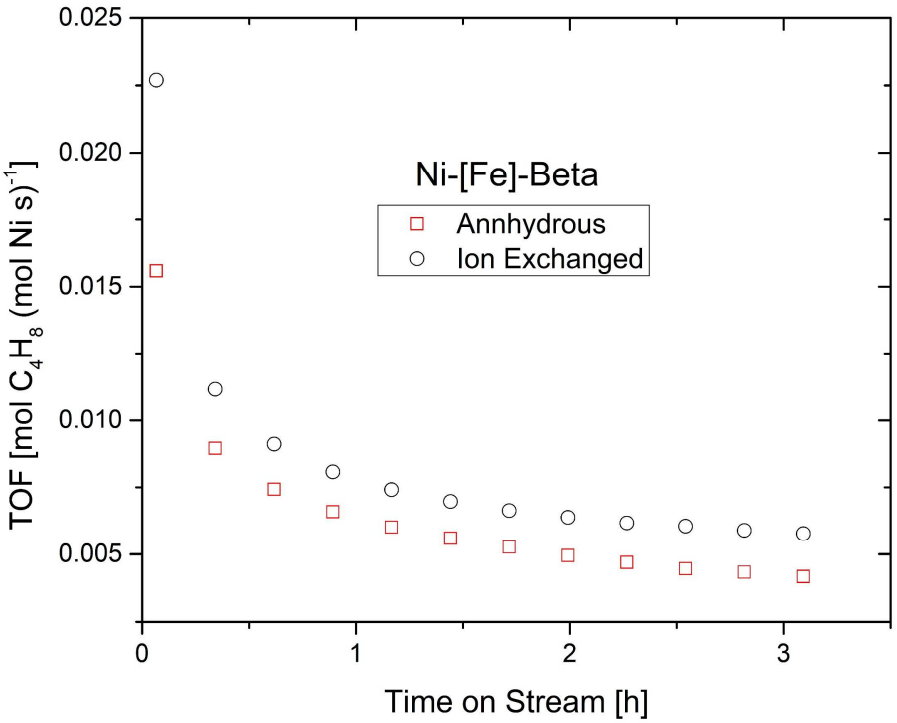

Figure 3.2. The effect of preparation method on activity of Ni-[Fe]-Beta catalysts. The TOF of the catalyst prepared via ion exchange, with $Ni(NO_3)_2$, is approximately 1.3–1.4 more active than the catalyst prepared via anhydrous deposition of $Ni(acac)_2$.

The effect of H_2 partial pressure, shown in Figure 3.3, was looked at by varying H_2 partial pressure during C_2H_4 dimerization at 180°C with Ni-[Fe]-Beta. The ratio of C_2H_4:H_2 was varied from 1:2 to 1:4 corresponding to H_2 partial pressure of 16 kPa and 32 kPa respectively. At 16 kPa and 32 kPa H_2 the butene selectivity decreased to 0.90 and 0.75 respectively. During catalysis at 32 kPa H_2 the selectivity continuously decreased from 0.75 to 0.59. After catalysis at 32 kPa H_2, H_2 was removed, and the selectivity increased back to 0.96. The ethane formation rate, Figure 3.3B, increased from 2.19×10^{-4} to 3.71×10^{-3} [C_2H_6 (mol Ni s)$^{-1}$] corresponding to a 17-fold increase in C_2H_6 TOF after increasing the partial pressure of H_2 to 32 kPa. The increase in ethane TOF suggests that when the partial pressure of H_2 is sufficiently high some Ni sites are being activated for C_2H_4 hydrogenation.

The TOF for butene formation increases with each additional increase in H_2 partial pressure and then returns to a lower TOF after the removal of H_2 from the feed. The results show that H_2 actively increase the activity of the Ni-[Fe]-Beta catalyst and that benefit disappears when H_2 is not co-fed. This behavior is consistent

with co-fed H_2 activating certain Ni sites that otherwise are not active without H_2. These sites need H_2 present to be activated as evidenced by when H_2 is removed from the feed the activity decreases immediately. If H_2 was only needed to activate the site once, then it would be expected for the activity to remain higher after H_2 is removed from the feed. Since the rate of deactivation with respect to butene formation does not appear to significantly increase with the addition of H_2, it is likely that the Ni sites performing hydrogenation are different than the ones active for dimerization but require a sufficient partial pressure of H_2 to be active.

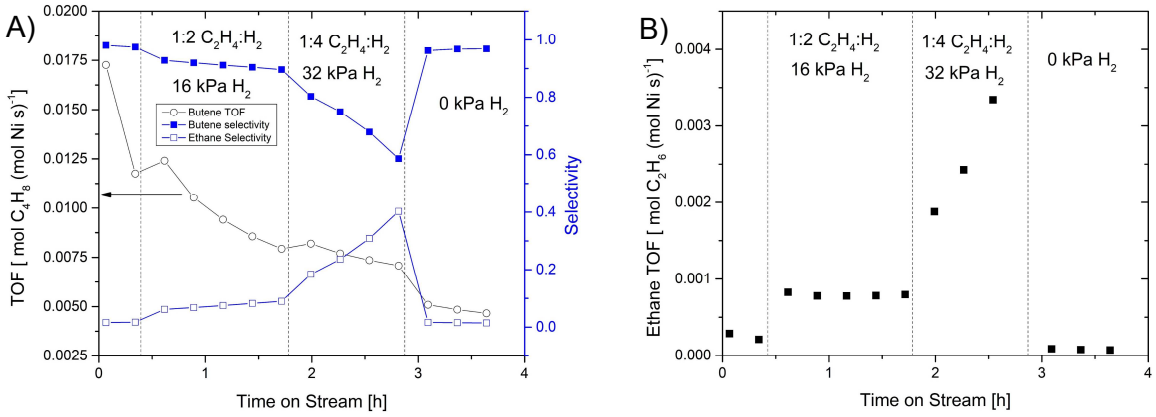

Figure 3.3. A) The influence of H_2 partial pressure on C_2H_4 dimerization with Ni-[Fe]-Beta (anhydrous). Dimerization rate increases with increasing partial pressure of H_2. When increasing to 32 kPa butene selectivity decreases at an increasing rate. B) The influence of H_2 partial pressure on C_2H_6 formation rate with Ni-[Fe]-Beta (anhydrous). When H_2 partial pressure is increased to 32 kPa the TOF for C_2H_6 TOF to more rapidly increase.

CO Temperature Programmed Reduction

Temperature programmed reduction (TPR) was performed with Ni-[Al]-Beta and Ni-[Fe]-Beta by heating each catalyst in 10% CO at a ramp rate of 5°C/min. The reduction in the presence of CO was monitored *in-situ* with FTIR by tracking the Ni carbonyl bands (previously determined band assignments reported in Table S3.1). Figures 3.4A-C show spectra under CO flow between 40 – 120°C, 140 – 220°C, and 240 – 300°C respectively. While heating from 40 – 120°C, the Ni^{2+}-CO (2212, 2207 cm^{-1} for Ni-[Al]-Beta and Ni-[Fe]-Beta respectively) [15,21] band decreases for both samples. The Ni^{+}-$(CO)_2$ (2138 and 2095 cm^{-1}) bands

are not present initially but begin to appear when Ni-[Al]-Beta has been heated to 80°C. This indicates that the reduction of N^{2+} to Ni^{+} is occurring because the Ni^{2+} sites need to be reduced for N^{+}-$(CO)_2$ bands to appear. The Ni^{+}-CO (2112 cm^{-1}) band appears at 180°C and relatively quickly increases in intensity until 300°C. The increase in intensity of the Ni^{+}-CO band instead of both Ni^{+}-$(CO)_2$ bands indicates that at elevated temperature the Ni^{+} monocarbonyl is more stable than dicarbonyls on some Ni sites. In contrast to Ni-[Al]-Beta, the Ni^{+}-CO (2103 cm^{-1}) band on Ni-[Fe]-Beta does not appear until 220°C and grows in intensity as the sample is heated to 300°C. The significantly higher onset temperature of when Ni^{+} carbonyl bands appear on Ni-[Fe]-Beta compared to Ni-[Al]-Beta, 220°C compared to 80°C, suggests that the Ni sites on Ni-[Fe]-Beta are more resistant to reduction. Figure S3.2 shows how the relative peak heigh of the Ni+ monocarbonyl increases for both Ni-[Al]-Beta and Ni-[Fe]-Beta. The peak height of the monocarbonyl on Ni-[Al]-Beta is at 53 % of the 300°C peak height at 220°C compared to 10 % for Ni-[Fe]-Beta. This shows that the Ni sites are more easily reduced by CO on Ni-[Al]-Beta compared to Ni-[Fe]-Beta. Ni^{+} dicarbonyls do not appear during the reduction of Ni-[Fe]-Beta, suggesting the Ni^{+} dicarbonyls are less thermally stable on Ni-[Fe]-Beta compared to Ni-[Al]-Beta.

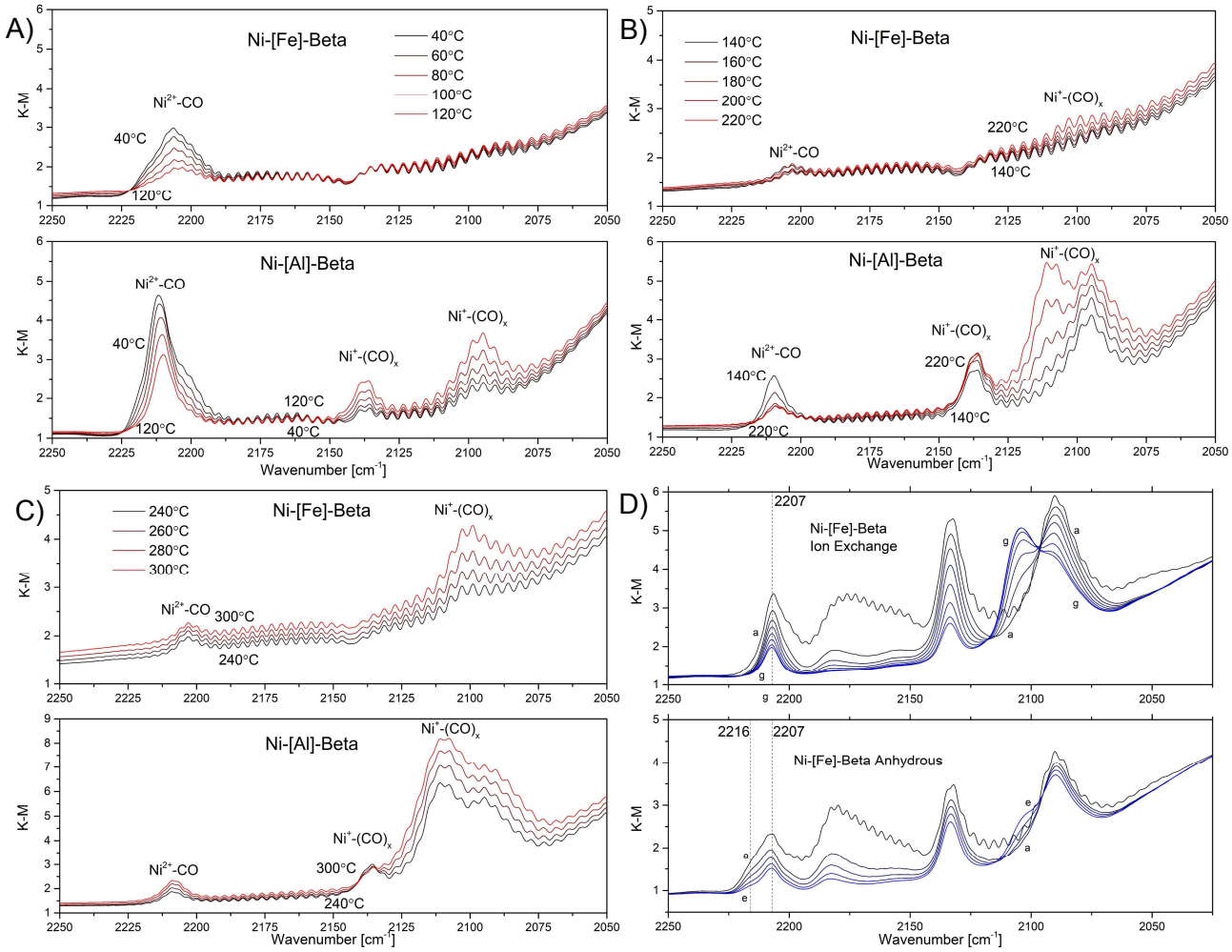

Figure 3.4. A-C: Temperature programmed reduction between 40 – 300°C of Ni-[Al]-Beta and Ni-[Fe]-Beta in 10% H_2 ramping at 10°C/min. A) Ni-[Fe]-Beta Ni^{2+}-CO bands decrease but see no start to the formation of Ni^{+}-CO. Ni-[Al]-Beta Ni^{2+}-CO band decreases while the Ni^{+}-CO band start to increase around 100°C. B) $Ni^{+}(CO)$ bands on Ni-[Al]-Beta increase with increasing temperature. Ni carbonyl bands on Ni-[Fe]-Beta do not change significantly between 140 – 220°C. C) Ni^{+}-$(CO)_x$ bands increase with increasing temperature for Ni-[Fe]-Beta. The Ni^{+}-$(CO)_x$ bands continue to increase with Ni-[Al]-Beta. D) CO adsorption at room temperature, after reduction at 300°C in 10% CO for 15 min, onto Ni-[Fe]-Beta prepared via ion exchange and anhydrous deposition with $Ni(acac)_2$. The shoulder present in the Ni^{2+}-CO band in the anhydrous sample is not present when prepared with ion exchange.

CO adsorption was also performed with Ni-[Fe]-Beta prepared via anhydrous deposition of $Ni(acac)_2$ as well as an ion exchanged sample using $Ni(NO_3)_2$. Figure 3.4D shows the CO adsorption/desorption onto both samples at room temperature. The Ni^{2+}-CO band on the sample prepared with $Ni(acac)_2$ has a shoulder at approximately 2216 cm^{-1}, while the ion exchanged sample does not show this band. The uniformity of

the Ni sites can be compared between the samples by observing the Ni^{2+}-CO band.[22] The full-width half max (FWHM) is 9.1 and 12 for the ion-exchanged and anhydrous sample respectively. This band has a shoulder at approximately 2216 cm^{-1} on the sample prepared with $Ni(acac)_2$ suggests there are two distinct Ni sites. The difference in site distribution can be rationalized by considering the differences in Ni deposition method. The anhydrous deposition of $Ni(acac)_2$ forces approximately 1 wt% Ni (Ni/Fe = 0.26, Table 3.1) to be dispersed onto the [Fe]-Beta zeolite by evacuating the n-pentane solvent. In contrast the Ni dispersed by an ion exchange needs to be stabilized by two framework Fe sites. The solution is then washed before calcination that leads to the removal of excess Ni, which likely leads to more uniform Ni sites and less Ni (Ni/Fe = 0.12, Table 3.1) dispersed onto the zeolite.

3.5 Conclusions

The effect that zeolite Beta support composition has on the properties of a supported Ni cation were studied by TPR and C_2H_4 dimerization catalysis. The reducibility of the Ni cations was shown to be influenced by the elemental composition of the zeolite Beta support. This was shown through CO TPR, which indicates that the Ni cations in Ni-[Fe]-Beta were more resistant to reduction. The effect of H_2 partial pressure was studied with Ni-[Fe]-Beta between 8.7 – 32 kPa. It was found that butene formation increased with increasing partial pressure with minor decrease in butene selectivity until 32 kPa H_2. At the 32 kPa H_2, the selectivity towards ethane increased continuously over 1 h, likely due to some Ni sites becoming active for hydrogenation at the higher H_2 partial pressure. The activation energy measured with Ni-[Al]-Beta and Ni-[Fe]-Beta were 48.8 and 32.4 kJ/mol respectively, indicating that Ni-[Fe]-Beta was more effective at stabilizing the TOF determining transition state. Dispersal of active Ni sites was shown to be more effective by ion-exchange than anhydrous deposition. The activity per amount of dispersed Ni on Ni-[Fe]-Beta prepared via ion-exchange was 1.4-fold higher than Ni-[Fe]-Beta prepared by anhydrous deposition, while the activation energy was the same between the two catalysts.

3.6 References

(1) Zhang, L.; Zhou, M.; Wang, A.; Zhang, T. Selective Hydrogenation over Supported Metal Catalysts: From Nanoparticles to Single Atoms. *Chem. Rev.* **2020**, *120* (2), 683–733. https://doi.org/10.1021/acs.chemrev.9b00230.

(2) Guan, B.; Zhan, R.; Lin, H.; Huang, Z. Review of State of the Art Technologies of Selective Catalytic Reduction of NOx from Diesel Engine Exhaust. *Appl. Therm. Eng.* **2014**, *66* (1–2), 395–414. https://doi.org/10.1016/j.applthermaleng.2014.02.021.

(3) Flytzani-Stephanopoulos, M.; Gates, B. C. Atomically Dispersed Supported Metal Catalysts. *Annu. Rev. Chem. Biomol. Eng.* **2012**, *3* (1), 545–574. https://doi.org/10.1146/annurev-chembioeng-062011-080939.

(4) Lu, J.; Serna, P.; Gates, B. C. Zeolite- and MgO-Supported Molecular Iridium Complexes: Support and Ligand Effects in Catalysis of Ethene Hydrogenation and H-D Exchange in the Conversion of H2+ D2. *ACS Catal.* **2011**, *1* (11), 1549–1561. https://doi.org/10.1021/cs200397r.

(5) Babucci, M.; Guntida, A.; Gates, B. C. Atomically Dispersed Metals on Well-Defined Supports Including Zeolites and Metal-Organic Frameworks: Structure, Bonding, Reactivity, and Catalysis. *Chemical Reviews*. 2020, pp 11956–11985. https://doi.org/10.1021/acs.chemrev.0c00864.

(6) White, R. J.; Luque, R.; Budarin, V. L.; Clark, J. H.; Macquarrie, D. J. Supported Metal Nanoparticles on Porous Materials. Methods and Applications. *Chem. Soc. Rev.* **2009**, *38* (2), 481–494. https://doi.org/10.1039/b802654h.

(7) Ndolomingo, M. J.; Bingwa, N.; Meijboom, R. Review of Supported Metal Nanoparticles: Synthesis Methodologies, Advantages and Application as Catalysts. *J. Mater. Sci.* **2020**, *55* (15), 6195–6241. https://doi.org/10.1007/s10853-020-04415-x.

(8) Aiello, R.; Nagy, J. B.; Giordano, G.; Katovic, A.; Testa, F. Isomorphous Substitution in Zeolites. *Comptes Rendus Chim.* **2005**, *8* (3–4), 321–329. https://doi.org/10.1016/j.crci.2005.01.014.

(9) Dědeček, J.; Čapek, L.; Kaucký, D.; Sobalík, Z.; Wichterlová, B. Siting and Distribution of the Co Ions in Beta Zeolite: A UV-Vis-NIR and FTIR Study. *J. Catal.* **2002**, *211* (1), 198–207. https://doi.org/10.1016/S0021-9517(02)93697-3.

(10) Patet, R. E.; Koehle, M.; Lobo, R. F.; Caratzoulas, S.; Vlachos, D. G. General Acid-Type Catalysis in the Dehydrative Aromatization of Furans to Aromatics in H-[Al]-BEA, H-[Fe]-BEA, H-[Ga]-BEA, and H-[B]-BEA Zeolites. *J. Phys. Chem. C* **2017**, *121* (25), 13666–13679. https://doi.org/10.1021/acs.jpcc.7b02344.

(11) Finiels, A.; Fajula, F.; Hulea, V. Nickel-Based Solid Catalysts for Ethylene Oligomerization-a Review. *Catal. Sci. Technol.* **2014**, *4* (8), 2412–2426. https://doi.org/10.1039/c4cy00305e.

(12) Anuj Raj, S. S. and K. L. Studies on the Stability of Fe3+ Ions in the Ferrisilicate Analog of Zeolite Beta. *J. Catal.* **1994**, *147*, 207–213.

(13) Yun, J. H.; Lobo, R. F. Catalytic Dehydrogenation of Propane over Iron-Silicate Zeolites. *J. Catal.* **2014**, *312*, 263–270. https://doi.org/10.1016/j.jcat.2014.02.007.

(14) Joshi, R.; Zhang, G.; Miller, J. T.; Gounder, R. Evidence for the Coordination-Insertion Mechanism of Ethene Dimerization at Nickel Cations Exchanged onto Beta Molecular Sieves. *ACS Catal.* **2018**, 11407–11422. https://doi.org/10.1021/acscatal.8b03202.

(15) Meloni, M.; Runnebaum, R. C. Tuning Supported Ni Catalysts by Varying Zeolite Beta Heteroatom Composition: Effects on Ethylene Adsorption and Dimerization Catalysis. *Catal. Sci. Technol.* **2021**, *11* (10), 3393–3401. https://doi.org/10.1039/d1cy00308a.

(16) Brogaard, R. Y.; Olsbye, U. Ethene Oligomerization in Ni-Containing Zeolites: Theoretical Discrimination of Reaction Mechanisms. *ACS Catal.* **2016**, *6* (2), 1205–1214. https://doi.org/10.1021/acscatal.5b01957.

(17) Li, Z.; Schweitzer, N. M.; League, A. B.; Bernales, V.; Peters, A. W.; Getsoian, A. B.; Wang, T.

C.; Miller, J. T.; Vjunov, A.; Fulton, J. L.; et al. Sintering-Resistant Single-Site Nickel Catalyst Supported by Metal-Organic Framework. *J. Am. Chem. Soc.* **2016**, *138* (6), 1977–1982. https://doi.org/10.1021/jacs.5b12515.

(18) Seufitelli, G. V. S.; Park, J. J. W.; Tran, P. N.; Dichiara, A.; Resende, F. L. P.; Gustafson, R. Kinetics of Ethylene Oligomerization over Ni-H-Beta Catalysts. *J. Catal.* **2021**, *401*, 40–53. https://doi.org/10.1016/j.jcat.2021.07.008.

(19) Nimlos, C. T.; Hoffman, A. J.; Hur, Y. G.; Lee, B. J.; Di Iorio, J. R.; Hibbitts, D. D.; Gounder, R. Experimental and Theoretical Assessments of Aluminum Proximity in MFI Zeolites and Its Alteration by Organic and Inorganic Structure-Directing Agents. *Chem. Mater.* **2020**, *32*, 9277–9298. https://doi.org/10.1021/acs.chemmater.0c03154.

(20) Dědeček, J.; Sobalík, Z.; Wichterlová, B. Siting and Distribution of Framework Aluminium Atoms in Silicon-Rich Zeolites and Impact on Catalysis. *Catal. Rev. - Sci. Eng.* **2012**, *54* (2), 135–223. https://doi.org/10.1080/01614940.2012.632662.

(21) Penkova, A.; Dzwigaj, S.; Kefirov, W. R.; Hadjiivanov, K.; Che, M. Effect of the Preparation Method on the State of Nickel Ions in BEA Zeolites. A Study by Fourier Transform Infrared Spectroscopy of Adsorbed CO and NO, Temperature-Programmed Reduction, and X-Ray Diffraction. *J. Phys. Chem. C* **2007**, *111* (24), 8623–8631. https://doi.org/10.1021/jp071927p.

(22) Hoffman, A. S.; Fang, C. Y.; Gates, B. C. Homogeneity of Surface Sites in Supported Single-Site Metal Catalysts: Assessment with Band Widths of Metal Carbonyl Infrared Spectra. *J. Phys. Chem. Lett.* **2016**, *7* (19), 3854–3860. https://doi.org/10.1021/acs.jpclett.6b01825.

Supporting Information

Effect of zeolite support composition on supported Ni cations reducibility and ethylene dimerization activity

Michael Meloni[1] *and Ron C. Runnebaum*[1,2*]

[1]Department of Chemical Engineering, University of California, Davis, CA, 95616, USA
[2]Department of Viticulture & Enology, University of California, Davis, CA, 95616, USA

Table of Contents

Table S3.1. Ni carbonyl bands observed on Ni-[Al]-Beta and Ni-[Fe]-Beta.

Catalyst	Ni^{2+}-CO	Ni^{+}-$(CO)_{2ss}$	Ni^{+}-$(CO)_{2as}$	Ni^{+}-CO	Reference
Ni-[Al]-Beta	2212	2138	2096	2112	3
Ni-[Fe]-Beta	2206	2133	2089	2103	4

Table S3.2. Activation energies of C_2H_4 dimerization of Ni based supported catalysts.

Catalyst	Ea [kJ/mol]	Reference
Ni-[Al]-Beta	48.8	This Work
Ni-[Al]-Beta	44	5
Ni-[Fe]-Beta Anhydrous	32.4	This Work
Ni-NU-1000	36	6
Ni-[Al]-AFI	77 (Theory)	7
Ni-[Al]-SSZ-24	37	8

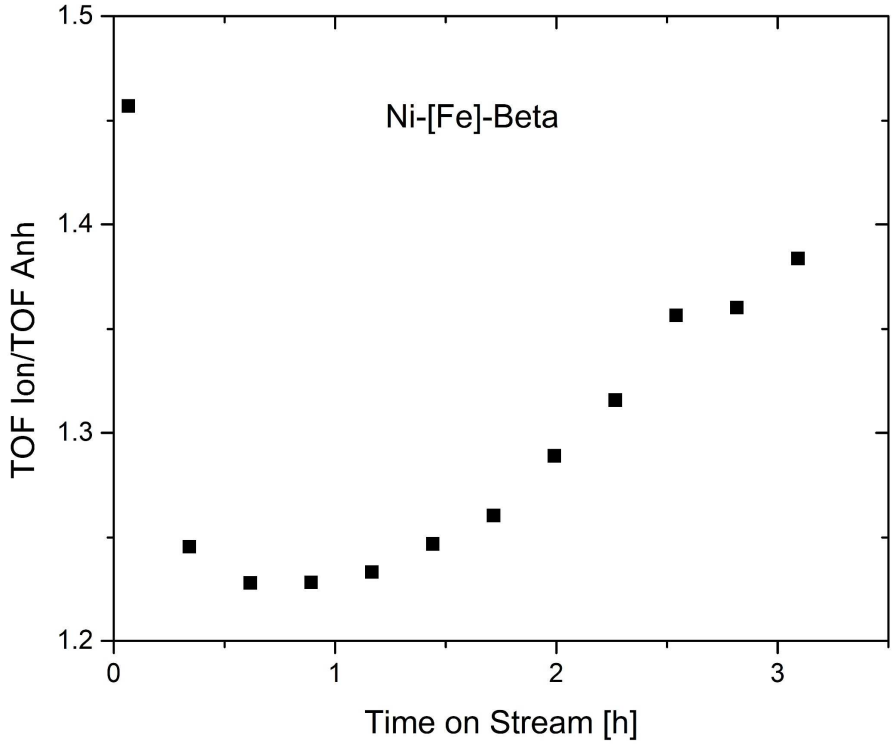

Figure S3.1. The effect of preparation method on activity of Ni-[Fe]-Beta catalysts. The TOF of the catalyst prepared via ion exchange, with $Ni(NO_3)_2$, is approximately 1.3-1.4 more active than the catalyst prepared via anhydrous deposition of $Ni(acac)_2$.

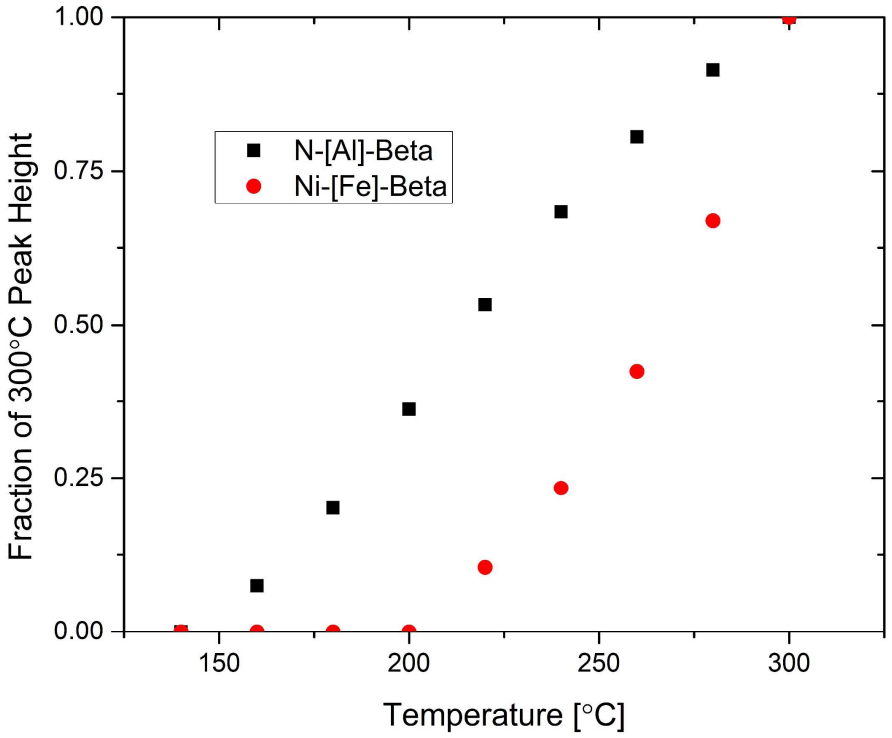

Figure S3.2. The ratio of the fraction of the Ni^{+}-CO band height at a temperature relative to the Ni^{+}-CO band height at 300°C. The Ni^{+}-CO band starts increasing at lower temperature for Ni-[Al]-Beta (black) compared to Ni-[Fe]-Beta (red) indicating the reduction from Ni^{2+} to Ni^{+} takes places at a lower temperature on Ni-[Al]-Beta.

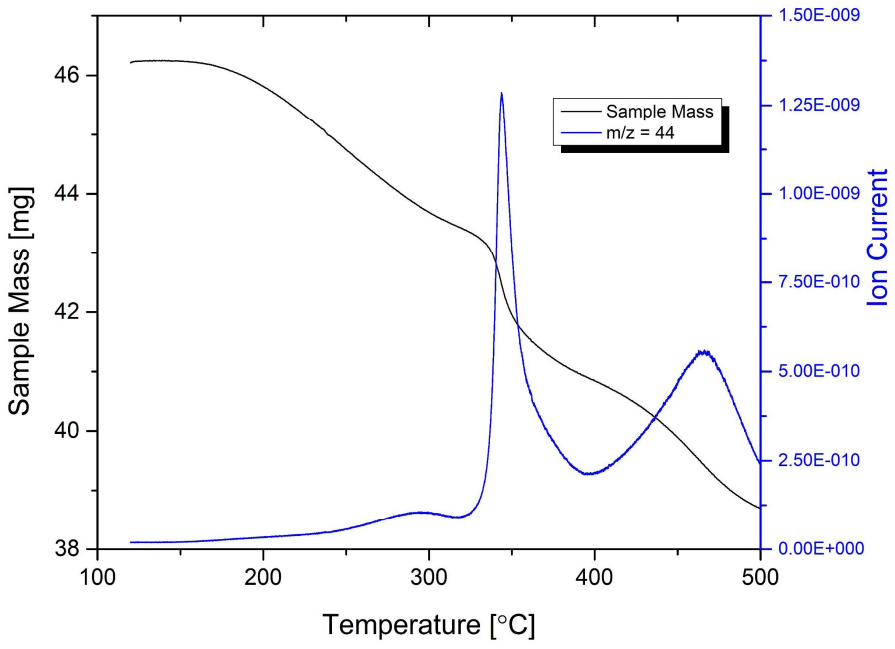

Figure S3.3. Removal of structure directing agent from Na-[Fe]-Beta by calcination in 10% O_2 with ramp rate of 5°C/min. The mass loss and corresponding increase in CO_2 shows a sharp combustion event starting around 330°C and another broader feature starting around 400°C.

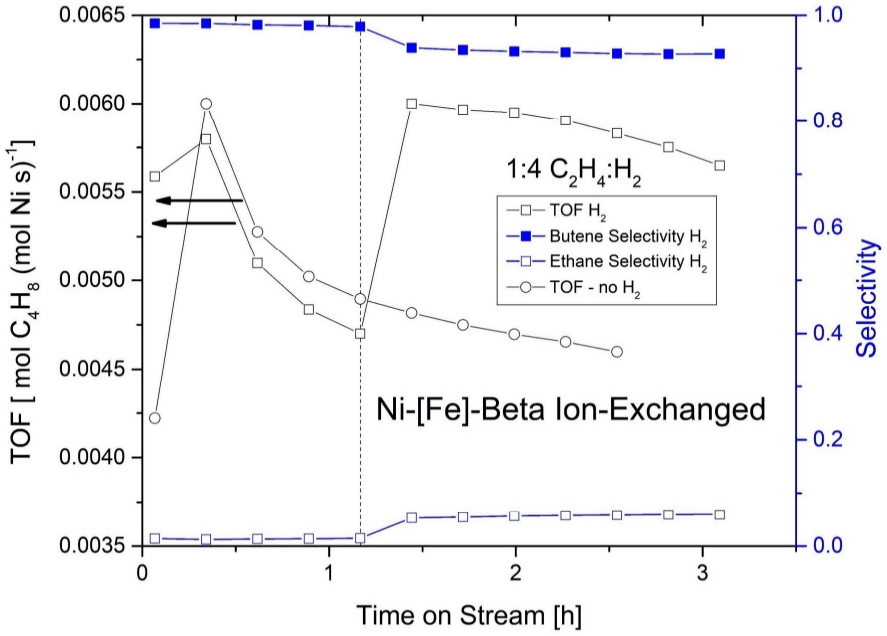

Figure S3.4. The influence of H_2 partial pressure on C_2H_4 dimerization with Ni-[Fe]-Beta prepared via ion exchange, at 180°C and 2.16 kPa C_2H_4. Selectivity is shown for catalyst when H_2 is co-fed at 1 h time on stream. The butene formation rate increase with the addition of co-fed H_2.

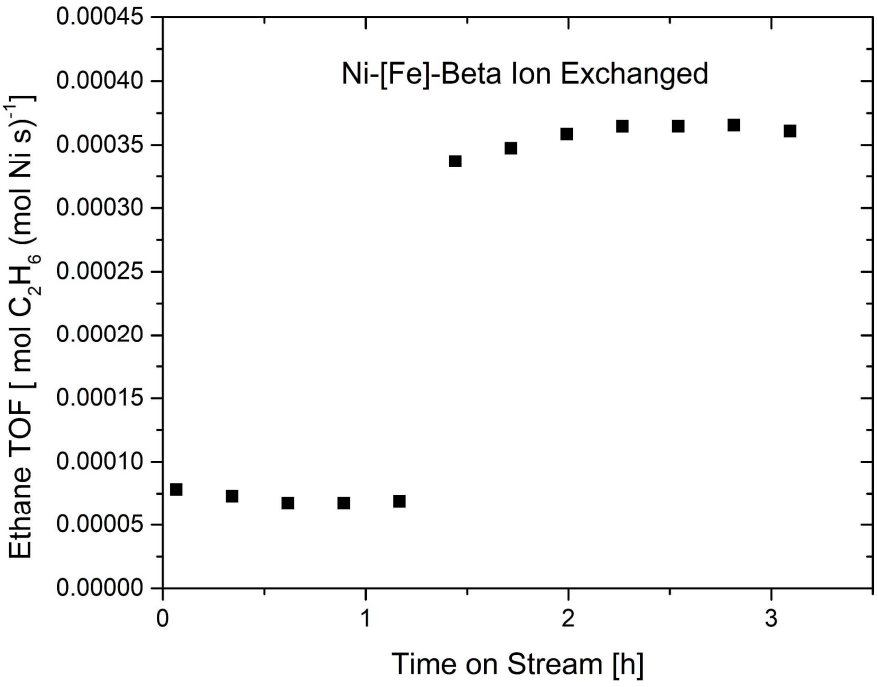

Figure S3.5. The influence of H_2 partial pressure on C_2H_4 hydrogenation with Ni-[Fe]-Beta prepared via ion exchange. The C_2H_4 hydrogenation rate increases by 4.9-fold when H_2 is co-fed.

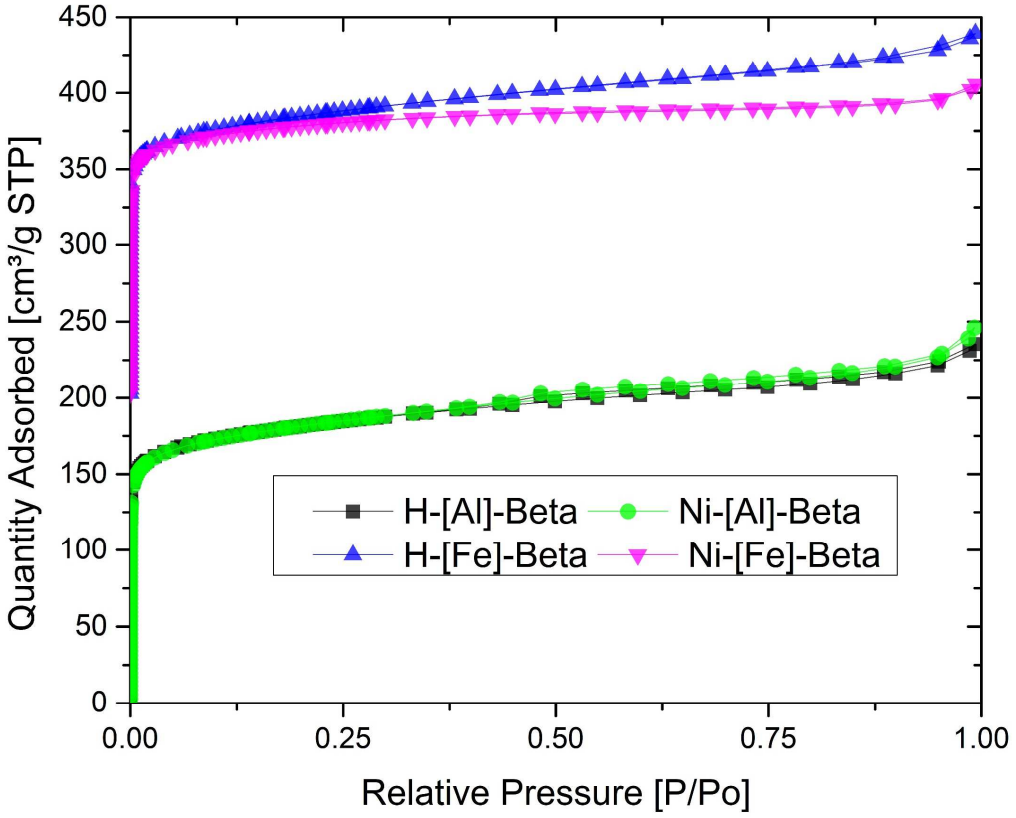

Figure S3.6. N_2 adsorption isotherms for catalysts and supports. Surface areas indicate no significant change in zeolite framework due to Ni deposition. BET surface areas [m^2/g]: H-[Al]-Beta: 690 Ni-[Al]-Beta: 690 H-[Fe]-Beta: 700 Ni-[Fe]-Beta: 690

References

(1) Penkova, A.; Dzwigaj, S.; Kefirov, W. R.; Hadjiivanov, K.; Che, M. Effect of the Preparation Method on the State of Nickel Ions in BEA Zeolites. A Study by Fourier Transform Infrared Spectroscopy of Adsorbed CO and NO, Temperature-Programmed Reduction, and X-Ray Diffraction. *J. Phys. Chem. C* **2007**, *111* (24), 8623–8631. https://doi.org/10.1021/jp071927p.

(2) Meloni, M.; Runnebaum, R. C. Tuning Supported Ni Catalysts by Varying Zeolite Beta Heteroatom Composition: Effects on Ethylene Adsorption and Dimerization Catalysis. *Catal. Sci. Technol.* **2021**, *11* (10), 3393–3401. https://doi.org/10.1039/d1cy00308a.

(3) Seufitelli, G. V. S.; Park, J. J. W.; Tran, P. N.; Dichiara, A.; Resende, F. L. P.; Gustafson, R. Kinetics of Ethylene Oligomerization over Ni-H-Beta Catalysts. *J. Catal.* **2021**, *401*, 40–53. https://doi.org/10.1016/j.jcat.2021.07.008.

(4) Li, Z.; Schweitzer, N. M.; League, A. B.; Bernales, V.; Peters, A. W.; Getsoian, A. B.; Wang, T. C.; Miller, J. T.; Vjunov, A.; Fulton, J. L.; et al. Sintering-Resistant Single-Site Nickel Catalyst Supported by Metal-Organic Framework. *J. Am. Chem. Soc.* **2016**, *138* (6), 1977–1982. https://doi.org/10.1021/jacs.5b12515.

(5) Brogaard, R. Y.; Olsbye, U. Ethene Oligomerization in Ni-Containing Zeolites: Theoretical Discrimination of Reaction Mechanisms. *ACS Catal.* **2016**, *6* (2), 1205–1214. https://doi.org/10.1021/acscatal.5b01957.

(6) Brogaard, R. Y.; Kømurcu, M.; Dyballa, M. M.; Botan, A.; Van Speybroeck, V.; Olsbye, U.; De Wispelaere, K. Ethene Dimerization on Zeolite-Hosted Ni Ions: Reversible Mobilization of the Active Site. *ACS Catal.* **2019**, *9* (6), 5645–5650. https://doi.org/10.1021/acscatal.9b00721.

Chapter 4

Nano sized metallic nickel clusters stabilized on dealuminated Beta zeolite: a highly active and stable ethylene hydrogenation catalyst

Manuscript in preparation for submission

Michael Meloni[1], Jiyun Hong[2], Adam Hoffman[2], Simon R. Bare[2] and Ron C. Runnebaum[1,3,*]
[1]Department of Chemical Engineering, University of California, Davis, CA, 95616, USA
[2]Stanford Synchrotron Radiation Lightsource, SLAC National Accelerator Laboratory, Menlo Park, CA, 94025, USA
[3]Department of Viticulture & Enology, University of California, Davis, CA, 95616, USA

4.1 Abstract

Supported Ni catalysts were synthesized using the Beta zeolite framework, with and without framework Al, as a platform for dispersing Ni. The silanol nest sites of dealuminated zeolite Beta provide isolated cationic Ni sites that can be reduced under relatively mild conditions to create highly dispersed metal clusters. Compared to the Ni sites present in Ni-[Al]-Beta-19, Ni-[DeAl]-Beta exhibit a 20-fold increase in apparent reaction rate for C_2H_4 hydrogenation and is stable with little deactivation over 16 h of catalysis. Ni K-edge X-ray absorption spectroscopy (XAS), as well as CO adsorption monitored with Fourier transform infrared spectroscopy (FTIR), show that in the oxidized Ni-[DeAl]-Beta catalyst Ni is re-occupying vacant silanol nests produced from dealumination. After reductive treatment, XAS shows that approximately 50% of Ni is reduced to metallic Ni, forming clusters approximately 1 nm in size. STEM images show an absence of large (>1 nm) metallic Ni clusters. These results indicate that [DeAl]-Beta can be used to synthesize isolated cationic Ni sites, as well as stabilize highly dispersed metal clusters that can be used as a highly active and stable C_2H_4 hydrogenation catalyst.

4.2 Introduction

Ni catalysts supported on solid materials are widely used for a variety of different reactions such as alkene oligomerization, hydrogenation, carbonylation, and steam reforming.[1–4] As a hydrogenation catalyst, Ni is attractive because it is less expensive than platinum group elements, and can effectively catalyze hydrogenation of a variety of reactants such as alkenes, carbon dioxide, benzene, and fatty acids, among others.[2,5,6] In some instances, the same Ni catalyst is able to catalyze multiple reaction classes, such as the hydrogenation and oligomerization of alkenes. For example, cationic Ni supported on either aluminosilicates or metal organic frameworks (MOFs) is active for C_2H_4 oligomerization, but only cationic Ni on MOFs has been shown to be significantly active for C_2H_4 hydrogenation as well.[7–11] Because both initially prepared forms of Ni are cationic, Ni^{2+} , the differences in support identity are what enable Ni to catalyze both reactions when supported on the MOF. Determining the support effect on the reactivity and stability of a supported metal is important in order to deepen our understanding of how to effectively design

active sites.[12,13] In particular, a greater understanding of how certain supports, such as zeolites, can stabilize and confine small metallic clusters is needed. Metal clusters are widely used in catalysis applications such as hydrogenation, biomass conversion, and H_2 production.[14–16] Controlling the size of clusters, especially under reducing conditions, can increase the effective utilization of the metal as well as increase activity.[17–19] Methods for controlling particle size include confining a metal or protecting the metal site with various ligands.[20–22] Zeolites can be used as a support to confine metallic clusters because of their micropore systems and higher surface area. Zeolite extraframework cation exchange sites are created by the charge imbalance of Al^{3+} in the framework. Metals are typically dispersed after zeolite synthesis but inclusion of the desired metal during synthesis can also result in entrapped metal clusters.[23] In addition, the framework T^{3+} atom can be removed, leaving a silanol nest in its place, which is composed of four terminal silanol groups.[24] These silanol nests can be re-occupied, at least partially, by transition metal cations such as Cr, Co, and Ni to produce isolated metal sites, which are constrained within the zeolite framework.[25–27] It is anticipated that constraining the supported-metal within these sites will result in a modified activity as well as improved stability.

In this work, we examine how the location of Ni is altered by placement within silanol nests in Beta zeolites (framework code BEA) that are created by the removal of framework Al and how this siting affects the electron density, reducibility, catalytic activity, and stability of Ni cations. The two significant placement sites are: (a) Ni in cation extraframework exchange positions, present in Beta zeolites with framework Al, [Al]-Beta, and (b) Ni reoccupying silanol nests which is observed in Beta zeolites that have had framework Al removed, [DeAl]-Beta. It is observed that Ni in extraframework cation exchange positions of [Al]-Beta is not significantly active for C_2H_4 hydrogenation. In contrast, Ni dispersed onto [DeAl]-Beta exhibits high activity and stability for C_2H_4 hydrogenation. It is hypothesized that dispersed Ni in vacant silanol nest sites created by dealumination can be more readily reduced to small metallic clusters that are highly active and stable for C_2H_4 hydrogenation.

4.3 Experimental Section

Catalyst Synthesis. Beta zeolite samples are named as follows: M-[X]-Beta-#, where M is the extraframework cation, X is the framework T site heteroatom, and # is the Si/Al ratio. Aluminum Beta zeolite with Si/Al=19 (NH_4-[Al]-Beta-19) and Si/Al=150 (H-[Al]-Beta-150) were purchased from Zeolyst (CP814C and CP811C-300 respectively). Dealuminated Beta ([DeAl]-Beta) was synthesized by heating NH_4-[Al]-Beta-19 to 80°C in 13M nitric acid for 16 h. Afterwards the zeolite was washed and calcined at 600°C in 10% O_2 for 6 h with ramp rate 2°C/min and a 1 h hold at 120°C before metal deposition. Zeolites purchased from Zeolyst were calcined using the same procedure before metal deposition and stored in glovebox. Calcined Beta zeolites were mixed with $Ni(acac)_2$ (acac= acetylacetonate; STREM chemical min 95%) and n-pentane in a Schlenk flask such that the Ni loading was 1wt% (±0.02%, exact Ni loading was calculated for each sample). The solution was stirred for 24 h and then the solvent was evacuated for 24 h. All work was done in a glovebox or with a Schlenk line to exclude moisture and oxygen. The Ni loaded zeolite was then calcined in 10% O_2 at 600°C for 6 h, ramp rate of 2°C/min with a 1 h hold at 120°C, and then stored in an argon glovebox. The same procedure was used to disperse Ni on amorphous SiO_2 (dehydroxylated at 500°C in air) using $Ni(acac)_2$ (referred to as NiO-SiO_2 anhydrous). NiO-SiO_2 was also prepared using wetness impregnation with $Ni(NO_3)_2$ as the Ni source, with the same calcination procedure used after impregnation (referred to as NiO-SiO_2 aqueous). N_2 adsorption isotherms, Figure S4.1 and Table S4.1, of Ni-Beta catalysts before and after Ni deposition indicate the BET surface area and micropore volume did not change as a result of Ni deposition.

FTIR. Samples stored in a glovebox were pressed into ca. 13 mm self-supporting wafers, with approximately 20 mg of sample, then loaded into a Harrick high temperature transmission cell or the powdered sample was directly loaded into a Pike (Madison, WI) diffuse reflectance cell. Fourier Transform Infrared Spectrometry (FTIR) data were taken by a Bruker Tensor II with 2 cm^{-1} resolution and 128 scans collected per spectrum. Subtraction spectra were obtained by subtracting a spectrum recorded before (under

N_2 flow, 99.9999% Airgas) the sample was exposed to the respective reactive gas (CO, NO, or C_2H_4) from the spectra taken after the sample was exposed to the adsorbate. He (99.999%, Airgas) and C_2H_4 (99.998%, Matheson) were passed through traps containing reduced Cu and molecular sieve to remove oxygen and moisture, respectively. Prior to room temperature CO adsorption the catalyst was reduction with 10% CO (99.999%, Matheson), 90% N_2 at 300°C for 30 min. CO adsorption was also performed after reductions in H_2 (99.999%, Praxair) at various temperatures by reducing in 10% H_2 for 30 min then cooling to room temperature in N_2 before dosing CO. NO (1% NO, 99% N_2, Airgas) adsorption was performed by first drying the catalyst at 300°C in N_2 for 30 min, then cooling to room temperature and dosing NO.

HAADF-STEM. Aberration corrected High Angle Annular Dark Field Scanning Transmission Electron Microscopy (HAADF-STEM) was performed with a JOEL JEM-2100F-AC TEM with 200 kV accelerating voltage; bright and dark field images were collected simultaneously. For zeolite samples, the beam was focused in one area then quickly moved to another to capture the image to minimize any beam damage to the sample. Samples were either dispersed via sonication in methanol then dropped onto a lacey carbon grid (Lacey Carbon 300 mesh, Ted Pella) or the grid was pressed into the desired powder in a glovebox.

Catalysis. Samples were stored and loaded into a 6.35 mm OD quartz tube in an argon filled glovebox (MBraun), then transferred without exposure to air to a three-zone heated furnace. Each sample was diluted with ca. 100mg of α-Al_2O_3 and was held in place with glass wool. Samples were activated in the reactor by heating in 10% H_2 (99.999%, Praxair), 90% N_2 (99.999%, Praxair) at 3°C/min to 300°C and held for 2 h. They were then cooled under 10% H_2 to the reaction temperature of 100°C. C_2H_4 conversion was calculated via carbon balance, with Gas Chromatography (GC) with a calibration previously done using a known gas standard (custom gas mixture from Matheson) analyzed via Flame Ionization Detector. Control experiments, which resulted in no C_2H_4 conversion, were performed with all supports and α-Al_2O_3 with no metal loading.

XAS. X-ray absorption spectroscopy (XAS) measurements at the Ni K-edge (8333 eV) were performed at beamline 9-3 of the Stanford Synchrotron Radiation Lightsource (SSRL) at the SLAC National Laboratory. Beamline 9–3 is a 16-pole, 2-tesla wiggler beamline with a vertically collimating mirror for harmonic rejection and a cylindrically bent mirror for focusing. Incident photon energy was selected by the liquid-nitrogen cooled, double-crystal Si(220) monochromator with a crystal orientation of phi = 0˚. Inside an argon glove box, approximately 40 mg of the Ni-[DeAl]-Beta was loaded into a 3-mm diameter Kapton tube flow-through reactor.[28] The loaded sample made a 10-mm bed and was placed in between two quartz wool plugs. The reactor was mounted on the sample stage at a 45° angle relative to the X-ray beam. Spectra were collected in fluorescence detection mode using a passivated implanted planar silicon (PIPS) detector orthogonal (90°) to the beam path with a Soller slit. The beam size of 1 mm [v] by 3 mm [h] was used. N_2-filled ion chambers were used to measure the incident X-ray intensity, as well as the Ni reference foil which was scanned simultaneously with the sample for energy calibration. At each steady state, four EXAFS scans were collected for signal averaging. Gas flow rates were controlled using mass flow controllers (Brooks) and temperature was controlled with a Eurotherm PID controller. To monitor the gas flows, a mass spectrometer (Hiden QGA) was used throughout the experiment.

For the Ni nanoparticle (NP) spectrum, 1wt% Ni nanoparticles supported on SiO_2 (diameter ranging from 5-6 nm) were synthesized (see SI for more info). Using the same setup as described above, the NiNP was reduced in-situ and the spectra were collected in fluorescence mode using PIPS detector. The XAS spectrum of NiO was recorded from a 7-mm diameter pellet, prepared by diluting NiO in cellulose at 1:15 ratio. The spectra were collected in transmission mode using N_2-filled ion chambers.

The XAS data were processed using Athena software, and the EXAFS analysis was performed using Artemis software.[29] For EXAFS modeling, the scattering paths were simulated using FEFF6 provided by Artemis software. The model structures used to generate the scattering paths were the DFT-optimized Ni in silanol nest site (see SI for more detail) and the bulk fcc Ni crystal structure obtained from Inorganic Crystal Structure Database (ICSD 64989). Details of the EXAFS modeling are in the SI.

4.4 Results

Catalysis: C_2H_4 Hydrogenation. C_2H_4 hydrogenation was performed, after reduction at 300°C for 2 h in 10% H_2, with all synthesized materials to probe differences in catalytic activity. Materials were tested within a similar range of inverse weight space velocity (W/F 0.14-0.18 [mol Ni (mol C_2H_4)$^{-1}$ s]) at 100°C and partial pressures P_{H_2} = 20 kPa, $P_{C_2H_4}$ = 10 kPa for at least 16 h time-on-stream (TOS). All samples (Figure 4.1) exhibit higher initial conversion (TOS < 2 h) that approaches a steady state after a few hours. Table 4.1 compares catalyst performance at 5 h TOS. The conversion of C_2H_4 by Ni supported on each of the three Beta zeolites resulted in C_2H_4 conversion in the order: Ni-[DeAl]-Beta > Ni-[Al]-Beta-150 >> Ni-[Al]-Beta-19, with the Ni-[DeAl]-Beta sample operating at 16-fold higher conversion than that of the Ni-[Al]-Beta-19 sample while operating at a 19% lower inverse space velocity; these differences result in a 20-fold higher apparent reaction rate. Apparent reaction rate is used because most catalysts are not operating at differential conversion and therefore may have mass transport limitations. The catalyst with the lowest deactivation is Ni-[DeAl]-Beta with a ratio of apparent reaction rate at 17 h to initial time on stream of 0.97, while Ni-[Al]-Beta-19 had the lowest ratio of 0.34. C_2H_6 selectivity, reported in Table 4.1, was high with all catalysts tested and varied between 0.99 – 1.0 at 5 h TOS.

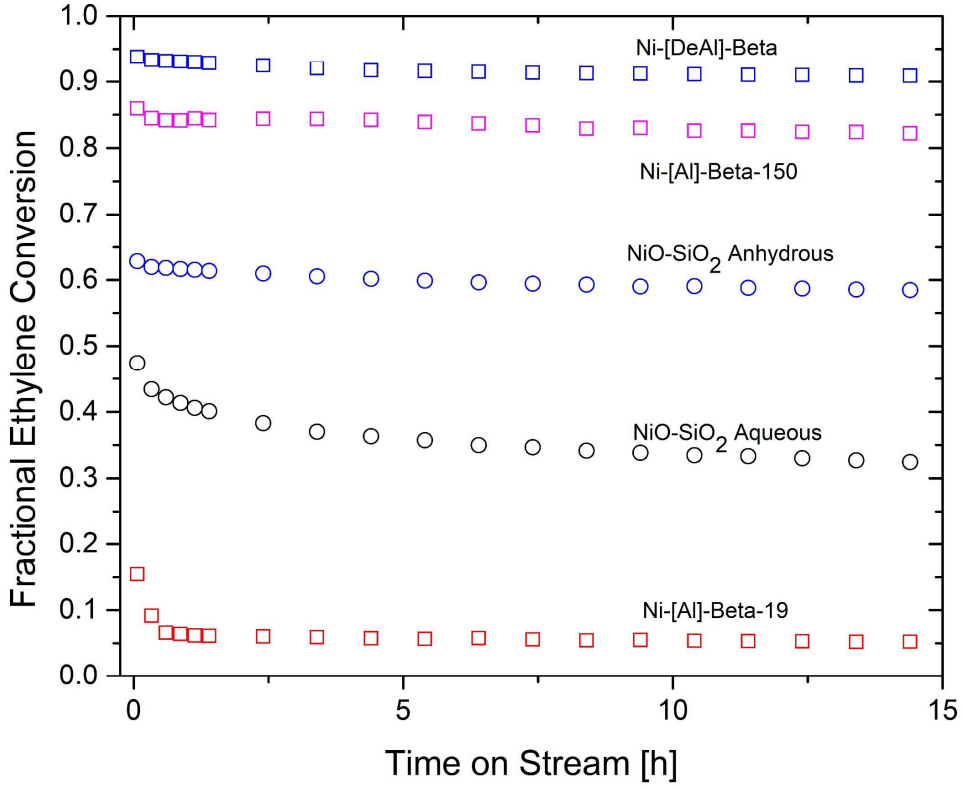

Figure 4.1. C_2H_4 hydrogenation at 100°C and inverse space velocity, W/F, [mol Ni (mol C_2H_4)$^{-1}$ s] for catalysts: Ni-[DeAl]-Beta = 0.14, NiO-SiO_2 anhydrous = 0.16, NiO-SiO_2 aqueous = 0.17, Ni-[Al]-Beta-150 = 0.17, Ni-[Al]-Beta-19 = 0.18, with partial pressures: P_{H2} = 20 kPa, P_{C2H4} = 10 kPa. Samples were reduced at 300°C with 10% H_2 for 2 h, inverse space velocity variations are due to differences in catalyst mass in reactor.

Table 4.1. Summary of C_2H_4 hydrogenation catalysis. Conversion, apparent reaction rate, and selectivity taken from 5 h on stream. Deactivation is summarized by the ratio of the apparent reaction rate at 17 h on steam to the initial reaction rate (Rxn $Rate_{17}$/Rxn $Rate_i$).

Catalyst	W/F [mol Ni (mol C_2H_4)$^{-1}$ s]	C_2H_4 Conversion	Apparent Reaction Rate [mol C_2H_6 (mol Ni)$^{-1}$ s^{-1}]	Rxn $Rate_{17}$/Rxn $Rate_i$	C_2H_6 Selectivity
Ni-[Al]-Beta-19	0.18	0.057	0.30	0.34	0.99
Ni-[Al]-Beta-150	0.17	0.84	5.1	0.95	0.99
Ni-[DeAl]-Beta	0.15	0.92	6.1	0.97	1.0
NiO-SiO_2 – Aqueous	0.17	0.36	2.1	0.66	1.0
NiO-SiO_2 – Anhydrous	0.16	0.60	3.8	0.93	1.0

Ni dispersed by two methods onto amorphous SiO_2 are included for additional comparison: an anhydrous method, which uses a $Ni(acac)_2$ precursor, and a sample prepared using wet impregnation with $Ni(NO_3)_2$ as the Ni source. The sample prepared anhydrously resulted in a 1.7-fold higher conversion than sample prepared via an aqueous method, while operating at a slightly lower inverse space velocity (0.16 [mol Ni (mol C_2H_4)$^{-1}$ s] compared to 0.17 [mol Ni (mol C_2H_4)$^{-1}$ s]). However, Ni-[DeAl]-Beta exhibited 1.6-fold higher apparent reaction rate than NiO-SiO_2 anhydrous and 2.9-fold higher activity than NiO-SiO_2 aqueous. Comparison of initial reaction rates was not possible due to the high initial activity of many of the materials with conversion well above 0.2, which could result in concentration gradients and products formed from reaction adsorbing onto active sites on the catalyst surface.

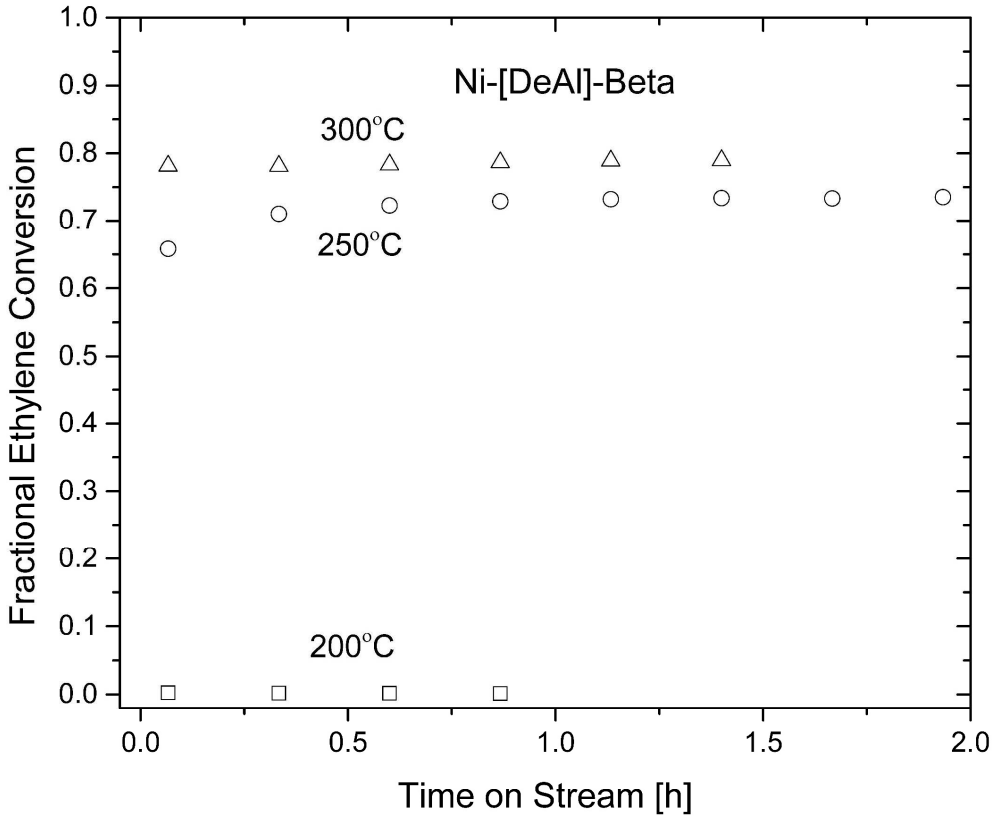

Figure 4.2. C_2H_4 hydrogenation of Ni-[DeAl]-Beta activated at 200°C (square), 250°C (circle), and 300°C (triangle) for 2 h in 10% H_2. All experiments run at the same inverse space velocity, W/F. The activity after reduction at 250°C is 93% of the activity after reduction at 300°C.

C_2H_4 hydrogenation as a function of reduction temperature for Ni-[DeAl]-Beta is shown in Figure 4.2. The sample was reduced in 10% H_2 for 2 h at 200°C, 250°C, and 300°C and subsequently tested for C_2H_4 hydrogenation activity at 100°C. The sample showed no activity after reduction at 200°C but similar activity was observed at the 250°C and 300°C reduction temperatures with conversion of 0.73 and 0.79, respectively, at the same inverse space velocity. Ni-[Al]-Beta-150, shown in Figure S4.2, operates at C_2H_4 conversions of 0.026, 0.52, 0.84, and 0.88 after reduction at 200°C, 250°C, 300°C, and 400°C, respectively. Ni-[Al]-Beta-19, shown in Figure S4.3, exhibits measurable catalysis after activation at 300°C and 400°C. Both reduction temperatures exhibit relatively high loss of initial activity after 5 h on stream of 63% and 62% for 300°C and 400°C activation, respectively.

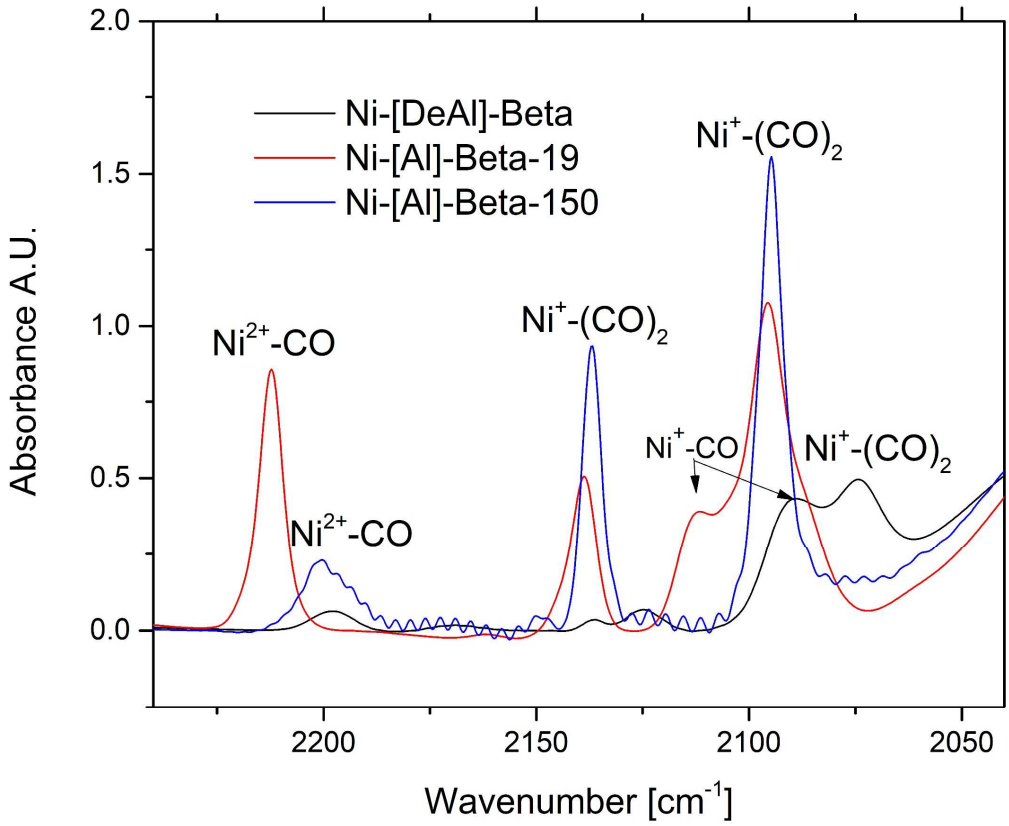

Figure 4.3. CO adsorption onto the Ni-Beta catalysts after reduction in 10% CO at 300°C. Spectra show that Ni-[Al]-Beta-19 and Ni-[DeAl]-Beta contain cationic Ni in extraframework exchange positions and silanol nests respectively (band assignments in Table S2). The two Ni-[Al]-Beta-150 spectra (shortly after

CO exposure and after desorption) show that there is a mixture of Ni is extraframework exchange positions as well as Ni in silanol nests.

CO Adsorption with FTIR. CO adsorption, monitored with FTIR, was used to characterize differences in Ni sites on the various Beta zeolites. Each material was characterized by CO adsorption at room temperature, after reduction with 10% CO at 300°C for 30 min, with spectra taken while purging CO from the IR cell. Reduction in H_2 was also followed by CO adsorption at room temperature was also performed with the most active catalyst, Ni-[DeAl]-Beta, between 185-400°C. Figure 4.3 shows FTIR spectra following CO adsorption onto Ni-[Al]-Beta-19, Ni-[Al]-Beta-150, and Ni-[DeAl]-Beta. The band assignments for CO adsorption are shown in Table S4.2. The carbonyl bands for Ni-[Al]-Beta-19 (2212, 2139, 2095, and 2122 cm^{-1}) and Ni-[DeAl]-Beta (2197, 2137, 2122, 2090, and 2076 cm^{-1}) are consistent with Ni as a cation at extraframework exchange sites and reoccupying silanol nests, respectively.[26,30] CO adsorption onto Ni-[Al]-Beta-19 and Ni-[DeAl]-Beta has been previously reported.[30] CO adsorption with Ni-[Al]-Beta-150, with desorption spectra shown in Figure S4.4, sample indicates that there is a mixture of Ni carbonyl bands that have been previously observed with Ni-[Al]-Beta and Ni-[DeAl]-Beta. Upon initial exposure to CO, bands are seen at 2201, 2138, and 2095 cm^{-1} corresponding to Ni^{2+}-CO, Ni^{+}-$(CO)_2$ and Ni^{+}-$(CO)_2$, respectively. The Ni^{2+}-CO band corresponds to the same Ni^{2+}-CO band seen in Ni-[DeAl]-Beta, while the Ni^{+}-$(CO)_2$ bands correspond to those seen in the Ni-[Al]-Beta-19 sample. As the carbonyl ligands desorb, two Ni^{+}-CO bands are observed at 2113 and 2089 cm^{-1} that correspond to Ni as an extraframework cation and reoccupying silanol nest, respectively. Interestingly, there is no observable Ni^{2+}-CO band corresponding to Ni in an extraframework cation exchange position, which is unexpected due to the observation of Ni^{2+}-CO in Ni-[Al]-Beta-19. This may be because the Ni^{2+} sites in Ni-[Al]-Beta-150 correspond to the more reducible sites in Ni-[Al]-Beta-19. Alternatively, it is possible that the Ni^{2+} sites in Ni-[Al]-Beta-150 are more coordinately saturated and unable to bind CO.

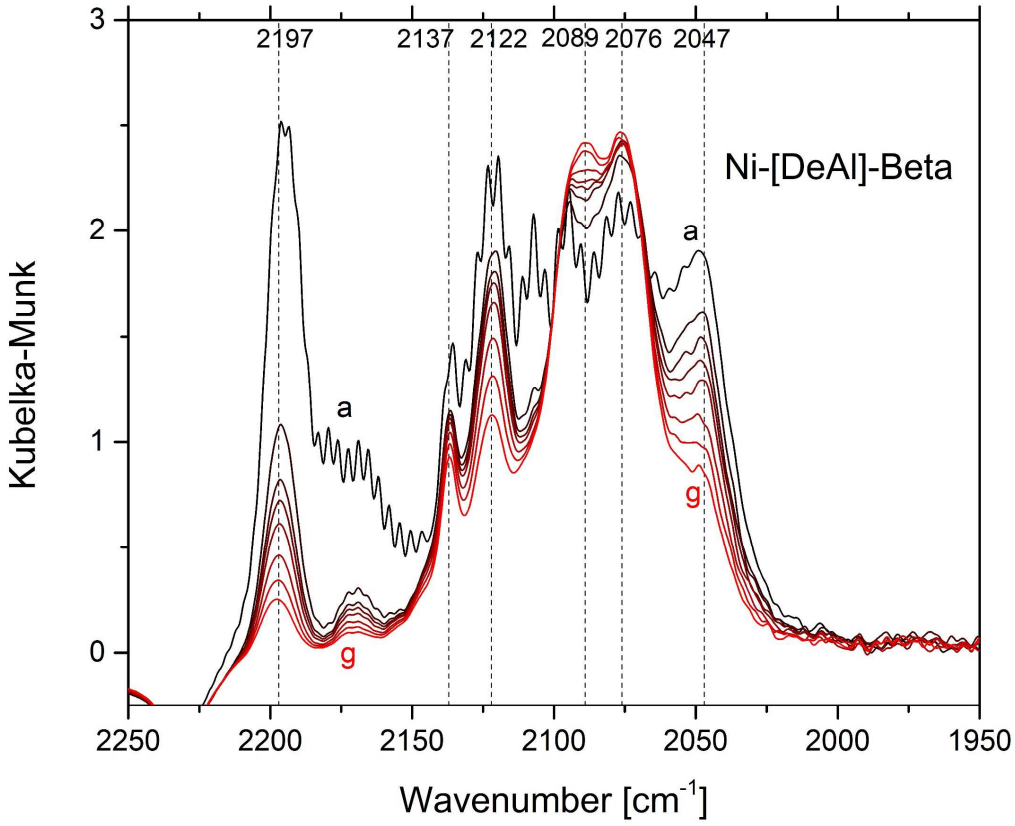

Figure 4.4. CO adsorption at room temperature of Ni-[DeAl]-Beta after reduction at 300°C in 10% H_2. Spectra taken (a-g) as gas phase CO was purged with N_2. Spectra show Ni^{2+} and Ni^{1+} present reoccupying silanol nests as well as Ni^0-CO (2047 cm^{-1}).

CO adsorption after reduction in 10% H_2 was performed with Ni-[DeAl]-Beta to monitor the state of Ni after the activation treatment that was required to catalyze C_2H_4 hydrogenation. CO adsorption after H_2 reduction at 300°C for 30 min of Ni-[DeAl]-Beta is shown in Figure 4.4. Ni carbonyl bands observed at 2197, 2137, 2122, 2090, and 2076 cm^{-1} correspond to carbonyls of cationic Ni in a silanol nest.[30] In addition to these bands that have also been observed after CO reduction, a new band at 2047 cm^{-1} is seen that has previously been assigned to Ni^0-CO.[31] CO adsorption after 10% H_2 reduction of Ni-[DeAl]-Beta as a function of reduction temperature from 185 to 400°C is shown in Figure 4.5. The spectra show the band at 2047 cm^{-1} appearing after reduction at 300°C and 400°C. The Ni^+-$(CO)_x$ bands are present in all spectra indicating that reduction from Ni^{2+} to Ni^+ starts to take place below 185°C.

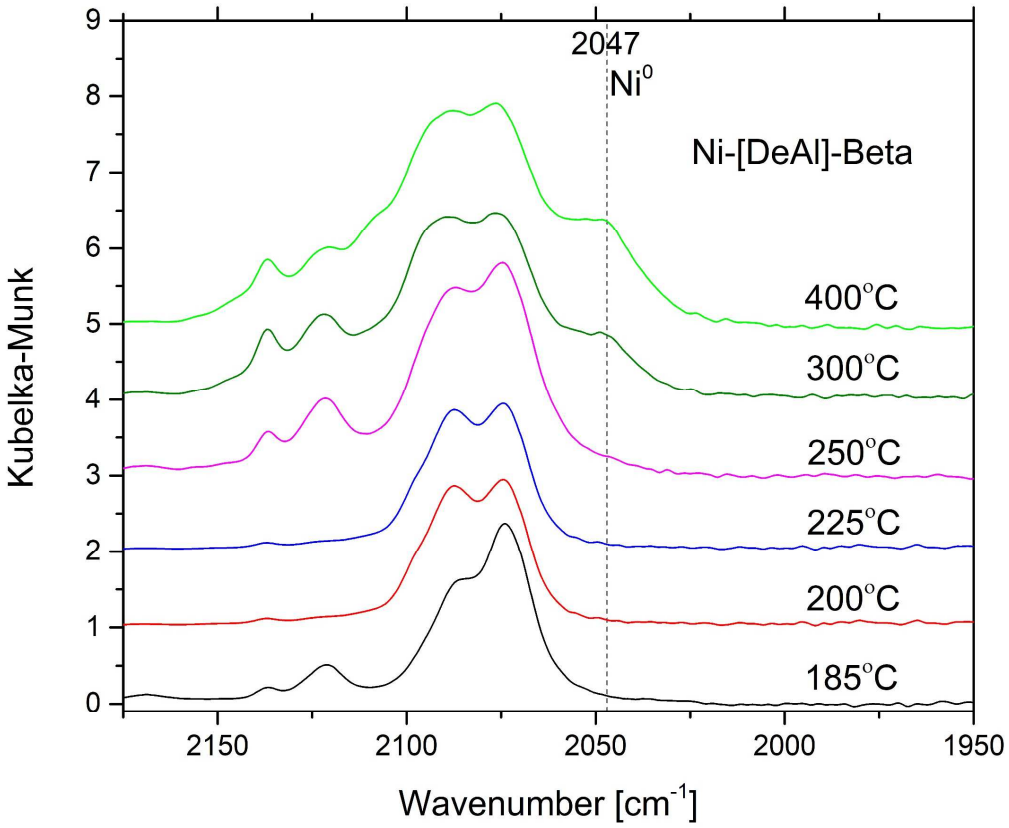

Figure 4.5. FTIR spectra of CO adsorption at 30°C of Ni-[DeAl]-Beta catalysts reduced at temperatures between 185-400°C in 10% H_2. Spectra show a band at 2047 cm^{-1}, assigned to Ni^0-CO, starting to appear at 300°C.

FTIR: *in-situ* C_2H_4 hydrogenation. C_2H_4 hydrogenation (reaction conditions: 100°C, 1:2:3 C_2H_4:H_2:He after reduction at 300°C in 10% H_2) with the Ni-Beta catalysts was monitored using *in-situ* FTIR spectroscopy to look for the presence of adsorbed hydrocarbons that may cause deactivation. In particular, the apparent reaction rate of Ni-[Al]-Beta-19 after 17 h of catalysis is 34% of the initial reaction rate (Table 4.1), which is a larger loss of activity compared to other catalysts. The reaction was stopped by co-feeding 10% CO to prevent any additional buildup of hydrocarbons on the Ni sites after 15 min of hydrogenation. The spectra collected under reaction conditions with Ni-[Al]-Beta-19, Figure S4.5a, show an increase in bands at 2958, 2927, 2875, and 2856 cm^{-1} which correspond to alkyl ligands.[9] The alkyl bands on Ni-[Al]-Beta-19 are visible even in the presence of gas phase C_2H_4. For the other catalysts C_2H_4 was purged from

the cell to make the CH region visible. Gas phase C_2H_6 is visible during hydrogenation with Ni-[Al]-Beta-150, Figure S4.5b. After purging the reactants and products with N_2, the same alkyl bands that were observed with Ni-[Al]-Beta-19 are visible. While Ni-[DeAl]-Beta is under reaction conditions gas phase C_2H_6 bands are seen as shown in Figure S4.5c. In contrast to the other catalysts, there are no alkyl bands present after the reactants and products are purged from the cell.

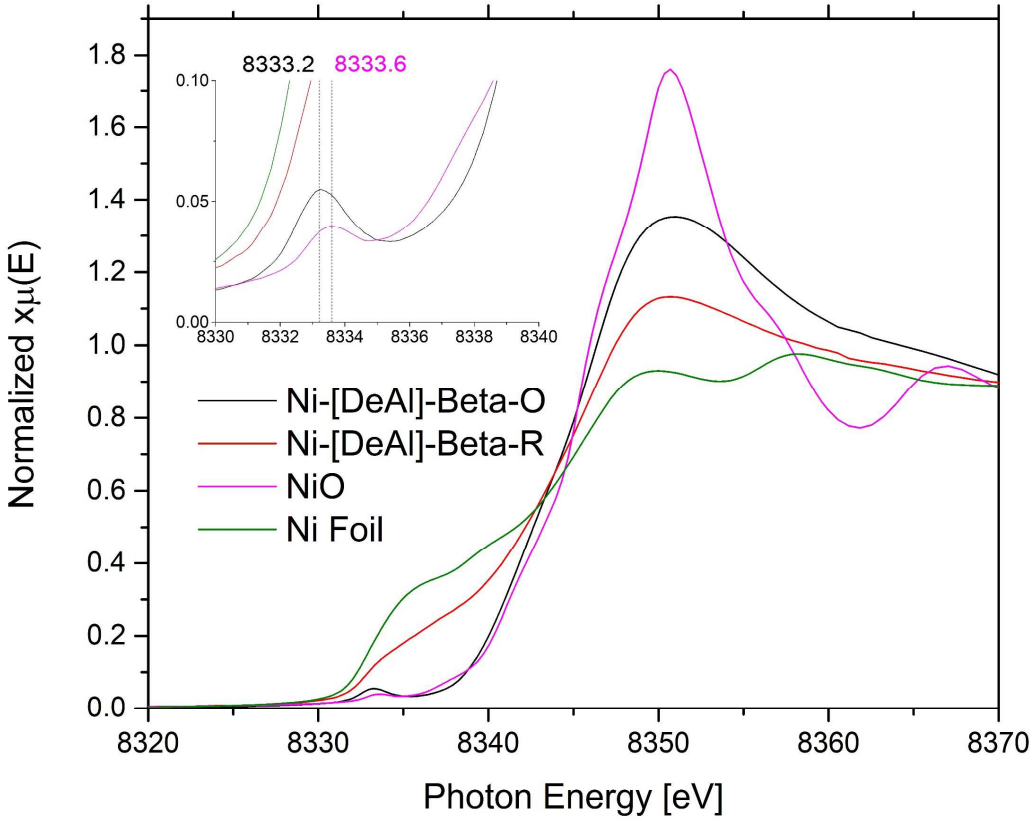

Figure 4.6. XANES spectra of Ni-[DeAl]-Beta after oxidation (Ni-[DeAl]-Beta-O) and after reduction at 300°C in 10% H_2 (Ni-DeAl-Beta-R). The pre-edge peak position suggests that oxidized Ni-[DeAl]-Beta appear to be Ni^{2+} in a tetrahedral like geometry. After reduction LCF analysis (Table S4.6 & Figure S4.6) show approximately 50% of Ni is reduced to a metallic state.

X-Ray Absorption Spectroscopy (XAS)

XAS at Ni K-edge was performed to directly probe the local structure of Ni sites in the most active catalyst, Ni-[DeAl]-Beta, before and after reduction with 10% H_2 at 300°C for 30 min. The X-ray absorption near edge spectra (XANES), Figure 4.6, show that the pre-edge peak of oxidized Ni-[DeAl]-Beta is more intense

and red-shifted by 0.4 eV in energy compared to that of octahedral Ni (NiO reference), consistent with the Ni in tetrahedral geometry.[32] In addition to the pre-edge feature, the whiteline intensity in XANES and the oscillations in low *k* region immediately above the whiteline are also indicative of Ni in tetrahedral geometry. In contrast to octahedral Ni geometry, tetrahedral Ni complexes exhibit lower white line intensity and less intensive oscillations at low *k*.[33,34] It has been reported that tetrahedral Ni complexes show these characteristics in the Ni K-edge XANES region due to fewer coordinated O atoms (4 in T_d vs 6 in O_h).[34] Spectra taken after reduction of Ni-[DeAl]-Beta, at 300°C in 10% H_2 for 30 min, indicate that Ni has partially reduced, as evidenced by decrease in whiteline intensity and the growth of intensity around 8333 eV. Linear combination fitting (LCF) was used to estimate the degree of reduction by using the XANES of the oxidized sample and that of metallic Ni nanoparticles (~5-6 nm size) as the basis spectra. The LCF, Figure S4.6, shows that approximately 50% of the spectra can be represented by the metallic Ni nanoparticle spectra, indicating that approximately 50% of the Ni in Ni-[DeAl]-Beta is reduced. However, it is possible that the high intensity X-ray beam may induce the formation of additional metallic Ni, therefore this value likely represents an upper limit to the amount of metallic Ni formed.[35]

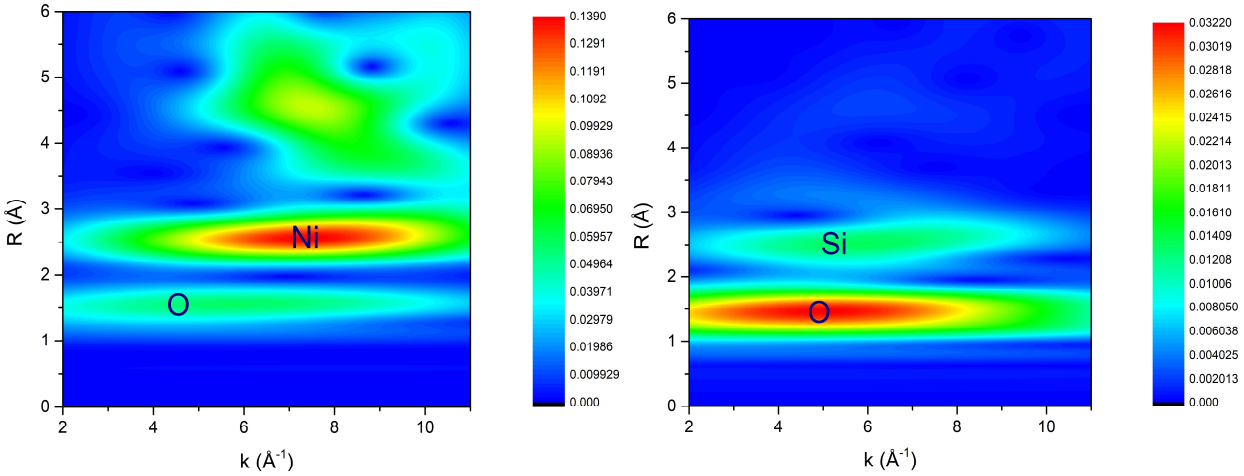

Figure 4.7. Wavelet analysis of reference NiO (left) and oxidized Ni-[DeAl]-Beta (right). The Ni-[DeAl]-Beta spectra show that the scatterer at ca. 2.9 Å is lighter than Ni by comparison with NiO spectra.

Wavelet transform analysis was performed on the EXAFS (Figure S4.7) of the oxidized Ni-[DeAl]-Beta sample to aid in identification the scattering path responsible for the peak in the Fourier transform at ~2.7 Å. The wavelet transforms, Figure 4.7, of Ni-[DeAl]-Beta and NiO show that while NiO's second scattering

path, which represents Ni – Ni scattering, is centered at $R \approx 2.6$ Å and $k \approx 7.0$ Å^{-1}, oxidized Ni-[DeAl]-Beta has its second feature centered at R ≈ 2.5 Å and k ≈ 5.0 Å^{-1}. The fact that the second feature of oxidized Ni-[DeAl]-Beta is centered at lower *k* indicates that it represents the scattering from lower Z element than Ni. The second feature in oxidized Ni-[DeAl]-Beta is therefore assigned to the Ni-Si scattering from the Beta zeolite support[32], in agreement with the XANES interpretation that Ni-[DeAl]-Beta before reduction has Ni^{2+} cations occupying the silanol nest sites. The fitting parameters obtained from the best fit EXAFS modeling of oxidized Ni-[DeAl]-Beta are summarized in Table S4.3. The fit gives total coordination number (CN) of 4.1 ± 1.6 for Ni-O scattering path, and CN of 3.7 ± 2.1 for Ni-Si scattering path. Thus, the EXAFS modeling agrees with the postulation that the Ni is 4-coordinate in silanol nest site in the oxidized catalyst. Based on the LCF analysis of reduced Ni-[DeAl]-Beta, the EXAFS data were modelled using the mixture of oxidized Ni-[DeAl]-Beta and metallic Ni. However, the EXAFS analysis of the reduced state proved to be challenging, as it was difficult to unambiguously distinguish between Ni-Si scattering path and the second Ni-Ni path of metal Ni. To tackle this issue, 50% of the oxidized Ni-[DeAl]-Beta portion of the spectrum in reduced Ni-[DeAl]-Beta was subtracted out, and the spectrum purely representing the reduced fraction of Ni-[DeAl]-Beta sample was constructed. The XANES and EXAFS of the constructed spectrum are shown in Figure S4.7. The XANES of the constructed spectrum (Figure S4.7, pink) has pronounced 8333.0 eV intensity, and its whiteline shape resembles the metallic Ni NP. The EXAFS also resembles that of the Ni NP spectrum throughout *k*-space, but at a slightly lower amplitudes, suggesting that the average size of the nanoparticles formed in the Ni-[DeAl]-Beta sample after reduction are smaller than the 5 – 6 nm sized Ni NP of the reference spectrum. The EXAFS fitting parameters obtained from this constructed spectrum is summarized in Table S4.4-4.5 and the fit is shown in Figure S4.8. Using the CNs of the first to fourth Ni-Ni scattering paths, it was estimated that the average size of the nanoparticles formed in the reduced Ni-[DeAl]-Beta are approximately 1 nm.[36] Another calculation was carried out to determine the number of atoms in a particle that would represent the coordination numbers extracted from the EXAFS fitting (details in SI).[37] The calculation indicates that the CN values from the EXAFS fit correspond to a

particle of 40 – 100 atoms. The metal Ni particles of fcc crystal structure that consist of 40 – 100 atoms have cluster diameters ranging from 0.9 – 1.3 nm. More details of these calculations can be found in SI.

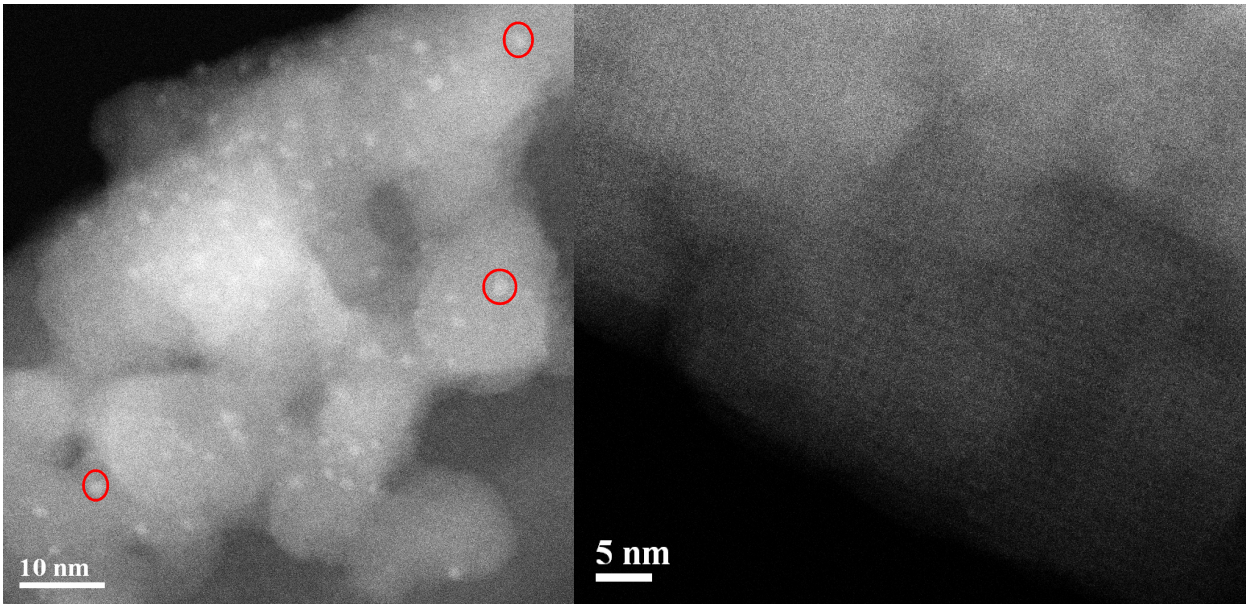

Figure 4.8. NiO-SiO_2 prepared with $Ni(acac)_2$ oxidized sample (left). Red circles indicate representative NiO particles. Ni-[DeAl]-Beta prepared with $Ni(acac)_2$ oxidized sample (right). The absence of abundant large (>1 nm) Ni clusters on Ni-[DeAl]-Beta is confirmed by the lack of visible particles.

High Angle Annular Dark Field Scanning Transmission Electron Microscopy (HAADF-STEM)

HAADF-STEM images were taken of samples before and after reduction at 300°C in 10% H_2 for 2 h. Representative images of NiO-SiO_2, prepared via the anhydrous method, and Ni-[DeAl]-Beta are shown in Figure 4.8. NiO particles (some representative particles circled in red) can be seen in the NiO-SiO_2 sample, with an average particle diameter of 1.6 ± 0.3 nm. Imaging Ni dispersed on a zeolite is difficult due to the low stability of the zeolite under the electron beam and the relatively low Z contrast between Ni and Si compared to other more commonly imaged metals such as Pt, Rh, or Ir.[13,38–41] No NiO or Ni particles are visible on the Ni-[DeAl]-Beta before or after reduction (post reduction samples were briefly exposed to air during transfer to the TEM). Images taken after reduction of Ni-[DeAl]-Beta at 300°C for 2 h in 10% H_2, shown in Figure S4.9, also lack any evidence of NiO or Ni particles. Energy-dispersive X-ray spectroscopy (EDS), Figure S4.10, confirmed the presence of Ni in the sample area imaged. To validate imaging

capabilities a sample of Ni-[Al]-Beta-150 with 2.7wt% Ni was synthesized and imaged. Figure S4.11, shows a resulting dark-field image that confirms the presence of NiO clusters between 1.2 – 2.1 nm.

4.5 Discussion

C_2H_4 Hydrogenation Activity and Stability

Ni-[DeAl]-Beta, initially composed of Ni re-occupying empty silanol nests, exhibits approximately 20-fold higher apparent reaction rate and significantly less deactivation (Table 4.1) than Ni-[Al]-Beta-19, where the Ni is present as extraframework cations. The results show that the Ni sites present in Ni-[Al]-Beta-19 are comparatively less active for hydrogenation. This is enhanced by the relatively large deactivation observed with a 60% decrease in conversion in just 1 h of catalysis. Because Ni-[Al]-Beta is commonly used as a oligomerization catalyst, it is likely the cationic Ni sites that have not been reduced can still catalyze C_2H_4 oligomerization.[9] These oligomerization products can then build up on the catalyst, Figure S4.5a, and block the active Ni sites. These results suggest that the extraframework Ni sites are either active for hydrogenation but deactivate quickly due to buildup of alkyl ligands, or these Ni sites create oligomerization products that then adsorb and deactivate the Ni sites that are active for hydrogenation. Ni-[DeAl]-Beta showed no alkyl bands during or after hydrogenation (Figure S4.5c) and was significantly more stable than Ni-[Al]-Beta-19 suggesting that the Ni associated with framework Al are involved in the relatively fast deactivation of Ni-[Al]-Beta-19. C_2H_4 hydrogenation on NiO-SiO_2 catalysts was also studied as a reference to compare to various supported Ni-Beta catalysts. Between the two preparation methods used for Ni supported on amorphous SiO_2, the anhydrous use of $Ni(acac)_2$ precursor leads to an apparent reaction rate 1.8-fold greater than that of the material prepared by wetness impregnation with $Ni(NO_3)_2$. The difference in activity is attributed to smaller average particle size as well as smaller standard deviation of Ni particles dispersed on SiO_2 using $Ni(acac)_2$ compared to $Ni(NO_3)_2$ (1.6 ± 0.3 nm and 3.2 ± 4 nm respectively) as observed through HAADF-STEM. These factors result in more sites being available for the same Ni weight loading on these amorphous supports.

It was observed that the Ni catalysts could regain their initial activity by reactivating them by using the initial activation conditions (typically at 300°C, 10% H_2 for 2 h). Reactivation of NiO-SiO_2 (aq), Figure S4.12, shows that the catalyst regains the same activity after reactivation with the same conditions. These results suggest that the mechanism of deactivation is a build-up of adsorbed species that are removed upon re-activation. If the mechanism of deactivation was sintering, i.e., a loss of active sites, it would be expected that upon reactivation of the catalyst the original activity would not be able to be recovered. The outcomes here suggest sintering is not the main deactivation mechanism as repeated reduction would be expected to exacerbate the issue. Instead, we propose deactivation through the build-up adsorbed alkyl species that accumulate on the active Ni sites and deactivate them.

Nature of Ni sites on Ni-[DeAl]-Beta

XAS was performed on the oxidized Ni-[DeAl]-Beta catalyst to directly probe the state of Ni and local environment of Ni. While CO and NO adsorption from FTIR suggest that Ni is occupying silanol nests, XAS directly probes all Ni in the sample and can be used to look for the evidence of NiO clusters that cannot be observed with CO or NO adsorption. Wavelet analysis is a useful because it allows the use of information from both the Fourier transform as well as k space. The analysis can be used to rule out the presence NiO on oxidized Ni-[DeAl]-Beta by comparing the spectrum to that of NiO. The second scattering path of Ni-[DeAl]-Beta is centered around R = 2.5 Å and k = 5 $Å^{-1}$ which is at lower k than the second (Ni – Ni) scattering path of NiO. The XANES pre-edge peak position and intensity suggest Ni is in a tetrahedral-like geometry, which is consistent with tetrahedral/pseudo-tetrahedral geometry of Ni reoccupying silanol nests.[42] The EXAFS fit of oxidized Ni-[DeAl]-Beta is also consistent with distorted tetrahedral Ni sites. To generate the scattering paths for EXAFS fitting, the DFT optimized structure of Ni in silanol nest site was used (see SI for details). The EXAFS of Ni-[DeAl]-Beta is best fit with CN of 1.8 ± 0.7 and 2.3 ± 1.2 for two different sets of Ni-O paths at 1.91 ± 0.04 Å and 2.06 ± 0.04 Å, respectively, and a CN of 3.3 ± 1.7 for Ni-Si path at 3.17 ± 0.03 Å. The resulting CN values, within error, are in good agreement with Ni reoccupying the silanol nest site in tetrahedral coordination. A model using one set of Ni – O distance at

1.99 ± 0.01 Å with CN of 5.3 ± 0.9 also results in good-quality fit, but it gives a relatively large mean square disorder of 0.013 $Å^2$, while the fit using two sets of Ni-O distances give mean square disorder of 0.002 $Å^2$ for both distances. Both fitting models indicate Ni reoccupying the silanol nest site with two different sets of Ni – O bond distances. The details of EXAFS fitting parameters for both models are summarized in Table S4.3. These results, along with HAADF-STEM and CO adsorption, show that Ni is reoccupying silanol nests with a distorted tetrahedral geometry.

The synthesis of isolated Ni cations after high temperature oxidation, 600°C in 10% O_2 for 6 h, following anhydrous deposition of $Ni(acac)_2$ shows that Ni is more stable as isolated cations within the zeolite framework than as extraframework NiO clusters. The Ni deposition method onto [DeAl]-Beta does not involve a reaction between an acac ligand and an acid site to anchor the complex to the support, in contrast to what has been observed with various metals interacting with zeolites that have H^+ extraframework cations.[12,43] It is not likely that the acac ligands would preferentially interact with silanol nest sites during deposition rather than other silanols present on the zeolite. Therefore, the oxidation appears to allow the Ni cations sufficient mobility to reoccupy silanol nests, which are more favorable than Ni agglomerating into extraframework NiO clusters. The results may be similar to what has recently been observed with Pd on chabazite, where high temperature oxidation enables the dispersion of Pd to extraframework cation sites.[44]

XAS spectra were recorded after reduction at 300°C; the reduction was not followed *in-situ* because exposure to the X-ray beam increases the degree of reduction of the Ni-[DeAl]-Beta sample.[35] The average size of the metal clusters was estimated from the EXAFS fitting give an approximate size of 1 nm (0.9 – 1.2 nm) using two methods to estimate cluster size. It is likely that given the effects of the X-ray beam on the Ni sites, that 1 nm represents the upper limit of the size of the Ni clusters. While the STEM images do not show the presence of large Ni clusters, the predicted <1 nm clusters are also not visible likely due to the low Z contrast between Ni and Si, as well as the imaging conditions used to minimize damage to the zeolite framework. The high activity of Ni-[DeAl]-Beta is likely due to the small size of the metallic clusters formed after reduction.

Activation of Ni-Beta Catalysts

The catalytic activity of Ni-[DeAl]-Beta was tested after activation in 10% H_2 at 200°C, 250°C, and 300°C to determine if less harsh reducing conditions could be used to enable C_2H_4 hydrogenation. It was found that for activation at 250°C, as shown in Figure 4.8, the apparent reaction rate was 6.3 [mol C_2H_6 (mol Ni)$^{-1}$ s^{-1}] which is only 7% lower than what is measured with activation at 300°C (6.8 [mol C_2H_6 (mol Ni)$^{-1}$ s^{-1}] for equivalent TOS of 300°C activated sample). CO adsorption of reduction temperatures between 185–400°C, shown in Figure 4.5, show qualitatively that there is significantly less Ni^0 in the sample reduced at 250°C, as suggested by decreased intensity of the Ni^0-CO band at 2047 cm^{-1}. One explanation is that the first Ni^0 clusters formed at 250°C are highly active and result in similar activity to the more reduced state of Ni in the catalyst reduced at 300°C. Another explanation is that, similar to what is seen with Ni-NU-1000,[8] cationic Ni dispersed in silanol nests is highly active for hydrogenation as well, but requires activation around 250°C instead of the 200°C used with Ni-NU-1000. While outside of the scope of this manuscript, it may be possible to distinguish between two different active sites by kinetic measurements.[45] Similar experiments were run with Ni-[Al]-Beta-150, Figure S4.2, with reduction temperatures between 200–400°C. In contrast to the Ni-[DeAl]-Beta sample, there is a more significant difference between reduction at 300°C and 250°C with 38% lower activity when activated at 250°C. Ni-[Al]-Beta-19 activity increases significantly as the reduction temperature is increased from 300°C to 400°C as seen in Figure S4.3. This is consistent with extraframework cation exchange Ni sites requiring high temperature reduction to be active for hydrogenation and agrees with literature regarding temperature programmed reduction of Ni-[Al]-Beta that indicates cationic Ni in extraframework positions is relatively resistant to reduction.[46]

4.6 Conclusions

In this study, differences in coordination environment of Ni dispersed on Beta zeolites were examined to determine effects on the electronic properties, catalytic activity, and stability under C_2H_4 hydrogenation conditions. Adsorption experiments with both CO and NO as well as XAS show that two significant Ni

environments in the Ni-Beta catalysts are 1) Ni in extraframework cation exchange sites in Beta zeolites with framework Al and 2) Ni re-occupying empty silanol nests created by the dealumination process. It was observed that in Ni-[Al]-Beta-19 Ni was present in extraframework cation exchange sites, while in Ni-[DeAl]-Beta Ni re-occupied silanol nests. The Ni in Ni-[Al]-Beta-150 was present as a mixture of Ni in silanol nests and extraframework exchange positions. The mechanism of deactivation was found to be an accumulation of alkyl ligands that inactivates Ni sites; these sites were successfully regenerated and reused. The Beta zeolites with partial or complete dealumination exhibit significantly higher activity than either $NiO\text{-}SiO_2$ catalyst or Ni-[Al]-Beta-19. After reduction of the Ni-[DeAl]-Beta catalyst, approximately nanometer-sized metallic Ni clusters are stabilized, as characterized by XAS and STEM. The silanol nests provide isolated cationic Ni sites that can be easily reduced at relatively low temperatures to form highly dispersed metallic Ni with high C_2H_4 hydrogenation activity.

4.7 Acknowledgments

The authors would like to acknowledge support from the Rossi Endowment at UC Davis (RR). Use of the Stanford Synchrotron Radiation Light Source (SSRL, beamline 9-3), SLAC National Accelerator Laboratory is supported by the U.S. Department of Energy, office of Basic Energy Sciences under Contract No. DE-AC02-76SF00515. Additional support by the Consortium for Operando and Advanced Catalyst Characterization via Electronic Spectroscopy and Structure (Co-ACCESS) at SLAC is acknowledged. Co-ACCESS is supported by the U.S. Department of Energy, Office of Science, Office of Basic Energy Sciences, Chemical Sciences, Geosciences and Biosciences Division.

4.8 References

(1) Finiels, A.; Fajula, F.; Hulea, V. Nickel-Based Solid Catalysts for Ethylene Oligomerization-a Review. *Catal. Sci. Technol.* **2014**, *4* (8), 2412–2426. https://doi.org/10.1039/c4cy00305e.

(2) Millet, M. M.; Algara-Siller, G.; Wrabetz, S.; Mazheika, A.; Girgsdies, F.; Teschner, D.; Seitz, F.; Tarasov, A.; Levchenko, S. V.; Schlögl, R.; et al. Ni Single Atom Catalysts for CO 2 Activation. *J. Am. Chem. Soc.* **2019**, *141*, 2451–2461. https://doi.org/10.1021/jacs.8b11729.

(3) Xie, H.; Lin, T.; Shi, L.; Meng, X. Acetylene Carbonylation over Ni-Containing Catalysts: Role of Surface Structure and Active Site Distribution. *RSC Adv.* **2016**, *6* (99), 97285–97292. https://doi.org/10.1039/C6RA17567H.

(4) Wang, W.; Gong, J. Methanation of Carbon Dioxide: An Overview. *Front. Chem. Eng. China* **2011**, *5* (1), 2–10. https://doi.org/10.1007/s11705-010-0528-3.

(5) Savva, P. G.; Goundani, K.; Vakros, J.; Bourikas, K.; Fountzoula, C.; Vattis, D.; Lycourghiotis, A.; Kordulis, C. Benzene Hydrogenation over Ni/Al2O3 Catalysts Prepared by Conventional and Sol-Gel Techniques. *Appl. Catal. B Environ.* **2008**, *79* (3), 199–207. https://doi.org/10.1016/j.apcatb.2007.10.023.

(6) Fernández, M. B.; Tonetto, G. M.; Crapiste, G. H.; Damiani, D. E. Revisiting the Hydrogenation of Sunflower Oil over a Ni Catalyst. *J. Food Eng.* **2007**, *82* (2), 199–208. https://doi.org/10.1016/j.jfoodeng.2007.02.010.

(7) Hulea, V.; Fajula, F. Ni-Exchanged AlMCM-41 - An Efficient Bifunctional Catalyst for Ethylene Oligomerization. *J. Catal.* **2004**, *225* (1), 213–222. https://doi.org/10.1016/j.jcat.2004.04.018.

(8) Li, Z.; Schweitzer, N. M.; League, A. B.; Bernales, V.; Peters, A. W.; Getsoian, A. B.; Wang, T. C.; Miller, J. T.; Vjunov, A.; Fulton, J. L.; et al. Sintering-Resistant Single-Site Nickel Catalyst Supported by Metal-Organic Framework. *J. Am. Chem. Soc.* **2016**, *138* (6), 1977–1982. https://doi.org/10.1021/jacs.5b12515.

(9) Moussa, S.; Concepción, P.; Arribas, M. A.; Martínez, A. Nature of Active Nickel Sites and Initiation Mechanism for Ethylene Oligomerization on Heterogeneous Ni-Beta Catalysts. *ACS Catal.* **2018**, *8* (5), 3903–3912. https://doi.org/10.1021/acscatal.7b03970.

(10) Finiels, A.; Fajula, F.; Hulea, V. Nickel-Based Solid Catalysts for Ethylene Oligomerization – a Review. *Catal. Sci. Technol.* **2014**, *4* (8), 2412–2426. https://doi.org/10.1039/C4CY00305E.

(11) Li, Z.; Peters, A. W.; Liu, J.; Zhang, X.; Schweitzer, N. M.; Hupp, J. T.; Farha, O. K. Size Effect of the Active Sites in UiO-66-Supported Nickel Catalysts Synthesized: Via Atomic Layer Deposition for Ethylene Hydrogenation. *Inorg. Chem. Front.* **2017**, *4* (5), 820–824.

https://doi.org/10.1039/c7qi00056a.

(12) Lu, J.; Aydin, C.; Browning, N. D.; Gates, B. C. Oxide- and Zeolite-Supported Isostructural Ir(C 2H 4) 2 Complexes: Molecular-Level Observations of Electronic Effects of Supports as Ligands. *Langmuir* **2012**, *28* (35), 12806–12815. https://doi.org/10.1021/la302522a.

(13) Flytzani-Stephanopoulos, M.; Gates, B. C. Atomically Dispersed Supported Metal Catalysts. *Annu. Rev. Chem. Biomol. Eng.* **2012**, *3* (1), 545–574. https://doi.org/10.1146/annurev-chembioeng-062011-080939.

(14) Wang, N.; Sun, Q.; Bai, R.; Li, X.; Guo, G.; Yu, J. In Situ Confinement of Ultrasmall Pd Clusters within Nanosized Silicalite-1 Zeolite for Highly Efficient Catalysis of Hydrogen Generation. *J. Am. Chem. Soc.* **2016**, *138* (24), 7484–7487. https://doi.org/10.1021/jacs.6b03518.

(15) Song, W.; Zhao, C.; Lercher, J. A. Importance of Size and Distribution of Ni Nanoparticles for the Hydrodeoxygenation of Microalgae Oil. *Chem. - A Eur. J.* **2013**, *19* (30), 9833–9842. https://doi.org/10.1002/chem.201301005.

(16) Zhang, L.; Zhou, M.; Wang, A.; Zhang, T. Selective Hydrogenation over Supported Metal Catalysts: From Nanoparticles to Single Atoms. *Chem. Rev.* **2020**, *120* (2), 683–733. https://doi.org/10.1021/acs.chemrev.9b00230.

(17) Campelo, J. M.; Luna, D.; Luque, R.; Marinas, J. M.; Romero, A. A. Sustainable Preparation of Supported Metal Nanoparticles and Their Applications in Catalysis. *ChemSusChem* **2009**, *2* (1), 18–45. https://doi.org/10.1002/cssc.200800227.

(18) White, R. J.; Luque, R.; Budarin, V. L.; Clark, J. H.; Macquarrie, D. J. Supported Metal Nanoparticles on Porous Materials. Methods and Applications. *Chem. Soc. Rev.* **2009**, *38* (2), 481–494. https://doi.org/10.1039/b802654h.

(19) Ndolomingo, M. J.; Bingwa, N.; Meijboom, R. Review of Supported Metal Nanoparticles: Synthesis Methodologies, Advantages and Application as Catalysts. *J. Mater. Sci.* **2020**, *55* (15), 6195–6241. https://doi.org/10.1007/s10853-020-04415-x.

(20) Vitale, G.; Molero, H.; Hernandez, E.; Aquino, S.; Birss, V.; Pereira-Almao, P. One-Pot

Preparation and Characterization of Bifunctional Ni-Containing ZSM-5 Catalysts. *Appl. Catal. A Gen.* **2013**, *452*, 75–87. https://doi.org/10.1016/j.apcata.2012.11.026.

(21) Bo, Z.; Ahn, S.; Ardagh, M. A.; Schweitzer, N. M.; Canlas, C. P.; Farha, O. K.; Notestein, J. M. Synthesis and Stabilization of Small Pt Nanoparticles on TiO2 Partially Masked by SiO2. *Appl. Catal. A Gen.* **2018**, *551* (September 2017), 122–128. https://doi.org/10.1016/j.apcata.2017.11.017.

(22) Mian, M. R.; Redfern, L. R.; Pratik, S. M.; Ray, D.; Liu, J.; Idrees, K. B.; Islamoglu, T.; Gagliardi, L.; Farha, O. K. Precise Control of Cu Nanoparticle Size and Catalytic Activity through Pore Templating in Zr Metal–Organic Frameworks. *Chem. Mater.* **2020**, *32* (7), 3078–3086. https://doi.org/10.1021/acs.chemmater.0c00059.

(23) Wu, Z.; Goel, S.; Choi, M.; Iglesia, E. Hydrothermal Synthesis of LTA-Encapsulated Metal Clusters and Consequences for Catalyst Stability, Reactivity, and Selectivity. *J. Catal.* **2014**, *311*, 458–468. https://doi.org/10.1016/j.jcat.2013.12.021.

(24) Silaghi, M. C.; Chizallet, C.; Raybaud, P. Challenges on Molecular Aspects of Dealumination and Desilication of Zeolites. *Microporous Mesoporous Mater.* **2014**, *191*, 82–96. https://doi.org/10.1016/j.micromeso.2014.02.040.

(25) Baran, R.; Onfroy, T.; Casale, S.; Dzwigaj, S. Introduction of Co into the Vacant T-Atom Sites of SiBEA Zeolite as Isolated Mononuclear Co Species. *J. Phys. Chem. C* **2014**, *118* (35), 20445–20451. https://doi.org/10.1021/jp506375v.

(26) Penkova, A.; Dzwigaj, S.; Kefirov, W. R.; Hadjiivanov, K.; Che, M. Effect of the Preparation Method on the State of Nickel Ions in BEA Zeolites. A Study by Fourier Transform Infrared Spectroscopy of Adsorbed CO and NO, Temperature-Programmed Reduction, and X-Ray Diffraction. *J. Phys. Chem. C* **2007**, *111* (24), 8623–8631. https://doi.org/10.1021/jp071927p.

(27) Yuvaraj, S.; Palanichamy, M.; Krishnasamy, V. Chromium Substitution in a Large-Pore High-Silica Zeolite BEA: Synthesis, Characterisation and Catalytic Activity. *Chem. Commun.* **1996**, No. 24, 2707–2708.

(28) Hoffman, A. S.; Singh, J. A.; Bent, S. F.; Bare, S. R. In Situ Observation of Phase Changes of a Silica-Supported Cobalt Catalyst for the Fischer-Tropsch Process by the Development of a Synchrotron-Compatible InÂ Situ/Operando Powder X-Ray Diffraction Cell. *J. Synchrotron Radiat.* **2018**, *25* (6), 1673–1682. https://doi.org/10.1107/S1600577518013942.

(29) Ravel, B.; Newville, M. ATHENA, ARTEMIS, HEPHAESTUS: Data Analysis for X-Ray Absorption Spectroscopy Using IFEFFIT. *J. Synchrotron Radiat.* **2005**, *12* (4), 537–541. https://doi.org/10.1107/S0909049505012719.

(30) Meloni, M.; Runnebaum, R. C. Tuning Supported Ni Catalysts by Varying Zeolite Beta Heteroatom Composition: Effects on Ethylene Adsorption and Dimerization Catalysis. *Catal. Sci. Technol.* **2021**, *11* (10), 3393–3401. https://doi.org/10.1039/d1cy00308a.

(31) Mihaylov, M.; Hadjiivanov, K.; Knözinger, H. Formation of Ni(CO)4 during the Interaction between CO and Silica-Supported Nickel Catalyst: An FTIR Spectroscopic Study. *Catal. Letters* **2001**, *76* (1–2), 59–63. https://doi.org/10.1023/A:1016786023456.

(32) Zhang, G.; Yang, C.; Miller, J. T. Tetrahedral Nickel(II) Phosphosilicate Single-Site Selective Propane Dehydrogenation Catalyst. *ChemCatChem* **2018**, *10* (5), 961–964. https://doi.org/10.1002/cctc.201701815.

(33) Tian, Y.; Etschmann, B.; Liu, W.; Borg, S.; Mei, Y.; Testemale, D.; O'Neill, B.; Rae, N.; Sherman, D. M.; Ngothai, Y.; et al. Speciation of Nickel (II) Chloride Complexes in Hydrothermal Fluids: In Situ XAS Study. *Chem. Geol.* **2012**, *334*, 345–363. https://doi.org/10.1016/j.chemgeo.2012.10.010.

(34) Hoffmann, M. M.; Darab, J. G.; Palmer, B. J.; Fulton, J. L. A Transition in the Ni2+ Complex Structure from Six-to Four-Coordinate upon Formation of Ion Pair Species in Supercritical Water: An X-Ray Absorption Fine Structure, near-Infrared, and Molecular Dynamics Study. *J. Phys. Chem. A* **1999**, *103* (42), 8471–8482. https://doi.org/10.1021/jp990435c.

(35) Albrahim, M.; Thompson, C.; Leshchev, D.; Shrotri, A.; Unocic, R. R.; Hong, J.; Hoffman, A. S.; Meloni, M. J.; Runnebaum, R. C.; Bare, S. R.; et al. Reduction and Agglomeration of Supported

Metal Clusters Induced by High-Flux X-Ray Absorption Spectroscopy Measurements. *J. Phys. Chem. C* **2021**, *125* (20), 11048–11057. https://doi.org/10.1021/acs.jpcc.1c01823.

(36) Frenkel, A. I.; Hills, C. W.; Nuzzo, R. G. A View from the inside: Complexity in the Atomic Scale Ordering of Supported Metal Nanoparticles. *J. Phys. Chem. B* **2001**, *105* (51), 12689–12703. https://doi.org/10.1021/jp012769j.

(37) Jentys, A. Estimation of Mean Size and Shape of Small Metal Particles by EXAFS. *Phys. Chem. Chem. Phys.* **1999**, *1* (17), 4059–4063. https://doi.org/10.1039/a904654b.

(38) Kistler, J. D.; Chotigkrai, N.; Xu, P.; Enderle, B.; Praserthdam, P.; Chen, C. Y.; Browning, N. D.; Gates, B. C. A Single-Site Platinum CO Oxidation Catalyst in Zeolite KLTL: Microscopic and Spectroscopic Determination of the Locations of the Platinum Atoms. *Angew. Chemie - Int. Ed.* **2014**, *53* (34), 8904–8907. https://doi.org/10.1002/anie.201403353.

(39) Ortalan, V.; Uzun, A.; Gates, B. C.; Browning, N. D. Direct Imaging of Single Metal Atoms and Clusters in the Pores of Dealuminated HY Zeolite. *Nat. Nanotechnol.* **2010**, *5* (7), 506–510. https://doi.org/10.1038/nnano.2010.92.

(40) Liu, L.; Lopez-Haro, M.; Calvino, J. J.; Corma, A. Tutorial: Structural Characterization of Isolated Metal Atoms and Subnanometric Metal Clusters in Zeolites. *Nat. Protoc.* **2021**, *16* (4), 1871–1906. https://doi.org/10.1038/s41596-020-0366-9.

(41) Jaegers, N. R.; Khivantsev, K.; Kovarik, L.; Klas, D. W.; Hu, J. Z.; Wang, Y.; Szanyi, J. Catalytic Activation of Ethylene C-H Bonds on Uniform D8 Ir(i) and Ni(Ii) Cations in Zeolites: Toward Molecular Level Understanding of Ethylene Polymerization on Heterogeneous Catalysts. *Catal. Sci. Technol.* **2019**, *9* (23), 6570–6576. https://doi.org/10.1039/c9cy01442j.

(42) Śrebowata, A.; Baran, R.; Łomot, D.; Lisovytskiy, D.; Onfroy, T.; Dzwigaj, S. Remarkable Effect of Postsynthesis Preparation Procedures on Catalytic Properties of Ni-Loaded BEA Zeolites in Hydrodechlorination of 1,2-Dichloroethane. *Appl. Catal. B Environ.* **2014**, *147*, 208–220. https://doi.org/10.1016/j.apcatb.2013.08.040.

(43) Ogino, I.; Gates, B. C. Essentially Molecular Metal Complexes Anchored to Zeolite Beta:

Synthesis and Characterization of Rhodium Complexes and Ruthenium Complexes Prepared from Rh(Acac)(Eta(2)-C2H4)(2) and Cis-Ru(Acac)(2)(Eta(2)-C2H4)(2). *J. Phys. Chem. C* **2010**, *114* (6), 2685–2693.

(44) Lardinois, T. M.; Bates, J. S.; Lippie, H. H.; Russell, C. K.; Miller, J. T.; Meyer, H. M.; Unocic, K. A.; Prikhodko, V.; Wei, X.; Lambert, C. K.; et al. Structural Interconversion between Agglomerated Palladium Domains and Mononuclear Pd(II) Cations in Chabazite Zeolites. *Chem. Mater.* **2021**, *33* (5), 1698–1713. https://doi.org/10.1021/acs.chemmater.0c04465.

(45) Lu, Y.; Kuo, C. Te; Kovarik, L.; Hoffman, A. S.; Boubnov, A.; Driscoll, D. M.; Morris, J. R.; Bare, S. R.; Karim, A. M. A Versatile Approach for Quantification of Surface Site Fractions Using Reaction Kinetics: The Case of CO Oxidation on Supported Ir Single Atoms and Nanoparticles. *J. Catal.* **2019**, *378*, 121–130. https://doi.org/10.1016/j.jcat.2019.08.023.

(46) Penkova, A.; Dzwigaj, S.; Kefirov, W. R.; Hadjiivanov, K.; Che, M. Effect of the Preparation Method on the State of Nickel Ions in BEA Zeolites. A Study by Fourier Transform Infrared Spectroscopy of Adsorbed CO and NO, Temperature-Programmed Reduction, and X-Ray Diffraction. *J. Phys. Chem. C* **2007**, *111* (24), 8623–8631. https://doi.org/10.1021/jp071927p.

Supporting Information

Nano sized metallic nickel clusters stabilized on dealuminated Beta zeolite: a highly active and stable ethylene hydrogenation catalyst

Michael Meloni[1], Jiyun Hong[2], Adam Hoffman[2], Simon R. Bare[2] and Ron C. Runnebaum[1,3,]*

[1]Department of Chemical Engineering, University of California, Davis, CA, 95616, USA
[2]Stanford Synchrotron Radiation Lightsource, SLAC National Accelerator Laboratory, Menlo Park, CA, USA
[3]Department of Viticulture & Enology, University of California, Davis, CA, 95616, USA

Table of Contents

References

Experimental Details.

N_2 Physisorption. Samples, loaded into a capped tube in the glovebox to exclude exposure to moisture and air, were transferred to a Micromeritics 3Flex instrument and degassed at 350°C for 4 h before measurements under dynamic vacuum. Samples were weighed in a glovebox before and after analysis to ensure a dry weight was obtained. N_2 adsorption isotherms were taken at -196°C. BET surface area was determined in the relative pressure range 0.001-0.05. Micropore volume was calculated using the t-plot method using Harkins-Jura thickness equation relating relative pressure to thickness of adsorbed layer.

Ni nanoparticle (Ni NP) on SiO_2

Under nitrogen flow, 257 mg of $Ni(acac)_2$ was mixed with 15 mL oleylamine (OAm) and 0.32 mL oleic acid (OA). The formed solution was heated to 110°C in 20 min, The solution was kept at 110 °C for an hour to remove humidity and oxygen. Next, the solution was cooled down to 90 °C where 264 mg of BTB solvated in 2 mL of OAm quickly injected into the solution. The resultant solution was kept at 90 °C for 60 min. The solution was cooled down to room temperature. 30 mL of ethanol was added, and the product was separated by centrifugation (8000 rpm for 10 min). The product was then dispersed in hexane. TEM image was collected to determine the size of the nanoparticles formed (Figure S4.13a). The concentration of the Ni NPs was determined by thermogravimetric analysis (TGA) to be 2.3 g/l. 1 wt% of Ni was impregnated in silica gel (BET Surface area= 300 m^2/g). The silica was dispersed in ethanol and hexane and the NPs solution was added drop by drop. The mixture was left under stirring for 1 h. The support was collected by centrifugation and the obtained mixture was dried at 70°C for overnight.

DFT of Ni in a silanol nest

To prepare the initial structure, we started with a full BEA unit cell, removed a silicon atom from the T9 crystallographic site, and added hydrogen atoms to cap the oxygen atoms previously bound to the silicon. This produces a silanol nest site with 4 OH groups. Next, a nickel atom was added to the center of the

silanol nest and two hydrogens were removed to prepare the Ni(2+) state. This initial structure was then optimized with VASP quantum chemistry software, using the RPBE functional, at a 520 eV energy cutoff.

Extended Results

XANES

As shown in XANES spectra, the absorption edge of 8342.2 eV for the oxidized Ni-[DeAl]-Beta indicates that the Ni remains in oxidation state of 2+, similar to NiO. However, except for the similar edge position, the oxidized Ni-[DeAl]-Beta displays distinctive XANES features that suggest tetrahedral coordination geometry for Ni centers, rather than the octahedral geometry. First distinguishing feature is the pre-edge peak which arises from the 1s to 3d transition. Compared to NiO that is octahedral in coordination geometry, oxidized Ni-[DeAl]-Beta has the pre-edge peak that is slightly red-shifted by 0.4 eV and is more intense. In contrast to the octahedral geometry that is centrosymmetric, tetrahedral geometry induces d-p orbital mixing and hence increases the probability for dipole-forbidden 1s to 3d transition. This is manifested as more intense pre-edge peaks in tetrahedrally coordinated complexes. The overall energy position for the pre-edge peak also differs between tetrahedral and octahedral complexes, as the ligand field splitting puts the Ni d-orbitals at different energies for the two geometries. For Ni^{2+} in tetrahedral coordination geometry, the t_2 orbitals sit lower in energy than the e_g orbitals do in the octahedral complexes. Our pre-edge data is also consistent with the XANES data of other tetrahedral Ni complexes that are reported elsewhere.[1]

Spectrum collected after reduction shows that there is formation of metallic Ni. In comparison to the oxidized state, the whiteline intensity has decreased, but it still retains the single broad peak rather than the two humps that the metallic Ni has. The pre-edge region of reduced state shows growth in intensity around 8333 eV, which is consistent with the edge position of metallic Ni. The co-existence of single

broad whiteline peak and the growth of intensity at 8333 eV suggests that the reduced state is a mixture of the original oxidized state and metallic Ni.

Linear Combination Analysis (LCF) on XANES

Linear combination fitting (LCF) analysis on the reduced Ni-[DeAl]-Beta was performed with Athena software of Demeter package.[2] The analysis was done within an energy range of -20 eV below to +30 eV above the edge using the oxidized Ni-[DeAl]-Beta and Ni nanoparticle spectra as weighted components. During the fit, the components were constrained to have no E0 shift, and the weights were forced to be between 0 and 1, while not constrained to weight sum of 1.

EXAFS

As shown in the Fourier-transformed EXAFS spectra in Figure S4.7, oxidized Ni-[DeAl]-Beta has much smaller magnitude at 1.5Å than the NiO. This observation is consistent with the smaller coordination number for Ni-O in tetrahedral Ni centers in oxidized Ni-[DeAl]-Beta compared to the octahedral Ni in NiO. The oxidized Ni-[DeAl]-Beta shows the second-shell peak at 2.7Å, which is significantly weaker in magnitude and slightly longer distance than the second shell of NiO at 2.6Å.

The EXAFS of the reduced state of Ni-[DeAl]-Beta is consistent with the XANES in that the metallic Ni has formed after the reduction. The k-space EXAFS of reduced Ni-[DeAl]-Beta above the k of 5 $Å^{-1}$ is dominated by the oscillation that aligns with that of metallic Ni, but at much weaker amplitude, suggesting that the metallic Ni formed is in the form of very small, nanometer-sized particles. The oscillations in the below k of 5 $Å^{-1}$ deviates from the metallic Ni but shows some alignment with the as-prepared Ni-[DeAl]-Beta, consistent with the XANES interpretation that the reduced Ni-[DeAl]-Beta is a mixture of the as-prepared state and the metallic Ni nanoparticles. The Fourier-transform of EXAFS also shows that reduced Ni-[DeAl]-Beta resembles the spectrum of Ni nanoparticles, but at much weaker magnitudes, and has a small shoulder at R = 1.5Å (phase uncorrected) that overlaps with the first shell of oxidized Ni-[DeAl]-Beta. The wavelet transform analysis, Figure S4.14, on reduced Ni-[DeAl]-Beta also

supports the mixture of oxidized and reduced Ni. The plot of reduced Ni-[DeAl]-Beta (Figure S4.14b) has weak intensities at around R ≈ 1.5Å and k ≈ 4 $Å^{-1}$ and R ≈ 2.5Å and k ≈ 5-6 $Å^{-1}$, which align with the first and second shell of oxidized Ni-[DeAl]-Beta, respectively, in addition to the features representing metallic Ni (Figure S4.14c).

Calculation of nanoparticle cluster size based on coordination numbers from EXAFS

The CN values of the first to fourth Ni-Ni scattering paths were correlated with cluster diameter[3] to determine that the Ni nanoparticles formed in the reduced Ni-[DeAl]-Beta are about 1 nm. The CN values from the EXAFS fit of reduced Ni-[DeAl]-Beta was compared to the average CN values calculated for the fcc nanoparticle of perfect spherical shape. The best overlap for the CN values, together with their error bars, indicated 1 to 1.3 nm sized clusters for the Ni-[DeAl]-Beta.

Additional calculation was carried out to determine the number of atoms in a particle that would represent the coordination numbers extracted from the EXAFS fitting.[4] The formula and the parameters from Andreas Jentys[4] was used. The calculation indicates that the CN values for the EXAFS fit correspond to a particle with number of atoms ranging from 40-100. The metallic Ni particles of fcc crystal structure that consist of 40-100 atoms have cluster radii ranging from 4.7 – 6.4 Å, which correspond to about 0.9 – 1.3 nm size particles. See below for the details of calculations.

The unit cell of nickel is fcc (which has 4 atoms in a unit cell) with the lattice parameter of 3.52 Å (unit cell volume of $43.6Å^3$).[5] This information can be used to determine the radius of a cluster based on the following equation:

$$N_{unit\ cell} = {\frac{4}{3}\pi r^3}\Big/{V_{unit\ cell}}$$

$N_{unit\ cell}$ = Number of unit cells in a cluster

$V_{unit\ cell}$= Volume of a unit cell

r = radius of cluster

Number of atoms	Number of unit cells	Radius of cluster (Å)	Cluster diameter (nm)
40	10	4.7	0.9
80	20	5.9	1.2
100	25	6.4	1.3

NO Adsorption

In addition to CO adsorption, NO adsorption was performed on the oxidized Ni-Beta catalysts to probe the Ni sites without reduction (NO also quickly oxidized reduced Ni sites).[6] Figure S4.15 shows FTIR spectra after NO adsorption at room temperature, with band assignments in Table S4.1, that confirms the presence of Ni^{2+} extraframework cations due to framework Al and Ni occupying silanol nests in Ni-[Al]-Beta-19 and Ni-[DeAl]-Beta, respectively.[6] The NO adsorption spectrum of Ni-[Al]-Beta-150 contains bands from both Ni-[Al]-Beta-19 and Ni-[DeAl]-Beta indicating a mixture of Ni sites, extraframework and silanol nests, but with an additional band at 1904 cm^{-1} which is assigned to a Ni^{2+}-NO complex of Ni^{2+} associated with framework Al that is different from the 1896 cm^{-1} band.[7]

Table S4.1. BET surface area and micropore volume from N_2 physisorption isotherms.

Material	BET SA [m^2/g]	Micropore Vol [cm^3/g]	External SA [m^2/g]
H-[Al]-Beta-19	690	0.20	170
Ni-[Al]-Beta-19	690	0.20	180
H-[Al]-Beta-150	550	0.14	200
Ni-[Al]-Beta-150	570	0.15	190
[DeAl]-Beta	600	0.17	160
Ni-[DeAl]-Beta	630	0.19	150

Table S4.2. Summary of bands seen with CO adsorption of materials reduced at 300°C in CO. NO bands are summarized as well of NO adsorbed onto oxidized materials. $^{a}Ni^{2+}$ in extraframework cation exchange positions $^{b}Ni^{2+}$ reoccupying silanol nests

Material	$^{a}Ni^{2+}$-CO	$^{b}Ni^{2+}$-CO	$^{a}Ni^{+}$-$(CO)_x$	$^{b}Ni^{+}$-$(CO)_x$	$^{a}Ni^{2+}$-NO	$^{b}Ni^{2+}$-NO
Ni-[Al]-Beta-19	2212	-	2139, 2112, 2095	2095	1896	-
Ni-[DeAl]-Beta	-	2197	-	2137, 2122, 2076, 2090	-	1879, 1840
Ni-[Al]-Beta-150	-	2201	2138, 2113	2095, 2089	1909, 1896	1879, 1840

Table S4.3. The EXAFS fitting parameters for oxidized Ni-[DeAl]-Beta.

Path	*CN* [a]	*R* [b] (Å)	σ^2 [c] (10^3 Å^2)	ΔE_0 [d] (eV)	R-factor (%)	Reduced χ^2
Using one set of Ni-O distance						
Ni-O	5.3 ± 0.9	1.99 ± 0.01	13.1 ± 10.2	1.5 ± 1.3	0.6	109
Ni-Si	3.0 ± 1.1	3.17 ± 0.02	9.3 ± 4.4	1.5 ± 1.3		
Using two sets of Ni-O distances						
$Ni-O_1$	1.8 ± 0.7	1.91 ± 0.04	1.8 ± 8.9	1.4 ± 2.6	0.4	219
$Ni-O_2$	2.3 ± 1.2	2.06 ± 0.04	1.8 ± 8.9	1.4 ± 2.6		
Ni-Si	3.3 ± 1.7	3.17 ± 0.03	10.0 ± 6.2	1.4 ± 2.6		

[a] Coordination number. [b] Interatomic distance. [c] Mean square disorder. [d] Energy-shift in the fitting.
The S_0^2 value was fixed to 0.87, which was obtained from fitting Ni foil.
The k-range used for the fits: 1.0 – 3.7 Å^{-1}
The R-range used for the fits: 3.6 – 9.5 Å

Table S4.4. The EXAFS fitting parameters for reduced Ni-[DeAl]-Beta.

Fraction	*Path*	*CN* [a]	*R* [b] (Å)	σ^2 [c] (10^3 Å^2)	ΔE_0 [d] (eV)	R-factor (%)	Reduced χ^2
0.51 ± 0.01	Ni-O	4.3 ± 0.8	1.97 ± 0.01	5.9 ± 2.2	-4.6 ± 0.0	0.9	14.03
	Ni-Si	0.6 ± 0.9	3.08 ± 0.04	1.1 ± 12			
0.49 ± 0.00	$Ni-Ni_1$	8.4	2.47	7.7	-4.0 ± 0.5		
	$Ni-Ni_2$	1.7	3.43	4.3			
	$Ni-Ni_3$	9.5	4.30	7.4			
	$Ni-Ni_4$	3.7	5.15	1.0			

[a] Coordination number. [b] Interatomic distance. [c] Mean square disorder . [d] Energy-shift in the fitting.
The CN, R, and σ^2 parameters for Ni-Ni scattering paths are fixed to the values from the EXAFS fitting of extracted (50% AP) data. The CN values are multiplied by fraction in the fit.
The S_0^2 value was fixed to 0.87, which was obtained from fitting Ni foil.
The k-range used for the fit: 2.9 – 9.8 Å^{-1}
The R-range used for the fit: 1.0 – 5.5 Å

Table S4.5. The EXAFS fitting parameters for extracted (50% oxidized) state.

Path	*CN* [a]	*R* [b] (Å)	σ^2 [c] (10^3 Å^2)	ΔE_0 [d] (eV)	R-factor (%)	Reduced χ^2
Ni-Ni$_1$	8.4 ± 1.2	2.47 ± 0.01	7.7 ± 1.3			
Ni-Ni$_2$	1.7 ± 2.2	3.43 ± 0.03	4.3 ± 11.9			
Ni-Ni$_3$	9.5 ± 6.0	4.30 ± 0.01	7.4 ± 5.5	-4.0 ± 1.4	1.3	42.6
Ni-Ni$_4$	3.7 ± 5.2	5.15 ± 0.03	1.0 ± 9.9			

[a] Coordination number. [b] Interatomic distance. [c] Mean square disorder . [d] Energy-shift in the fitting.
The S_0^2 value was fixed to 0.87, which was obtained from fitting Ni foil.
The k-range used for the fit: 2.9 – 10.4 Å^{-1}
The R-range used for the fit: 1.4 – 5.5 Å

Table S4.6. LCF analysis of Ni-[DeAl]-Beta after reduction at 300°C in 10% H_2. The analysis shows that approximately 50% of the Ni sites are reduced to metallic Ni. R-factor: 4.51 x10^{-4}, Reduced chi-square: 8.45 x 10^{-5}.

Standard	Weight
NiNP	0.557 (0.004)
Ni-[DeAl]-Beta-O	0.434 (0.004)
Sum: 0.991	

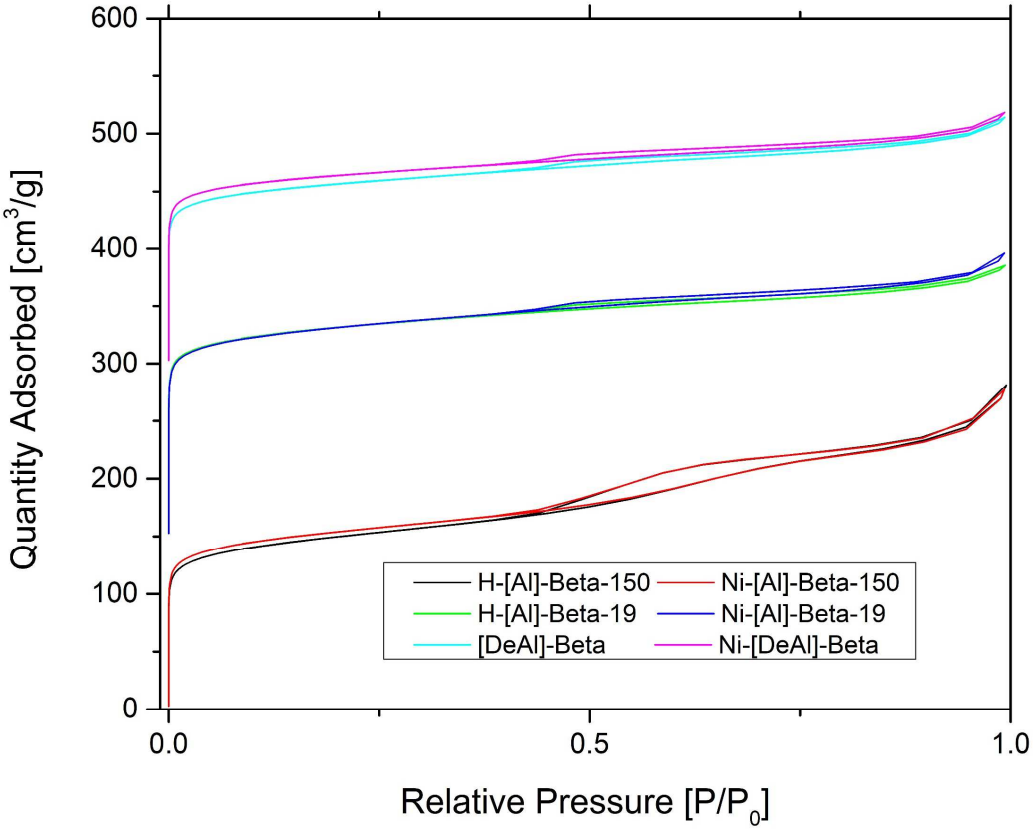

Figure S4.1. N_2 physisorption isotherms for all Beta catalysts. The isotherms show no significant change to the zeolite structure after Ni deposition.

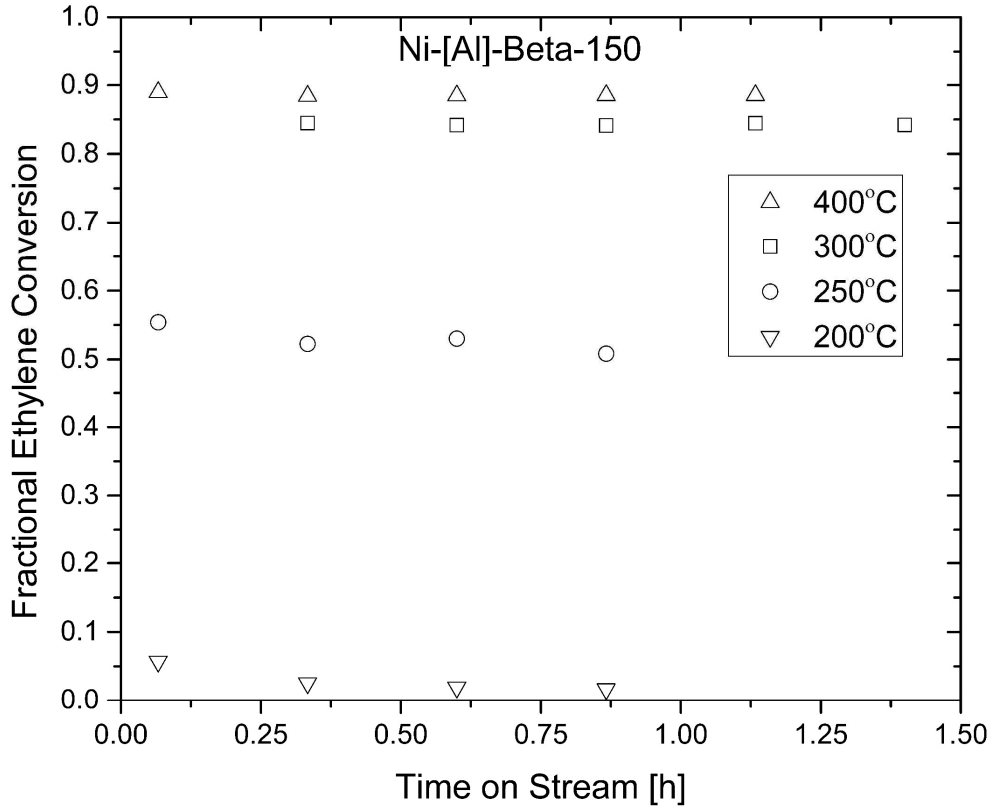

Figure S4.2. Ni-[Al]-Beta-150 activated at different temperatures between 200-400°C for 2 h in 10% H_2. All experiments run at the same W/F. Conversion increases by 1.6-fold when increasing activation temperature from 250°C to 300°C, and by 1.1-fold when increasing temperature from 300°C to 400°C.

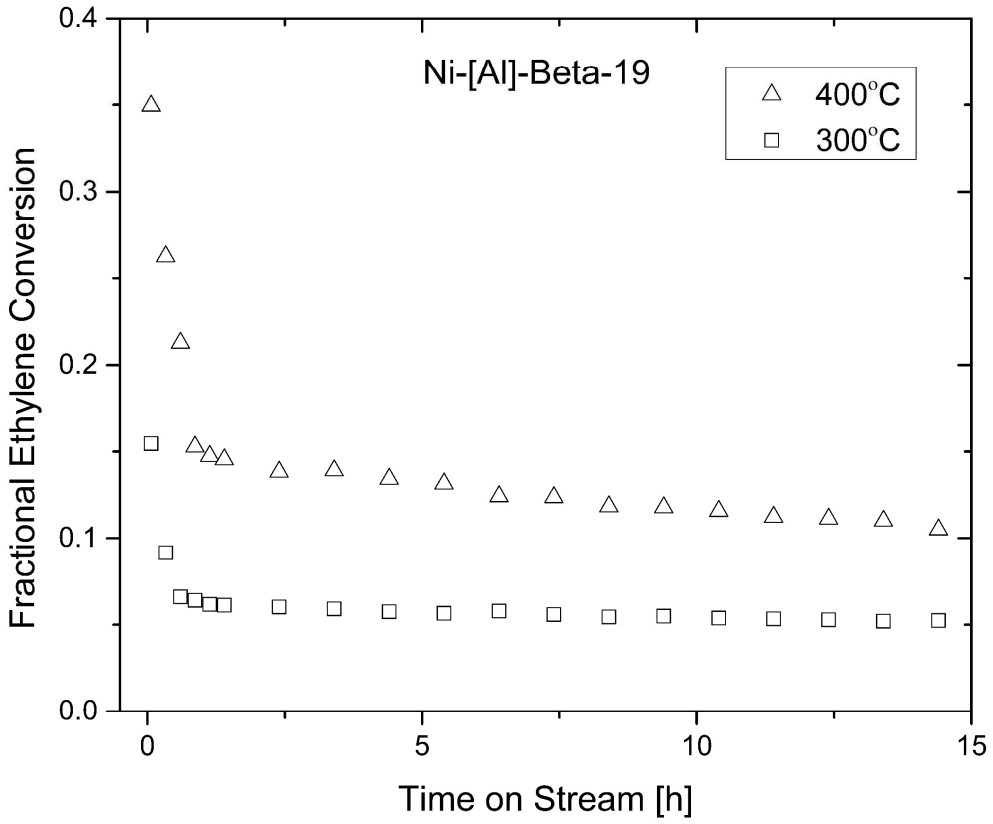

Figure S4.3. The effect of activation temperature on C_2H_4 hydrogenation of Ni-[Al]-Beta-19. Samples were activated at 400°C and 300°C in 10% H_2 for 2 hours and were run at the same W/F. Conversion increases by an average of 2.3-fold by increasing activation temperature from 300°C to 400°C.

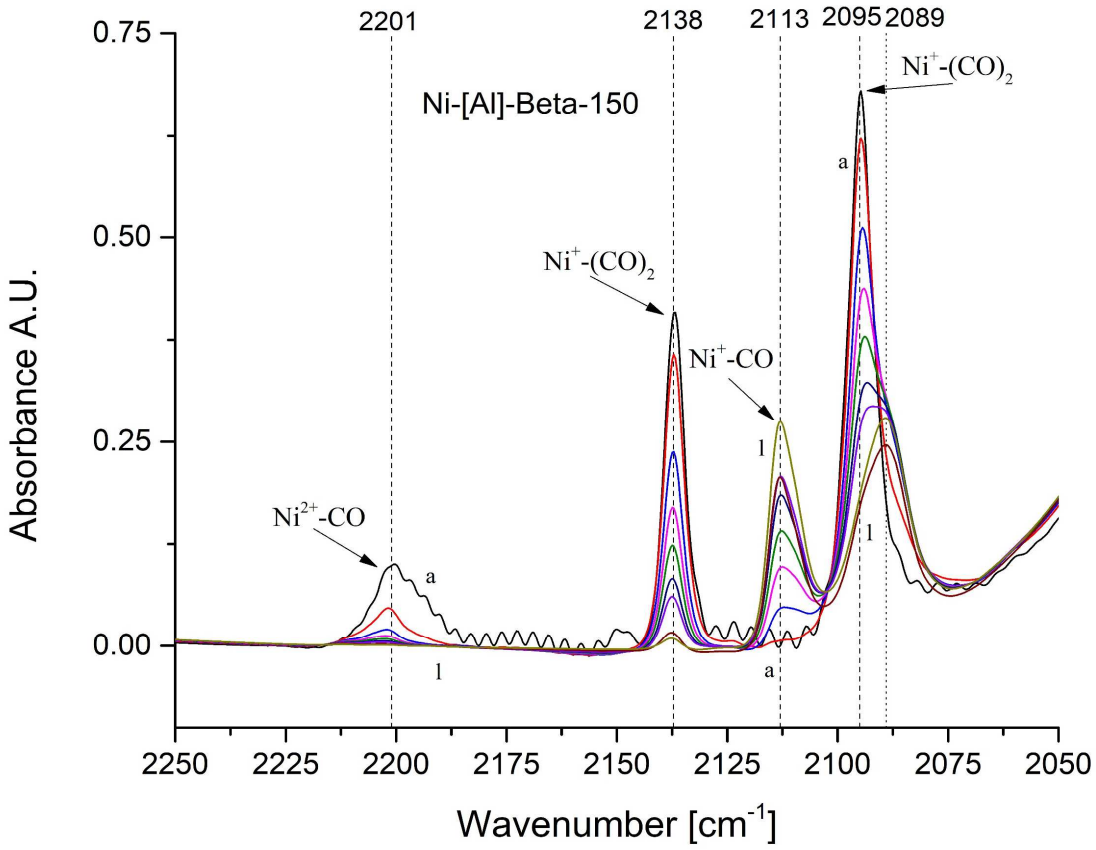

Figure S4.4. CO adsorption at room temperature of Ni-[Al]-Beta-150. Sample was previously reduced at 300°C for 15 min in 10% CO. Spectra taken (a-l) as gas phase CO was purged with He. Spectra indicate of mixture of Ni in silanol nests and extraframework cation exchange positions.

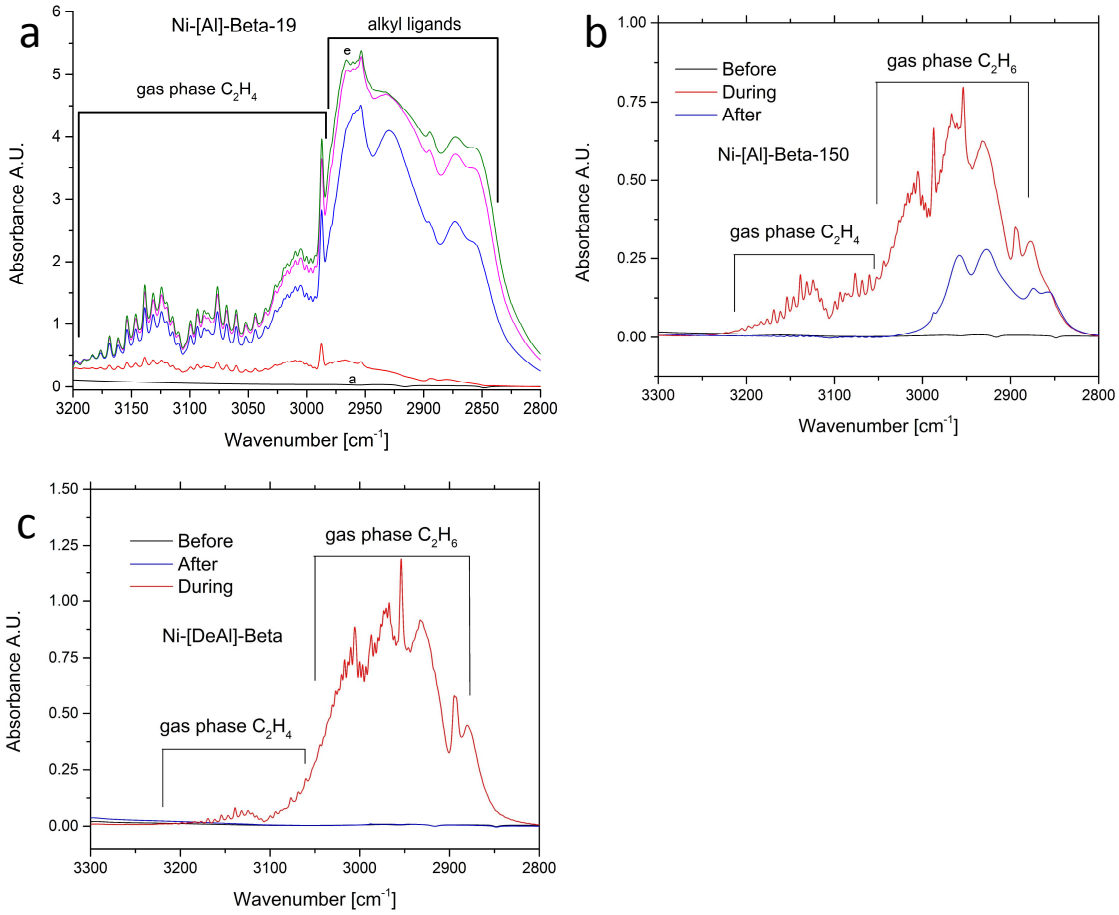

Figure S4.5. a) *In-situ* FTIR of Ni-[Al]-Beta-19 during C_2H_4 hydrogenation (1:2:3 C_2H_4:H_2:He, at 100°C) after activation in 10% H_2 at 300°C. Spectra start with the introduction of reaction gases at spectrum a) Spectra show a large increase in adsorbed alkyl species on Ni-[Al]-Beta-19 during reaction. b) Before, during, and after C_2H_4 hydrogenation with Ni-[Al]-Beta-150. Spectra show adsorbed alkyl ligands after hydrogenation. c) Before, during, and after C_2H_4 hydrogenation with Ni-[DeAl]-Beta. Spectra show no adsorbed alkyl ligands after hydrogenation.

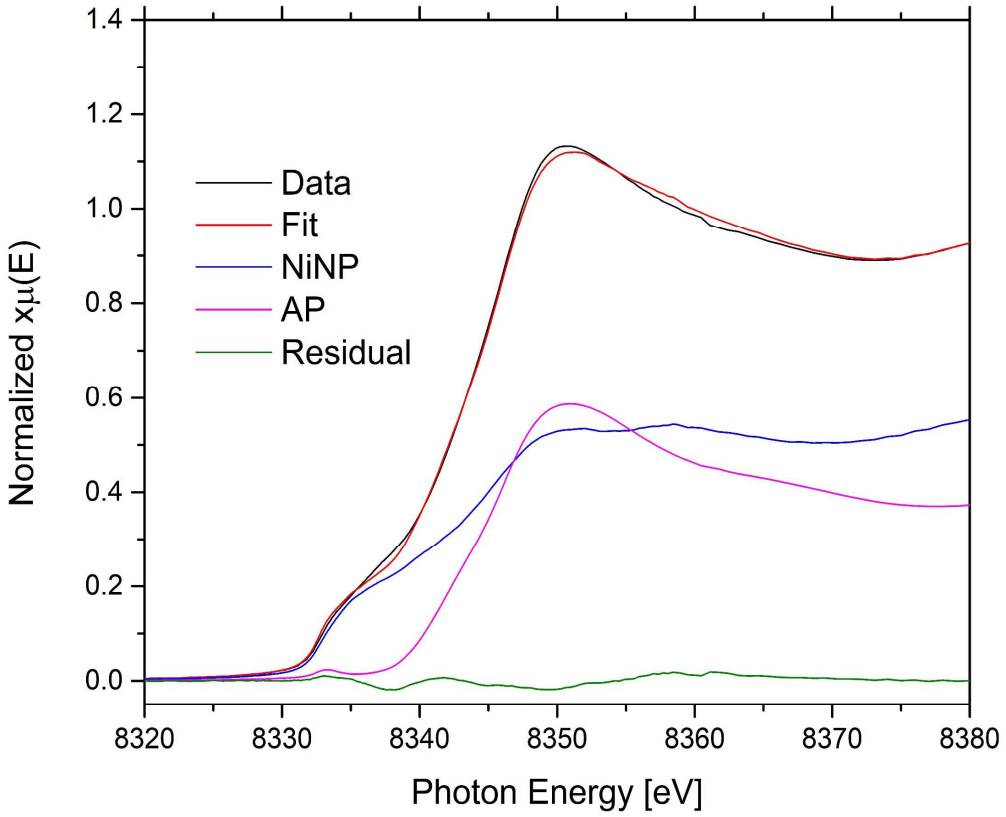

Figure S4.6. LCF of the reduced state of Ni after 300°C reduction, results of analysis in Table S4.6. The analysis shows that approximately 50% (Table S6) of the Ni in the spectra can be represented by metallic Ni nanoparticles.

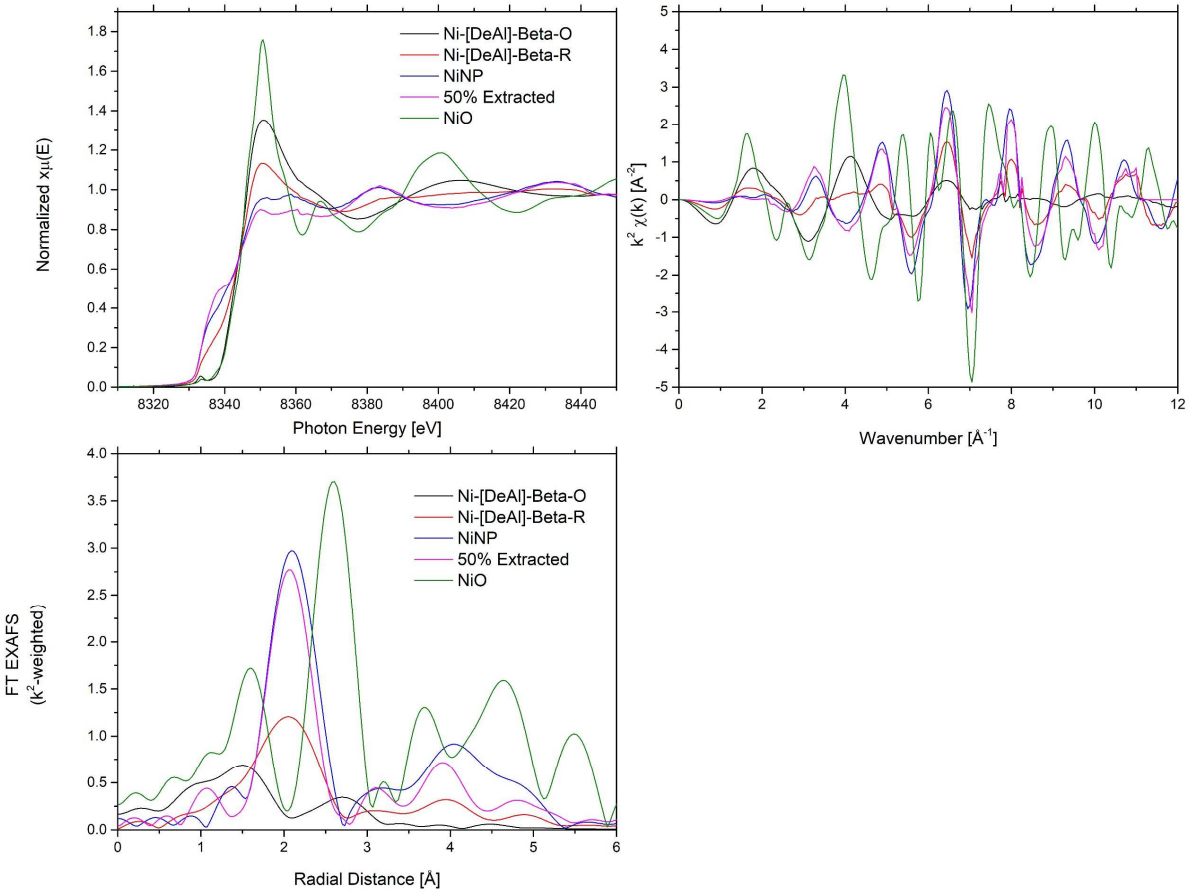

Figure S4.7. XANES and EXAFS constructed spectrum representing the reduced fraction of Ni-[DeAl]-Beta (50% Extracted) as well as both oxidized and reduced Ni-[DeAl]-Beta. The reconstructed spectrum resembles the NiNP but with smaller oscillations throughout k-space.

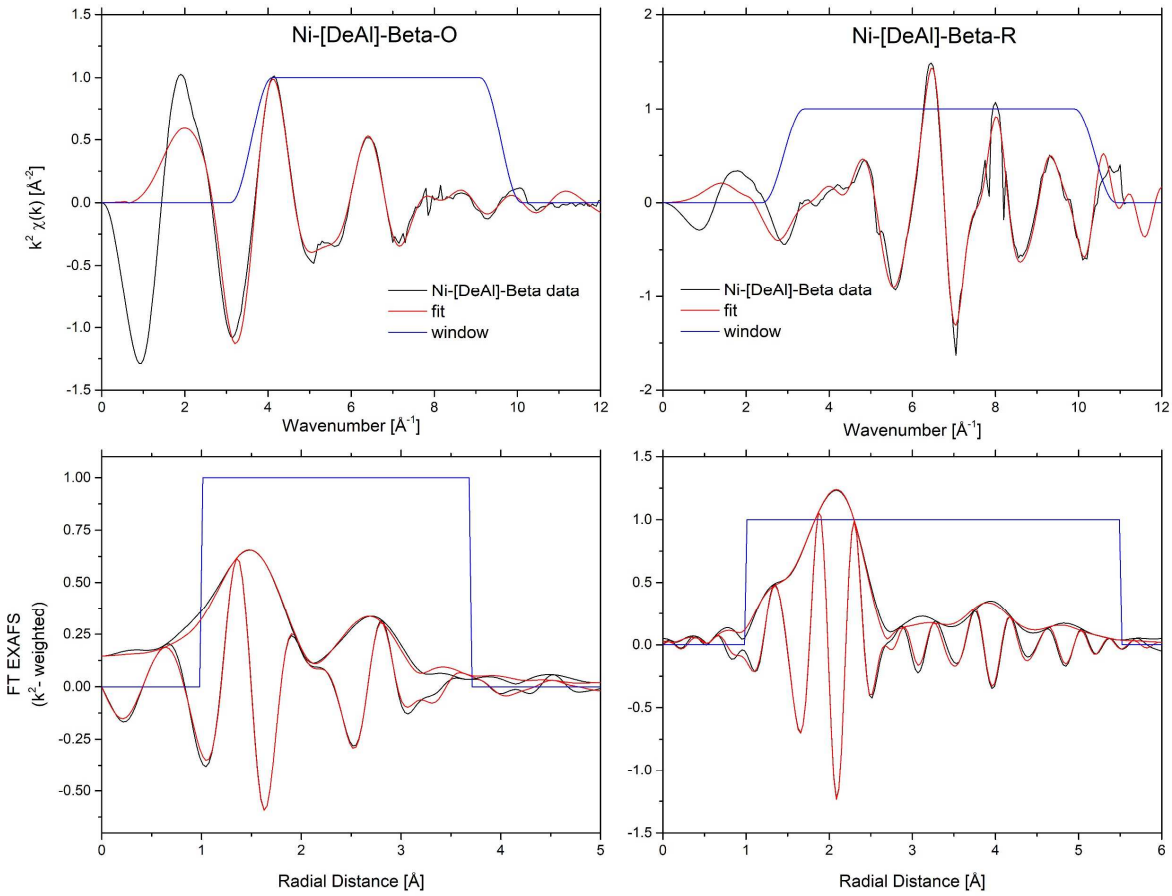

Figure S4.8. EXAFS spectra of Ni-[DeAl]-Beta after oxidation (left) and after reduction (right) at 300°C in 10% H_2. Data is in black while the fits are shown in red and the fitting window is in blue.

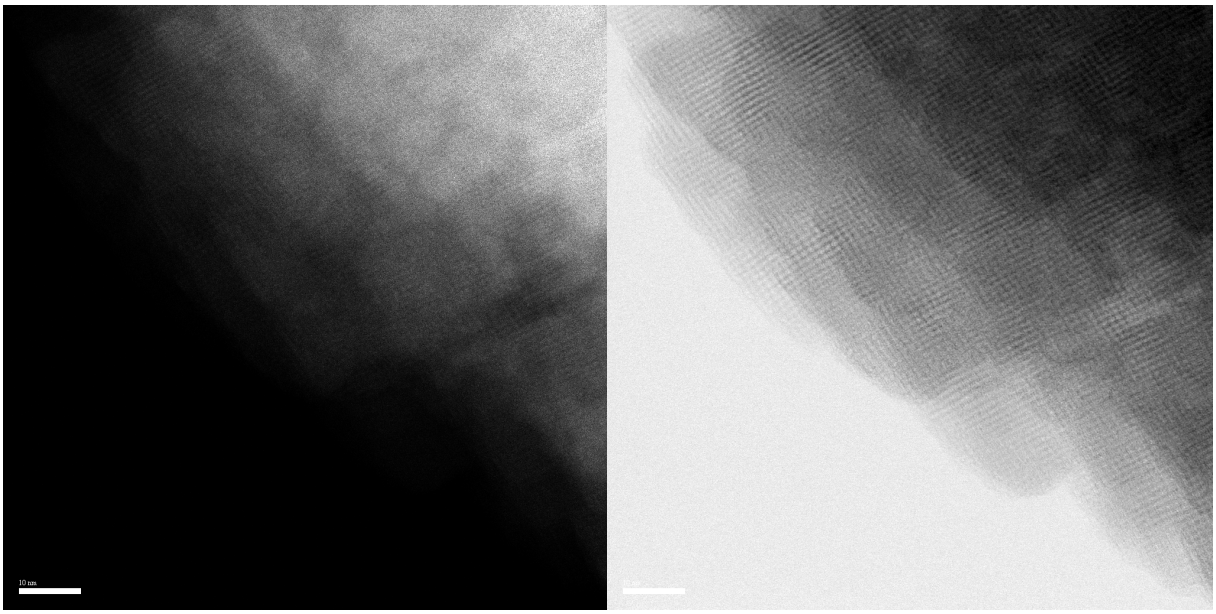

Figure S4.9. Representative image of Ni-[DeAl]-Beta with dark-field (left) and bright-field (right) images taken after reduction of the sample at 300°C in 10% H_2 for 2 hours. The images show no evidence of NiO nanoparticles.

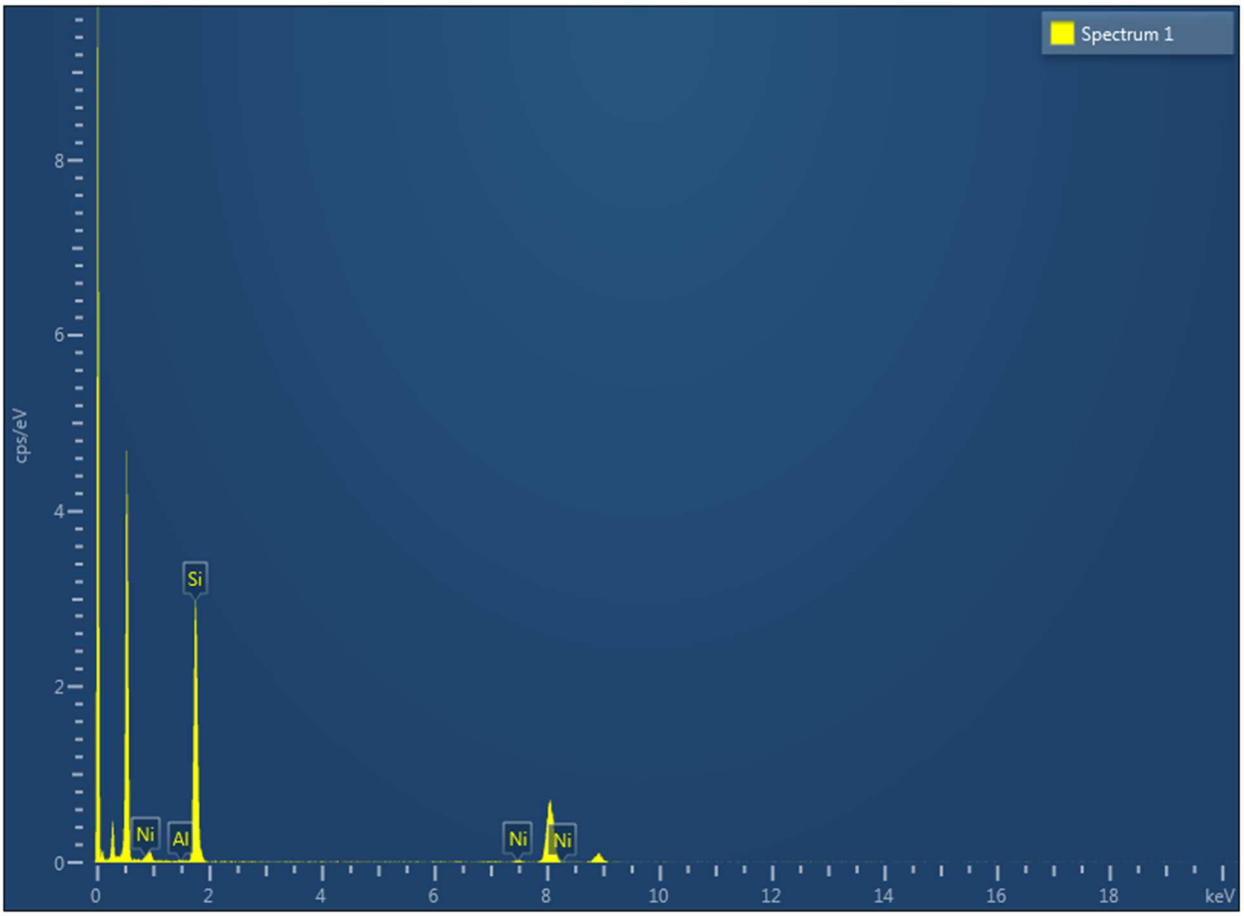

Figure S4.10. EDS spectrum of Ni-[DeAl]-Beta oxidized sample. Spectrum confirms the presence of Ni as well as the absence of Al.

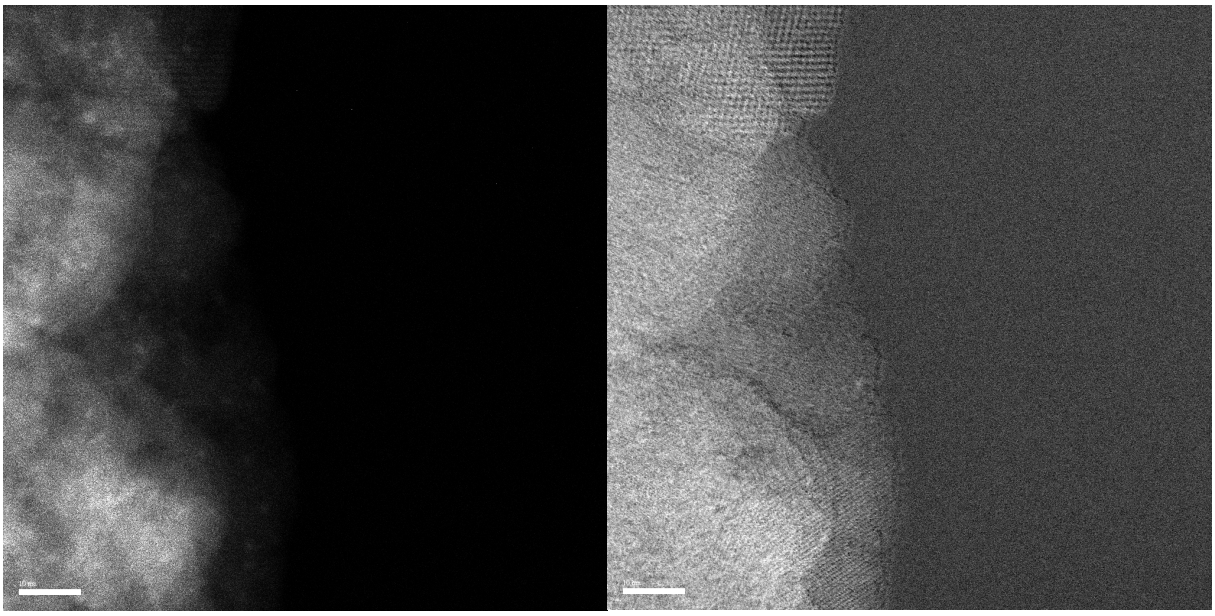

Figure S4.11. Reference dark field image taken of 2.7wt% Ni dispersed on [Al]-Beta-150. Image was taken to validate imaging of nano-sized NiO clusters on a zeolite.

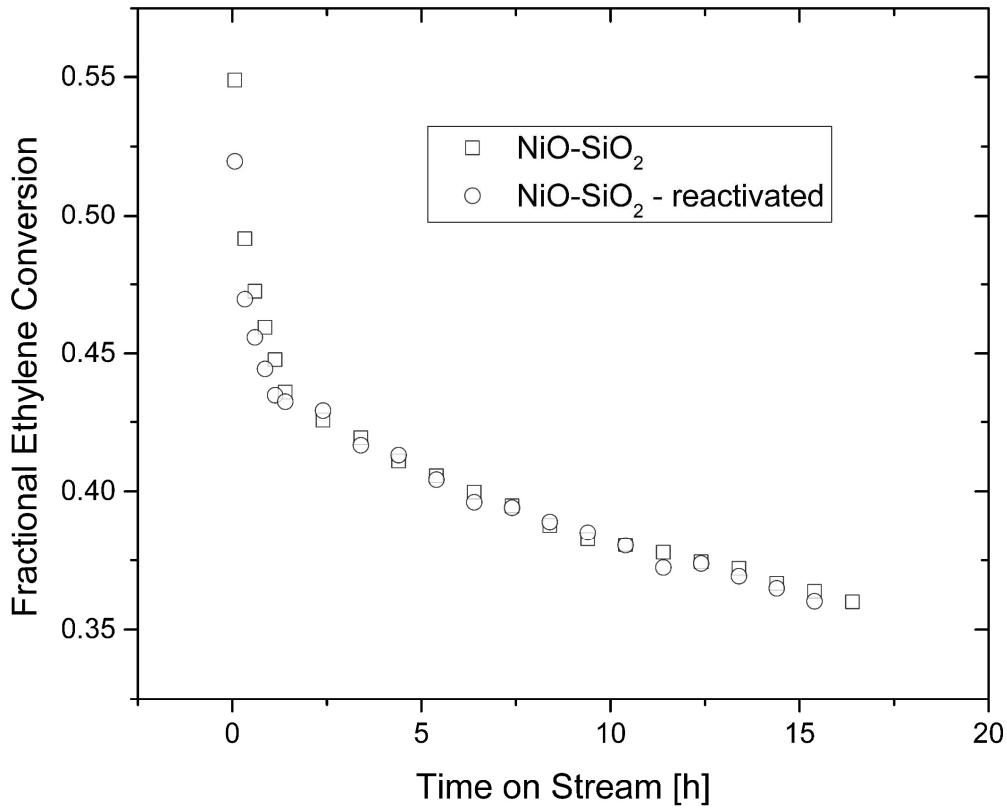

Figure S4.12. Reactivation of $NiO\text{-}SiO_2$ (aq) catalyst. Catalysis shows identical activity after reactivation with the same pretreatment conditions (10% H_2, 300°C for 2 h).

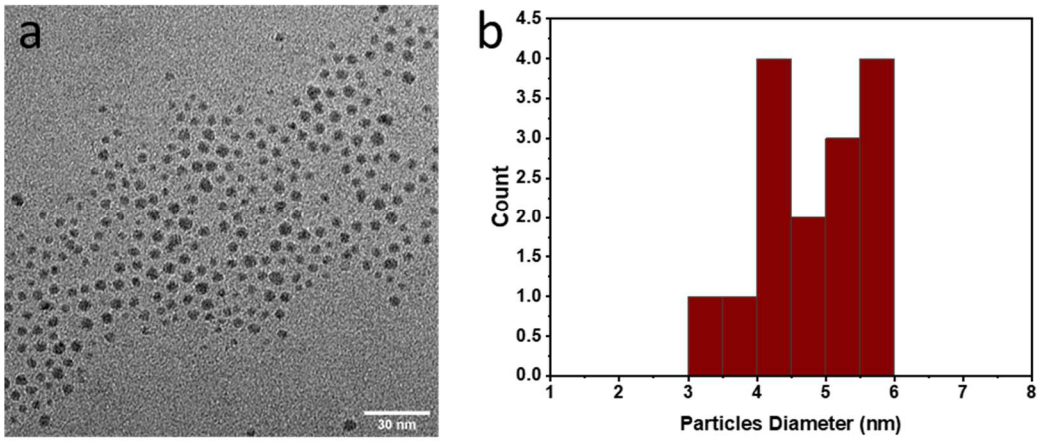

Figure S4.13. (a) TEM images of the synthesized Ni NP supported on SiO_2. (b) Size distribution of Ni NP.

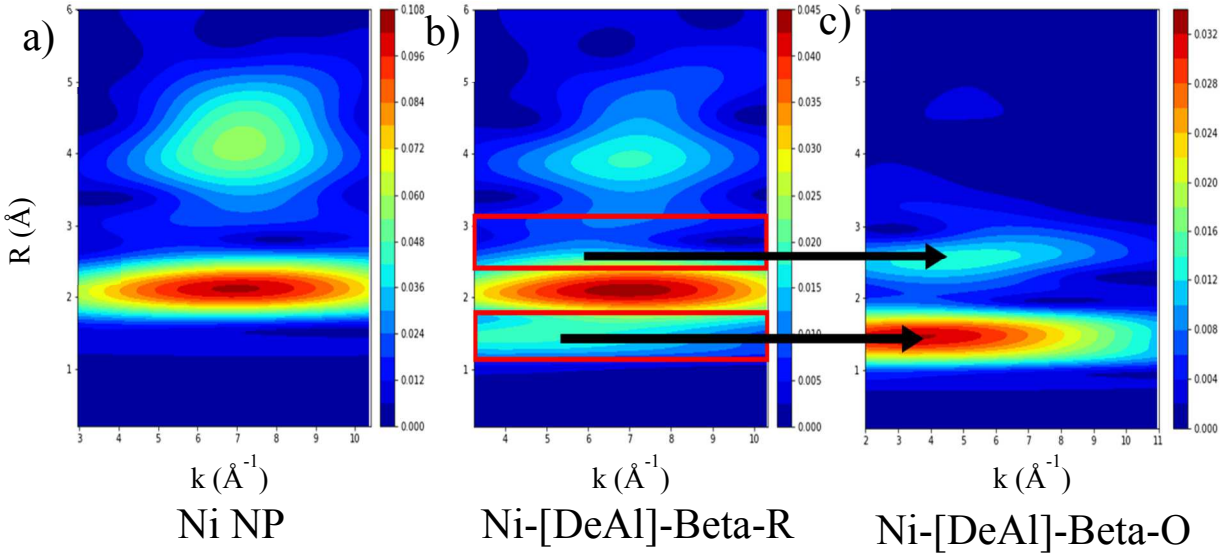

Figure S4.14. (a) Wavelet analysis of Ni NP, (b) reduced Ni-[DeAl]-Beta (b, 300°C 10% H_2), and (c) oxidized Ni-[DeAl]-Beta. The analysis qualitatively shows that reduced Ni-[DeAl]-Beta has features of both Ni NP and Ni-[DeAl]-Beta-O, suggesting that there is a mixture of reduced and oxidized Ni sites.

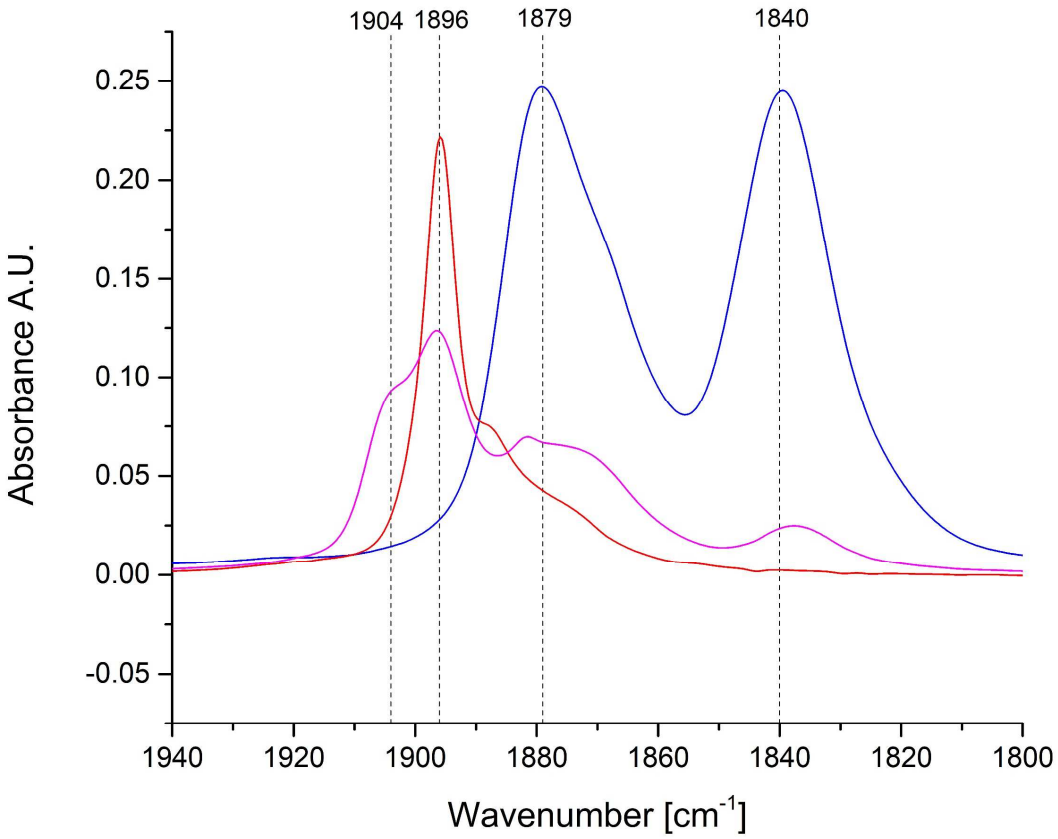

Figure S4.15. NO adsorption at room temperature onto oxidized catalysts. NO was briefly pulsed (1%NO 99% N_2) and then spectra were taken. Ni-[Al]-Beta-19 (red) and Ni-[DeAl]-Beta (blue) show bands due to extraframework cation exchange Ni and Ni reoccupying silanol nests respectively. The Ni-[Al]-Beta-150 (purple) spectrum indicates a mixture of extraframework Ni cations as well as Ni reoccupying silanol nests.

References

(1) Zhang, G.; Yang, C.; Miller, J. T. Tetrahedral Nickel(II) Phosphosilicate Single-Site Selective Propane Dehydrogenation Catalyst. *ChemCatChem* **2018**, *10* (5), 961–964. https://doi.org/10.1002/cctc.201701815.

(2) Ravel, B.; Newville, M. ATHENA, ARTEMIS, HEPHAESTUS: Data Analysis for X-Ray Absorption Spectroscopy Using IFEFFIT. *J. Synchrotron Radiat.* **2005**, *12* (4), 537–541. https://doi.org/10.1107/S0909049505012719.

(3) Frenkel, A. I.; Hills, C. W.; Nuzzo, R. G. A View from the inside: Complexity in the Atomic Scale Ordering of Supported Metal Nanoparticles. *J. Phys. Chem. B* **2001**, *105* (51), 12689–12703. https://doi.org/10.1021/jp012769j.

(4) Jentys, A. Estimation of Mean Size and Shape of Small Metal Particles by EXAFS. *Phys. Chem. Chem. Phys.* **1999**, *1* (17), 4059–4063. https://doi.org/10.1039/a904654b.

(5) Klaus Hermann. Crystallography and Surface Structure: An Introduction for Surface Scientists and Nanoscientists. John Wiley & Sons 2017. https://doi.org/10.1002/9783527697137.

(6) Mihaylov, M.; Hadjiivanov, K. FTIR Study of CO and NO Adsorption and Coadsorption on Ni-ZSM-5 and Ni/SiO2. *Langmuir* **2002**, *18* (11), 4376–4383. https://doi.org/10.1021/la015739g.

(7) Góra-Marek, K.; Glanowska, A.; Datka, J. Quantitative IR Studies of the Concentration of Different Nickel Sites in NiZSM-5 Zeolites. *Microporous Mesoporous Mater.* **2012**, *158*, 162–169. https://doi.org/10.1016/j.micromeso.2012.03.027.

Chapter 5

Re-dispersion of metallic of nanometallic Ni clusters on Ni-[DeAl]-Beta

Initial proof of concept experiment with suggested future steps

5.1 Abstract

The following is a rough set of initial experiments that look to show how metallic Ni clusters formed on Ni-[DeAl]-Beta may be redispersed atomically by oxidation. It was observed that after reduction of Ni-[DeAl]-Beta (300°C 10% H_2, leads to the formation nanometallic Ni clusters of 0.9 – 1.2 nm, see Chapter 4) that the metallic Ni nanoparticles. When the reduced sample was exposed to ambient air the clusters appear to re-oxidize as indicated by a color change of the sample from grey/black to white, this is not observed on a reference material NiO-SiO_2. The same color change took place after reduction at 400°C, which indicates even larger nanoparticles may be able to be oxidized. Calcination of the air exposed sample followed by CO adsorption leads to a large Ni^{2+} monocarbonyl band, indicating it is likely a significant portion of the Ni has re-dispersed from nanoparticles to atomically reoccupying silanol nests. The results are promising but need a more systematic set of experiments to be publishable, a set of next steps and future experiments are suggested.

5.2 Experimental Methods

Sample Synthesis. Dealuminated Beta ([DeAl]-Beta) was synthesized by heating NH_4-[Al]-Beta (Zeolyst, CP814C) to 80°C in 13M nitric acid for 16 h. Afterwards, the zeolite was washed then dried at 120°C before calcination at 600°C in 10% O_2 for 6 h with ramp rate 2°C/min and a 1 h hold at 120°C. [DeAl]-Beta was transferred from calcination to an argon filled glovebox without exposure to air. Calcined Beta zeolites were mixed with $Ni(acac)_2$ (acac= acetylacetonate; STREM chemical min 95%) and n-pentane in a Schlenk flask such that the Ni loading was 1wt% (±0.02%, exact Ni loading was calculated for each sample). The solution was stirred for 24 h and then the solvent was evacuated for 24 h. The Ni loaded zeolite was then calcined in 10% O_2 at 600°C for 6 h, ramp rate of 2°C/min with a 1 h hold at 120°C, and then stored in an argon glovebox. Reduction of Ni-[DeAl]-Beta was done by loading a calcined sample in a glovebox and transferring, without exposure to air, to a three-zone heated reactor. The sample was heated at 2°C/min to the reduction temperature (300°C or 400°C) and held for 2 h in 10% H_2 (Praxair, 99.999%) 90% N_2 (Praxair, 99.999%).

5.3 Results and Discussion

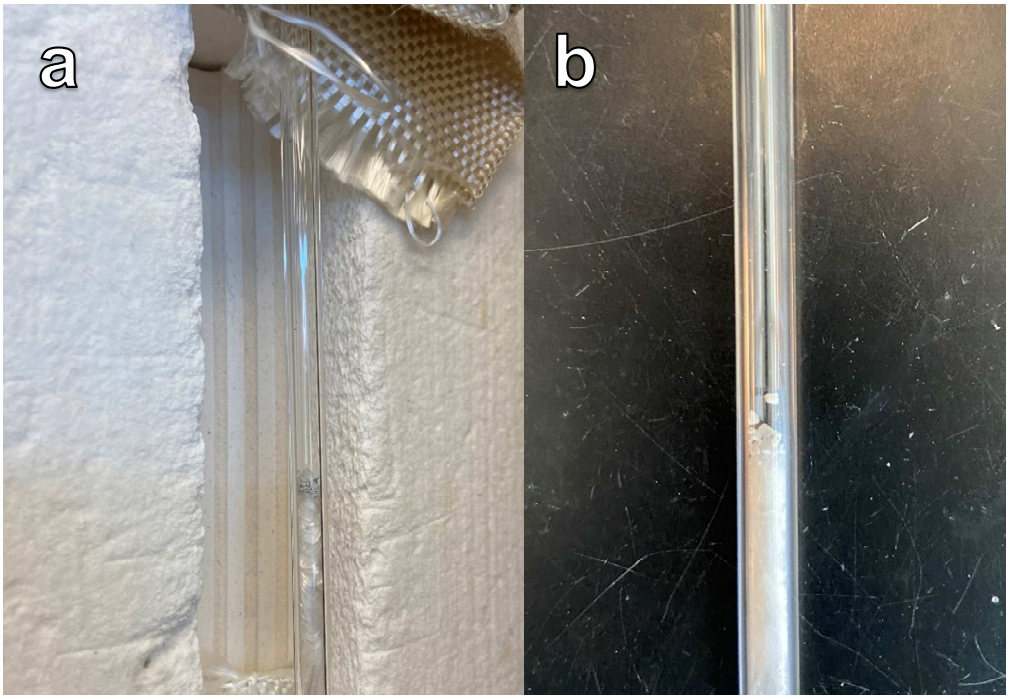

Figure 5.1. a) Ni-[DeAl]-Beta in reactor after reduction at 300°C in 10% H_2 for 2 h. b) The same sample after 2 days of exposure to ambient air.

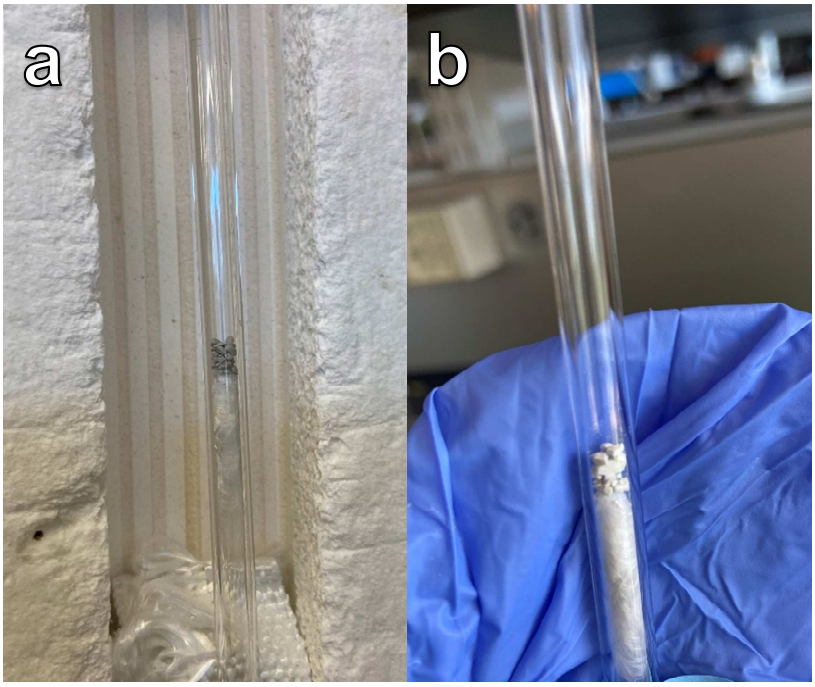

Figure 5.2. a) Ni-[DeAl]-Beta in reactor after reduction at 400°C in 10% H_2 for 2 h. b) The same sample after 4 days of exposure to ambient air.

Figures 5.1 and 5.2 show Ni-[DeAl]-Beta samples after reduction and then subsequent air exposure. The color change is likely an indication of reoxidation of the Ni sites, which happens over the course of a few days at ambient conditions. This behavior was not observed after reduction of a reference material NiO dispersed onto amorphous SiO_2. One explanation for this could be the difference in metallic Ni particle size, the metallic Ni particles on reduced Ni-[DeAl]-Beta are a maximum of 1 nm while particle size of metallic Ni nanoparticles on SiO_2 are likely significantly larger.

The relative amount of Ni^{2+} was probed using CO adsorption at room temperature on Ni-[DeAl]-Beta after reduction (300°C 10% H_2) then reoxidation (600°C 10% O_2). In Figure 5.3, this spectrum is compared to a previously taken spectrum of Ni-[DeAl]-Beta after just oxidation treatment (referred to as as-prepared, AP). The Ni^{2+} monocarbonyl band is larger on the reoxidized sample than the AP sample. This suggests the amount of Ni^{2+} is similar between the two materials even though one had gone through a reductive treatment to form a significant amount of metallic Ni. However, there are some limitations to interpretation of the spectra. The FTIR in-situ pretreatment was not the same (AP was dried at 300°C in N_2) which could result in different in amount of Ni^{2+} monocarbonyls because even residual moisture will reduce CO binding. Another factor that the partial pressure of CO between the two samples is likely different, this will affect the peak height of the Ni^{2+} monocarbonyl band. Even with these limitations it is still likely that the Ni nanoparticles are able to be re-dispersed into silanol nests after reduction and agglomeration, but more systemic experiments are needed.

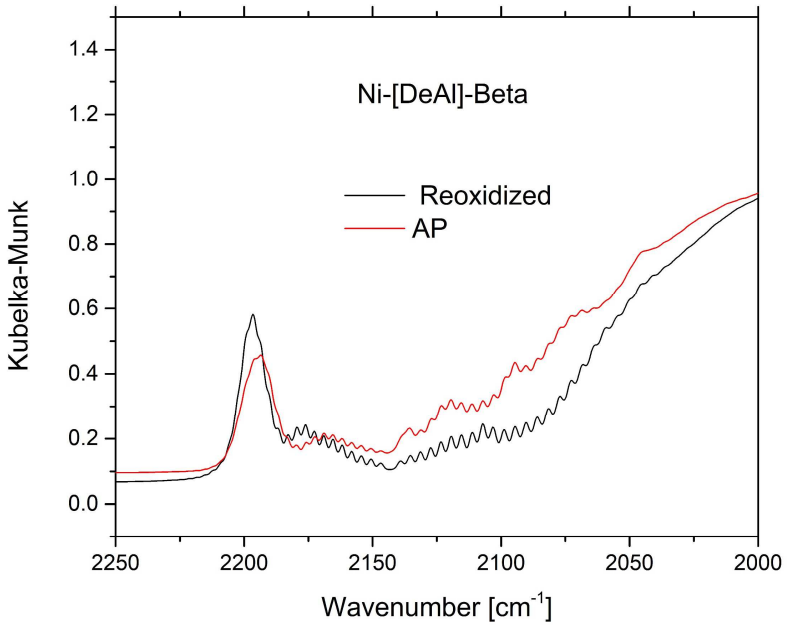

Figure 5.3. CO adsorption onto Ni-[DeAl]-Beta with no reductive treatment (AP, red) and Ni-[DeAl]-Beta after reduction (Reoxidized, black) at 300°C 10% H_2, and then re-oxidation at 600°C in 10% O_2. The Ni^{2+} monocarbonyl band at 2197 cm^{-1} is at a similar magnitude between the two samples, suggesting a similar amount of Ni^{2+} in silanol nests.

5.4 Suggested Future Steps

A more definitive experiment to be used as a proof of concept with CO (or NO) adsorption is suggested as a starting point. The limitations stated in the previous section make it difficult to draw strong conclusions from the spectra. Either the same sample should be used with all gas treatments done in-situ in the FTIR cell (i.e. Figure 5.3 recreated with a single sample *in-situ*) or one synthesis batch of Ni-[DeAl]-Beta should be used for both the AP state (after only oxidation) and reoxidized spectra. Ni^{2+} monocarbonyl peak height depends on gas concentration so care should be taken to make sure the spectra being compared are under the same conditions. Air exposure is likely not necessary, it can be done and maybe there are interesting properties of the Ni sites but as far as FTIR goes H_2O will interfere with CO interacting with the Ni sites potentially making adsorption experiments more difficult. There is precedent for similar ion mobility with Pd in Chabazite as shown by Lardinois et al that see ion mobility under high temperature

oxidizing conditions to extraframework cation sites.[1] Further techniques that directly characterize the Ni sites are suggested to understand the state of Ni more completely, assuming the CO/NO adsorption experiments show promise. XAS will be able to show what the average local environment looks like, with wavelet analysis potentially helping to look for the presence of a Ni – Ni scattering path (see Chapter 4) after reoxidation.[2] Imaging of the reduced state (higher temperature reduction may help by creating larger metallic nanoparticles) without exposure to air before loading sample into the TEM compared to after reoxidation would be very valuable. XPS has the potential to be useful as well since it is possible there may be surface enrichment of Ni after reduction given that the nanoparticles are around 1 nm after 300°C reduction and potentially larger if reduction temperature is increased.

5.5 References

1. Lardinois, T. M. *et al.* Structural Interconversion between Agglomerated Palladium Domains and Mononuclear Pd(II) Cations in Chabazite Zeolites. *Chem. Mater.* **33**, 1698–1713 (2021).

2. Zhang, G., Yang, C. & Miller, J. T. Tetrahedral Nickel(II) Phosphosilicate Single-Site Selective Propane Dehydrogenation Catalyst. *ChemCatChem* **10**, 961–964 (2018).